

ECOLE CENTRALE DE LILLE / L2EP
TSINGHUA UNIVERSITY / ELECTRICAL ENGINEERING DEPARTMENT

Dissertation for the degree of
Doctor of Engineering

Ling PENG

Title:

**Research on Graphical Modeling and
Low Voltage Ride-Through Control
Strategies of Doubly Fed Induction Wind
Generator System**

June 17th, 2010

Chairman	<i>Jianyun CHAI, Professeur, Tsinghua University</i>
Expert	<i>Maurice FADEL, Professeur à l'ENSEEIHHT / INP Toulouse, LAPLACE</i>
Expert	<i>Dianguo XU, Professeur, Harbin Institute of Technology</i>
Member	<i>George BARAKAT, Professeur, Université du Havre, GREAH</i>
Member	<i>Lipei HUANG, Professeur, Tsinghua University</i>
Invited member	<i>Jean DOREY, Directeur de l'Ecole Centrale de Pékin</i>
Co-supervisor	<i>Yongdong LI, Professeur, Tsinghua University</i>
Co-supervisor	<i>Bruno FRANCOIS, Maître de Conférences HDR, Ecole Centrale de Lille, L2EP</i>

Contents

Chapter I : INTRODUCTION	1
I.1. Context.	1
I.2. Wind technology development.....	2
I.3. Doubly-fed wind generator system	5
I.4. Low Voltage Ride Through strategies of DFIG wind turbine system.	6
I.4.1. Improved control strategies implementation.....	6
I.4.2. LVRT strategies with hardware implementation.....	9
I.5. Thesis layout.....	11
Chapitre II : MODELING AND CONTROL OF DFIG BASED WIND TURBINES	13
II.1. Modeling of the Wind Turbine System.....	13
II.1.1. Modeling of the turbine.	14
II.1.2. Modeling of the shaft.	15
II.1.3. Modeling of the gearbox.	16
II.1.4. Modeling of the DFIG.....	16
II.1.5. Modeling of the power converters.	18
II.1.6. Modeling of the DC bus.....	20
II.1.7. Modeling of the filter.	21
II.1.8. Explanation of the connection.....	21
II.2. Control strategy of the system.	22
II.2.1. MPPT strategy.....	23
II.2.2. Vector control of the DFIG	25
II.2.3. Vector control of the grid side converter.	28
II.3. Simulation results.....	31
II.4. Experimental results.....	32
II.5. Conclusion.	35
Chapitre III : MODIFIED VECTOR CONTROL STRATEGY OF THE DFIG AGAINST GRID VOLTAGE DIPS	36
III.1. Grid voltage dips.....	37

III.1.1. Characteristics of the voltage dip.	37
III.1.2. Classification of voltage dips.....	38
III.2. Modified vector control strategy of dfig.....	40
III.3. Simulation results.	44
III.4. Experimental results.	47
III.5. Feasibility region of the strategy.	50
III.6. Conclusion.	51
Chapitre IV : PERFORMANCE OF THE DFIG DURING VOLTAGE DIPS WITH AN ACTIVE CROWBAR	52
IV.1. Crowbar protection circuit.....	52
IV.1.1. Development of the crowbar circuit.	53
IV.1.2. Modeling of the active crowbar.	54
IV.2. Synthetic control and protection strategy.....	55
IV.2.1. Hysteresis control of the crowbar.	56
IV.2.2. Demagnetization control of the DFIG.....	56
IV.2.3. Grid voltage support.	57
IV.3. Simulation results.	58
IV.4. Conclusion.....	61
Chapitre V : RECONFIGURATION OF CONTROL STRATEGIES FOR HIGH POWER DFIG SYSTEM	62
V.1. Modeling of the three-level converter.	62
V.2. Control strategy of the system.	65
V.2.1. Space-vector hysteresis current control.....	66
V.2.2. Reconfiguration of the control algorithms.	72
V.3. Simulation results.	76
V.4. Experimental Results	77
V.5. Conclusion.	79
Chapter VI : CONCLUSION AND PERSPECTIVES	81
VI.1. Conclusion.....	81
VI.2. Perspective.....	82

Reference	83
------------------------	-----------

CHAPTER I

INTRODUCTION

I.1. CONTEXT.

As a result of conventional energy source consumption and increasing environmental concern, interest in technology for generating electricity from renewable energy sources, such as wind energy, is greatly increased. Wind energy is one of the most important and promising sources of renewable energy all over the world, mainly because it is considered to be nonpolluting and economically viable. Institutional and governmental support on wind energy source, together with wind energy potential and improvement of wind energy conversion technology, has led to a fast development, with a growth at an annual rate in excess of 30% and a foreseeable penetration of 12% of global electricity demand by 2020 [1].

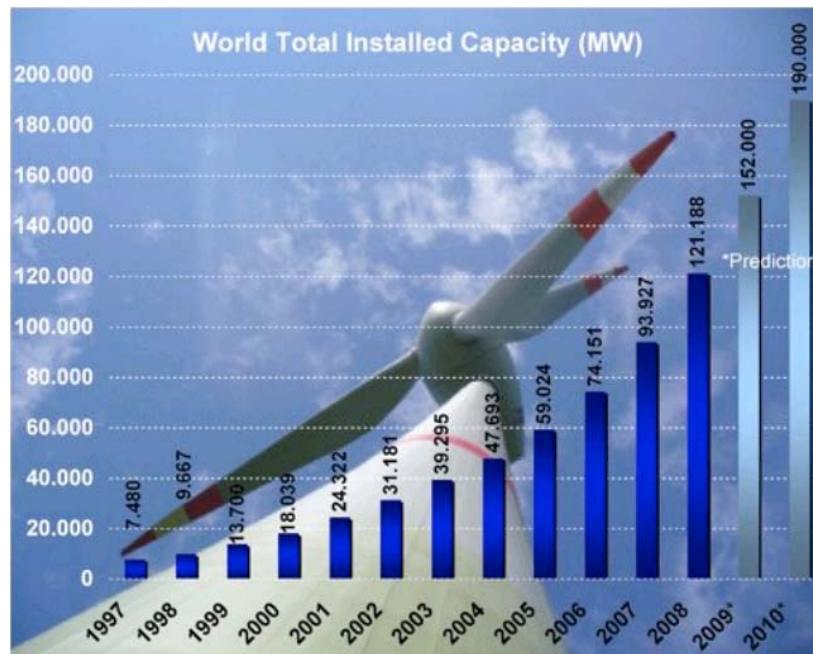


Figure I-1 : World total installed capacity of wind turbines [1]

At the end of 2008, the world total installed capacity of wind turbines has increased to 121 GW from 93 GW in 2007 (Figure I-1). According to world wind energy report in 2008,

The USA and China took the lead, USA taking over the global No. 1 position from Germany and China, which has got ahead of India for the first time, taking the lead in Asia. The USA and China accounted for 50.8% of the wind turbine sales in 2008 and the eight leading markets represented almost 80% of the market for new wind turbines – one year ago, still only five markets represented 80% of the global sales [2]. It is clear that the global market for the electrical power produced by wind turbine generators has been increasing steadily, which directly pushes the wind technology into a more competitive area [3].

I.2. WIND TECHNOLOGY DEVELOPMENT.

The development of modern wind power conversion technology has been started since 1980's, and the rapid development has been seen from 1990's. Over the past 20 years, average wind turbine ratings have grown almost linearly, as it is shown in Figure I-2, with current commercial machines rated at 1.5 MW [4].

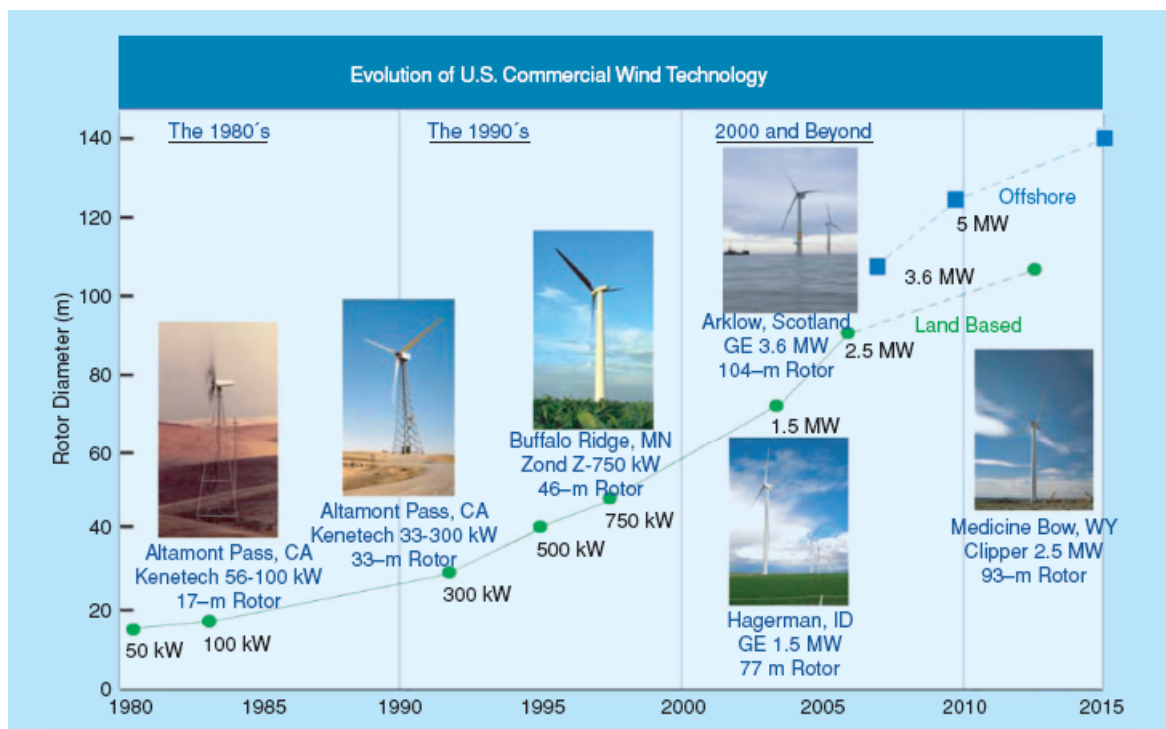


Figure I-2 : The development path and size growth of wind turbines [4]

In the beginning, fixed-speed wind turbines using Squirrel-Cage Induction Generators (SCIG) directly connected to the grid are widely used because of their design simplicity and low cost (as shown in Figure I-3). However, this system has substantial drawbacks such as it severely limits the energy conversion efficiency; a large capacitor bank is always needed to compensate reactive power; the output power varies strongly when there is a gust of wind which certainly requires a stiff power grid to enable stable operation as well as a sturdy mechanical design to absorb high mechanical stresses [5].

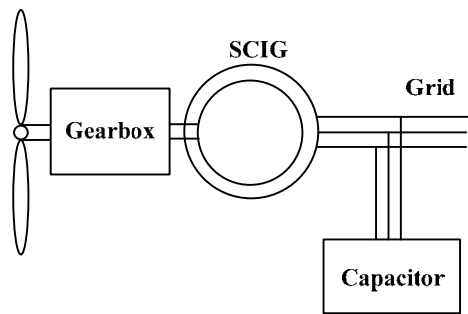


Figure I-3 : Scheme of a fixed speed concept with SCIG system

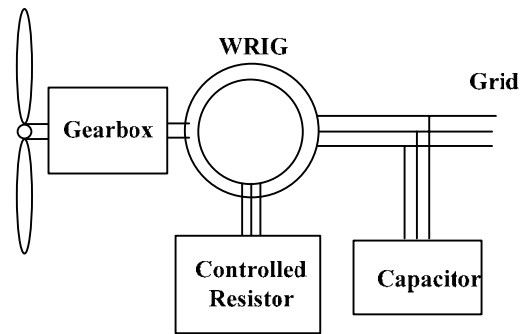


Figure I-4 : Scheme of a limited variable speed concept with WRIG system (Optislip)

Thanks to the development of power electronics, modern wind turbines can operate with variable speed, which have numerous advantages. Compared to the fixed-speed wind turbines, much more power can be produced as they can rotate at the optimal rotational speed for each wind speed. They can improve power quality as well as compensate for torque and power pulsations. And they can also reduce mechanical stresses and acoustic noise while improve the dynamic behavior of the turbine [6-7].

As shown in Figure I-4, the limited variable speed concept with a multiple-stage gearbox is also known as the Optislip concept, which has been applied by the Danish manufacturer Vestas since the mid 1990's [8-9]. This wind turbine concept uses a Wound Rotor Induction Generator (WRIG) with variable rotor resistance by means of a power electronic converter. The stator of WRIG is directly connected to the grid, whereas the rotor winding is connected in series with a controlled resistor. Variable-speed operation can be achieved by controlling the energy extracted from the WRIG rotor; however, this power must be dissipated in the external resistor. Therefore the dynamic speed control range depends on the size of the variable rotor resistance, and the energy extracted from the external resistor is also dumped as heat loss in the controllable rotor resistance. A typical limited variable speed range is less than 10% above the synchronous speed [10]. Furthermore, reactive power compensation and a soft-starter are also required for this concept.

One possible implementation way of variable-speed wind turbines is to connect a power converter directly between the stator windings of the induction generator and the grid. But this converter has to be designed rated power of the turbine which makes it very expensive. In addition, the output filters are also rated power making design difficult and costly. An alternative concept is to apply a doubly-fed induction generator (DFIG) with a bidirectional power converter connected to the rotor windings, as shown in Figure I-5. The partial-scale power converter controls the rotor frequency and thus the rotor speed. Compared to the full power wind turbines, this concept has a number of advantages [5-12]. Since only a percentage, typically 20-30%, of the rated power has to pass through the power converter, it is typically 30% of the total system power which makes it much cheaper. Since the size of the

frequency converter is depended on the operational speed range. The filters are also rated at 30% of the total power making them much cheaper. Compared with the Optislip concept, the rotor energy, instead of being dissipated, can be fed into the grid by the power electronic converter. Moreover, decoupled control of active and reactive power as well as power-factor control can be easily obtained to improve power quality. As the slip ring requires a regular maintenance and maybe results in machine failures and electrical losses, the brushless DFIG has been proposed in partial-scale power concept application. However, it is still difficult to design high power brushless DFIGs.

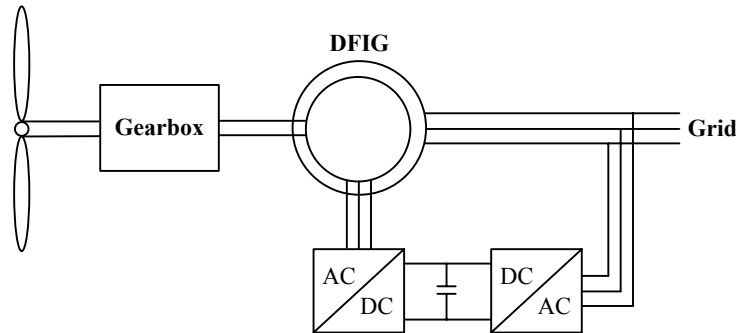


Figure I-5 : Scheme of a variable speed concept with DFIG system

Due to multiple-stage gearbox maintenance issues and related failures, a direct-drive generator connected to the grid through a full-scale power converters proposed to reduce drive train weight and cost while improving reliability [13]. The direct-drive generator can be either an Electrically Excited Synchronous Generator (EESG) or a permanent magnet synchronous generator (PMSG), as shown in Figure I-6. The main drawback of this concept is obvious the higher cost of the power converters and the filters as well as the lower efficiency of the system. The most important difference between geared drive wind turbines and direct-drive types is the generator rotor speed. The direct-drive generator rotates at a low speed, because the generator rotor is directly connected on the hub of the turbine rotor. Thus it demands a larger size of the multi-pole generator as well as a heavier weight, which causes it more difficult to install the generator in the cabin [14-15].

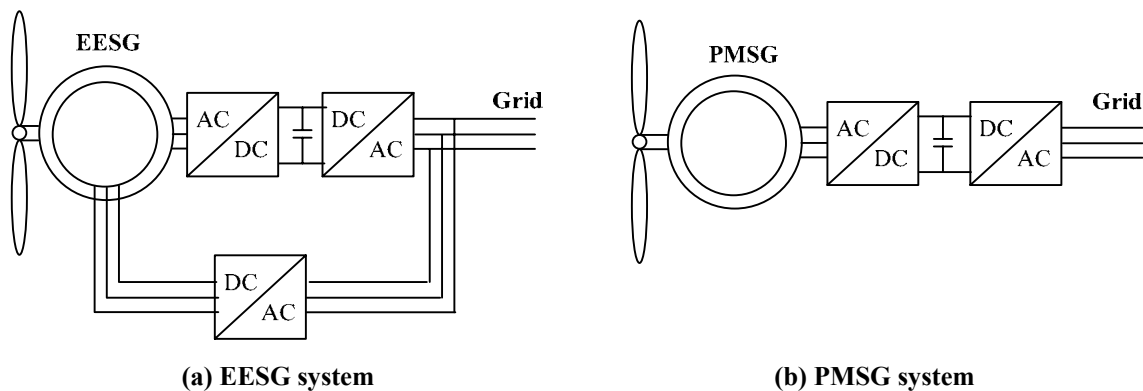


Figure I-6 : Scheme of direct-drive variable speed concept with SG system

I.3. DOUBLY-FED WIND GENERATOR SYSTEM

Nowadays, the most widely used variable speed wind turbine type for units above 1MW is Doubly Fed Induction Generator (DFIG), since it is able to generate controllable high power thanks to reduced rated power converters in comparison with other wind generator technologies for the same power.

As it is shown in Figure²² I-3, the stator is directly connected to the grid, where as the rotor is connected through a power electronic converter. There are many different kinds of topologies for DFIG [16-17], as the partial-scale power converter can be back-to-back PWM converters [18], conventional AC-AC converter [19], matrix converter [20] or hybrid current-source/voltage-source power inverter [21]. Today, factors, which influence the choices of converters are the complexity of power supplies circuit, integrity, modularization, condition of energy-saving, availability of the continuous run, technology proven or not and so on. Though progresses are made all the time, problems exist in aspects such as bridge balance and irregular stresses. The proven technology and adequate research history result in that back-to-back PWM converters along with DFIG are excellent for high power applications in the MW range. However, problems like short of voltage level and large switching losses still require solutions. The overall performance of hybrid converter is superior to both VSIs and CSIs, its concept worth comprehending although application is limited because of the complexity in control circuit. It is more likely to use multi-level converter as slip power converter in doubly-fed induction motor drive to increase the power and improve the power quality along with the soft-switching technology. That may become a mainstream in the near future. Compact design and long life due to the absence of a bulky power electronic capacitor will make matrix converter qualified for wind-turbine generator. Furthermore, the semi-tensor product of matrices method has been proposed to solve the problems of logical dynamic networks control.

Based on the dynamic mathematical model of the DFIG, various control strategies exist. Conventional design of DFIG control systems is based on rotor current vector control techniques. The control system is usually defined in the synchronous d-q frame oriented to either the stator flux [11, 18], the stator voltage (or grid flux) [22-23] or the gap flux [24]. Although it involves relatively complex transformation of voltages, currents and control outputs among the stationary and the synchronous reference frames, the output active and reactive power can be controlled independently with d-q decoupling. Some other control strategies such as Direct Torque Control (DTC) [25], direct power control (DPC) [26-27], rotor Flux Magnitude and Angle Control (FMAC) [28] and also some nonlinear control strategies [29-31] have been proposed to show their own superiority in the control performance.

I.4. LOW VOLTAGE RIDE THROUGH STRATEGIES OF DFIG WIND TURBINE SYSTEM.

In the past, most national grid codes and standards did not require wind turbines to support the power system during a disturbance. For example during a grid fault or sudden drop in frequency wind turbines were tripped off the system. However, as the wind power penetration continues to increase, the interaction between the wind turbines and the power system has become more important. This is because, when all wind turbines would be disconnected in case of a grid failure, these renewable generators will, unlike conventional power plants, not be able to support the voltage and the frequency of the grid during and immediately following the grid failure. This would cause major problems for the systems stability [39, 43, 44].

Therefore, wind farms will have to continue to operate during system disturbances and support the network voltage and frequency. Network design codes are now being revised to reflect this new requirement. A special focus in this requirement is drawn to both the fault ride-through capability and the grid support capability [39-48]. Fault ride-through capability addresses mainly the design of the wind turbine controller in such a way that the wind turbine is able to remain connected to the network during grid faults (e.g. short circuit faults). While grid support capability represents the wind turbine capability to assist the power system by supplying ancillary services, i.e. such as supplying reactive power, in order to help the grid voltage recovery during and just after the clearance of grid faults.

Due to the partial-scale power converter, wind turbines based on the DFIG are very sensitive to grid disturbances, especially to voltage dips during grid faults. Faults in the power system, even far away from the location of the turbine, can cause a voltage dip at the connection point of the wind turbine. The abrupt drop of the grid voltage will cause over-current in the rotor windings and over-voltage in the DC bus of the power converters [39-42]. Without any protection, this will certainly lead to the destruction of the converters. In addition, it will also cause over-speeding of the wind turbine, which will threaten the safe operation of the turbine [47-48]. Thus a lot of research works have been carried out on the LVRT ability of DFIG wind turbines under the grid fault. These LVRT strategies can be divided into two main types: the active method by improving control strategies, the passive scheme with additional hardware protective devices.

I.4.1. Improved control strategies implementation.

In the operational control of the DFIG, traditional vector control based on stator flux orientation or stator voltage orientation has been widely used. With this kind of control strategy, the PI controller is usually used in order to regulate independently the active and reactive power. But when there is a sharply voltage dip on the grid side, the PI controller will

get saturation easily, and it is hard to get back to the effective regulate state. The commandability of the DFIG is then lost. In order to overcome the shortcoming of the traditional vector control, the researchers around the world have proposed many improved strategies to achieve LVRT without using any other hardware circuit.

The simulation results of [42] show that through the appropriately increasing of the proportional factor of the PI regulator in the current loop of the traditional DFIG vector controller, the generator can remain in a continuous operation within a certain range when a grid fault appears. However, a dynamic response of two important state variables such as rotor current and rotor voltage can not be obtained. The proposed method can only keep the DFIG operating under a symmetrical three-phase fault, which causes a slight drop in the bus voltage. When the fault causes a serious dip in the bus voltage, over-current and over-voltage are in the exciting converter.

An improved vector control strategy has been proposed in [49] to explain that the dc and negative sequence components are caused in the machine by flux linkages, resulting in a large ElectroMotive Force (EMF) induction in the rotor circuit. A new method is proposed to control the rotor-side converter so that the rotor current contains components in order to oppose the undesired components in the stator-flux linkage. A fast observation of the stator-flux linkage components is essential to the control. This constrains the rotor current given by the voltage capability of the converter. An increased machine leakage inductance is useful to the proposed ride-through control method. The advantage of this method is that it can be applied to all types of symmetric and asymmetric grid failures and the disadvantages is that the rotor side converter is used to generate the rotor current, which is opposite to the transient component of the stator flux so that the control effect is limited to the converter capacity.

The dynamic changes of the exciting current are taken into account when designing the controller in [50], which is also based on the traditional vector control method. The improved controller can be obtained by considering the dynamic changes of the exciting current as a feed-forward compensation in the rotor current regulator. This method can effectively reduce the rotor over-current under grid voltage drops, but it is achieved by increasing the rotor-side converter output voltage. As the maximum output voltage of the rotor side inverter is limited, this method can be applied to the situation when grid faults caused a slight drop in the generator terminal voltage. But for a serious drop in the generator stator voltage (caused by serious grid faults), the rotor side converter can not provide a sufficient high exciting voltage. So the rotor currents will still be out of control. In addition, because the method can not reduce the power fed into the rotor side converter, the stability of the DC voltage is not improved.

The above control strategies are all based on the traditional vector control strategy, because the vector control strategy has a high precision, constant switching frequency and

good steady-state performances. But at the same time, in order to achieve a decoupling control of the active power and reactive power, the control structure of the vector control is usually complicated. Therefore, there are some researchers who have proposed other control strategies. In order to avoid the impact of the cross-coupling compensation, a doubly-fed generator rotor Flux Magnitude and Phase Angle control (FMAC) is proposed in [28]. Unlike the vector control, which uses the rotor current to achieve control objectives, it uses the rotor flux amplitude to control the generator terminal voltage, and the rotor flux phase angle to control the output active power. Compared with the traditional vector control methods in [42], simulation results show that the new controller has better decoupling control performance on terminal voltage and output power, and when a slight drop happens in the grid voltage, the terminal voltage recovery capability and the power oscillation damping effect under grid faults are better than vector control. But it has to be noticed that when designing the controller, a reduced-order model of the DFIG, is used without considering the dynamics of stator flux. It is mentioned in [51] that a reduced-order model can only approximate average transient currents, but can not get the accurate transient current value, which is not sufficient for analyzing DFIG transient characteristics. In order to get detailed transient characteristics of the DFIG, a full-order model is necessary.

In order to improve the LVRT capacity of double-fed induction generator, non-linear control strategies have also been used in the DFIG control system, such as fuzzy control [29], exact linearization method [30] and reliable H_{∞} control technology [31]. However, these control schemes are very complicated in practical application, as they need a mass of calculation times which are not possible in a real-time operation.

The above literatures focused on the symmetrical three-phase voltage dips, but in the practical power system, the non-symmetrical voltage dips caused by the non-symmetrical faults are more frequent. As the asymmetrical faults will not only induce the dc component but also the negative sequence component in the stator flux, it will cause large transients, so that it is more difficult to control the DFIG during a non-symmetrical voltage dip. The published literatures are focused on how to control the DFIG system under unbalanced grid voltage conditions, seldom discusses the asymmetrical voltage dip ride-through strategy [52-58].

From the above simulation results, the improving of the control strategies can reduce transient response of some variables. However, from the energy conservation point of view, when a grid fault occurs, the generator terminal voltage is lower than in the normal operating mode. It means that the wind energy conversion system can not proper transfer power to the grid. At the same time, due to the large wind turbine inertia, the absorbed wind energy remains unchanged, so there will be a part of the captured wind energy that cannot be transferred to the grid. Only by improved the control strategies cannot give this part of energy a release channel obviously.

Actually through the control strategy, it is possible to get a balance between voltage and current, making sure that neither one will not get too high when absorbing the excess energy by the system itself. However, this method is only applicable in the case when voltage dip is not very serious. Once the voltage drop is too serious, only improving the control strategies will be difficult to achieve LVRT, which means that auxiliary protection circuit is necessary in such cases.

I.4.2. LVRT strategies with hardware implementation.

Since in doubly-fed wind power generation systems, the capacity of rotor-side converter is relatively small compared with the rated capacity of generator, the rotor-side converter can only provide partial control of the generator. Therefore when power system faults occur and a deep drop of generator terminal voltage occurs, the rotor-side converter will still lose the control of rotor currents. That is why an additional hardware protection circuit is necessary. The hardware implementation can be in the rotor side, the dc side or the stator side, as shown in Figure I-7.

Currently, the most commonly used protecting scheme is short-circuiting the rotor winding through the crowbar protection circuit when rotor currents of the doubly-fed generator or DC bus voltage exceed their rated value during the grid fault. Hence a path for the rotor over-current is provided, so that the rotor-side converter can be well protected [59]. Since the traditional crowbar circuits cannot be turned off shortly after the grid fault because of the thyristors, which does not meet the new grid codes.

Therefore, new active crowbars, using active switches such as IGBT and GTO, are proposed to protect the system [60]. The rotor-side converter with this kind of circuit can be still connected to the rotor when a grid fault occurs. And after the fault, the power system can be more flexible, taking less time to return to a normal operating mode. In order to decrease the rotor transient faster, the active crowbar circuit usually has a resistor on the DC side.

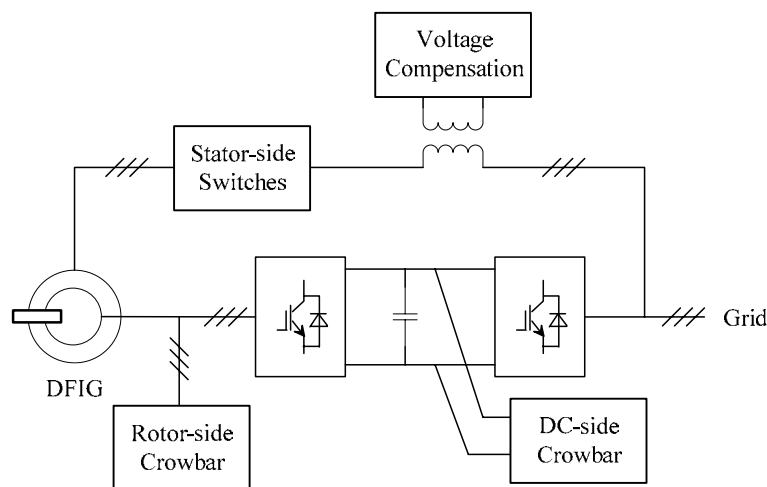


Figure I-7 : Hardware protection circuits for DFIG system

In [61], the pitch control is used to restrain the over-speeding of the turbine while a crowbar is implemented to protect the system. But there are many time delays to control the pitch angle, so that a damping controller is proposed to reduce the torsional oscillations in the drive train during grid faults before the crowbar is triggered [47]. Then a voltage controller from the rotor-side and a reactive power boosting controller from the grid-side are proposed to support the grid voltage during the fault [48]. With the cooperation of the above three controllers and the crowbar protection, the LVRT capability of the DFIG system can be greatly enhanced. It should be mentioned that the timing sequence for the crowbar removal affects the variations of currents and the electromagnetic torque after the fault clearance. A PWM control strategy of the active crowbar is proposed in [63]. The DC bus is controlled by a PI regulator. Compared to the traditional ON-OFF control method, the new PWM control can effectively reduce the electromagnetic torque ripple and thus a more stable output DC bus voltage is obtained in fault condition. However, rapid switching under this PWM control mode may exacerbate the transient progress of the DFIG, resulting in a higher transient current and a longer recovery time.

An improved crowbar is adopted in [39], which is constructed by three-phase AC switches and resistors. The crowbar is used to damp the short circuit rotor currents and bypass them away from the rotor-side converter. At the same time the rotor side converter can remain connected to the rotor windings. When the fault is cleared, the active crowbar can be removed immediately to get the system resume normal operation. If the voltage dip lasts for a long time, the crowbar can be disconnected and the rotor-side converter can be restarted to control the generator to provide reactive power to the grid in order to help the grid voltage recovery. However, as the rotor-side converter will remain physically connected to the rotor slip-rings, it may be exposed to a voltage higher than the dc bus voltage in response, owing to the higher crowbar resistance.

The use of an active crowbar circuit can effectively protect the rotor converter under serious grid faults. But its main drawback is that, when the crowbar is activated, the rotor-side converter cannot control the active and reactive power any longer. At the same time, the DFIG will be excited by the stator rather than by the rotor-side converter, and will operate as a conventional cage induction generator. Then, it will absorb a large amount of reactive power from the grid and lead to further deterioration of the grid voltage stability.

When the grid voltage drops, over-current in the rotor side appears and the output power from the rotor side will be restricted. This energy will be accumulated in the DC bus, which will cause the increasing of the DC bus voltage and destroy the DC side capacitors as well as power converters. To maintain the DC bus voltage, a regular method is to add dissipation loads on the DC side to consume the extra energy. This kind of load often consists of resistor in series with the power electronic switch, which will waste the extra energy [44]. In order to solve this problem, [64] uses the energy storage device (ESS) instead of a DC-side crowbar

circuit. According to the operating speed of the doubly-fed generator, the ESS could absorb energy to store the extra energy in fault condition, and export this energy back to the grid after a fault. Instead of a crowbar, the ESS can prevent the transient in switching operation state and keep the system controllable all the time. Moreover, if the converter is Dripped from the grid under a fault, the energy stored in the ESS can maintain the DC bus voltage, which ensures the output voltage ability of the converter and enhance the control ability of the rotor transient current [65]. However, the ESS cannot control the rotor current. Thus large-capacity power devices are necessary for the rotor-side converter in order to protect it from damage by rotor over-current. This will increase the cost of the system. Therefore, the DC side protection circuit will increase the cost of the system, but it can also provide better a control effect during grid faults.

It was recommended in [41] that an electronic switch should be inserted in the stator side in addition to the crowbar on the rotor terminals. This procedure will disconnect the stator winding during the fault so it prevents the reactive power absorption. Yet, it completely interrupts the stator active power generation during the fault. This method requires an additional switch with the rating of the stator circuit. Compared to traditional rotor side crowbar protection circuit, it has advantages in the transient restriction [66]. But in normal condition, the turned on thyristors will reduce the efficiency of the system. Moreover, the most important point is that it does not realize the real ride-through operation, as the DFIG is disconnected during the fault. In [46], enhancing the LVRT capability is achieved by inserting a series-connected voltage source converter at generator terminals which supports the voltage during the fault. However, the optimization consideration is not fulfilled since an expensive hardware is added.

I.5. THESIS LAYOUT.

The objective of the thesis is to develop an integrated control and protection system for modern wind turbines to fulfill the revised grid requirements. The following parts of the dissertation are organized as follows:

In Chapter 2, the dynamic model of the wind turbine system based on DFIG is firstly established, and then the control system in normal operation is deduced, including the control strategies of the wind turbine, the DFIG and the PWM rectifier.

In Chapter 3, a modified vector control strategy of the DFIG is proposed and then compared to the conventional vector control strategy to show the better ride-through performance against small voltage dips.

In Chapter 4, an active crowbar circuit is implemented with hysteresis protection scheme cooperated with demagnetization control of the DFIG in order to improve the ride-through capability and grid support capability during large voltage dips.

In Chapter 5, a reconfiguration scheme of control strategies for DFIG based high power wind turbine system in order to enhance the ride-through capability and fulfill the grid code requirements.

Finally, the obtained conclusion and proposed future work are presented.

CHAPITRE II

MODELING AND CONTROL OF DFIG BASED WIND TURBINES

Due to their advantageous characteristics, nowadays the most widely used variable speed wind turbine type for units above 1MW is doubly fed induction generator (DFIG). In order to study the dynamic behavior of the wind turbine, a suitable model of the wind energy conversion system is necessary. This chapter mainly describes the dynamic model of the DFIG based wind turbine including both mechanical and electrical components. The conventional control system consists of a maximum power point tracking (MPPT) algorithm, a decoupled control of the generated active power and reactive power, the power factor control by the grid-side PWM converter and the voltage control of the intermediate DC bus will also be presented.

II.1. MODELING OF THE WIND TURBINE SYSTEM.

Figure II-1 shows the basic configuration of a DFIG based wind turbine. The DFIG is essentially a wound rotor induction generator with slip rings. The stator is directly connected to the grid and the rotor is interfaced through a partial-scale variable frequency power converter. The DFIG is doubly fed by means that the voltage across the stator circuit is applied from the grid and the voltage across the rotor circuit is generated by a power electronic converter. In order to cover a wide operation range from sub-synchronous to super-synchronous speeds, the rotor side power electronic converter has to be able to operate with a power flowing in both directions. This is achieved by means of a back-to-back power converter, which consists of two voltage source converters (rotor side converter and grid side converter) and a common DC bus. The grid side converter is connected to the grid via three chokes to filter the current harmonics.

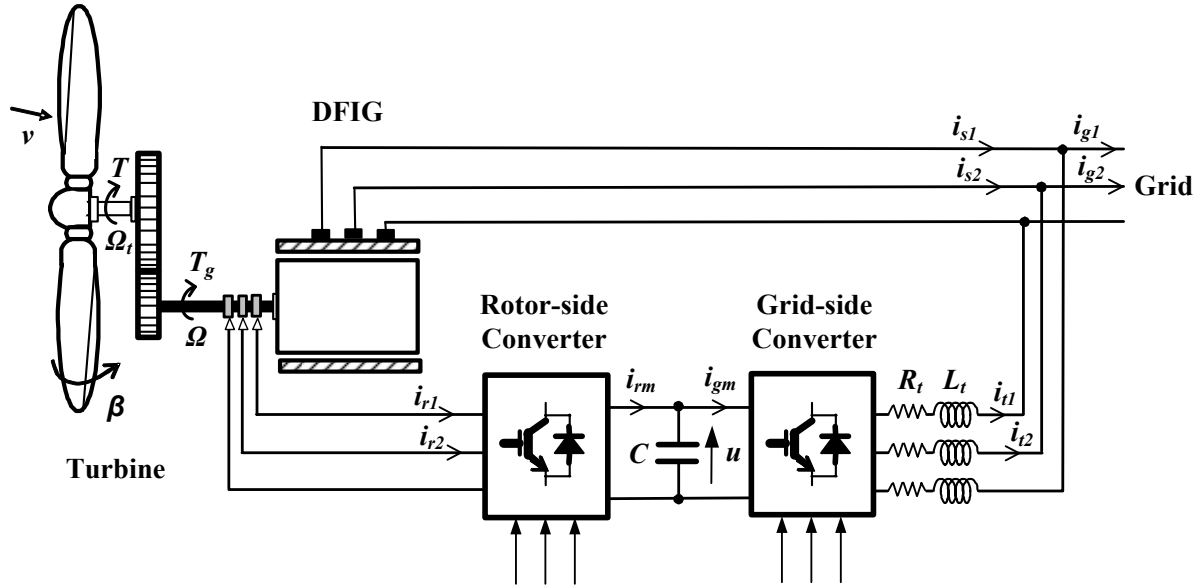


Figure II-1 : DFIG based wind turbine configuration

As we can see in the figure, the mechanical part includes the variable-pitch turbine, the gearbox and the drive train, while the electrical components consists in the generator, the back-to-back power electronics with a DC bus and the filters. The system is described by using graphic tools as the Causal Ordering Graph (COG) and the Energetic Macroscopic Representation (EMR). The COG is a graphical representation of mathematical equations, which can be used to model a system. The COG consists of a graphical language for describing dynamic systems in a physical manner thanks to the use of the natural causality principle [67-70]. Moreover, the COG formalism provides a methodology for the systematic synthesis of the control structure. When gathering all the COGs together, the EMR, which gives a synthetic description of the overall system can be obtained. EMR is based on the action-reaction principle, which organizes the system as interconnected subsystems according to the integral causality [71-73].

II.1.1. Modeling of the turbine.

The turbine is a device, which can convert wind energy to mechanical energy. It is characterized by its aero dynamical torque [74]:

$$R_1: T = \frac{1}{2\Omega_t} C_p \rho S v^3 \quad (\text{II-1})$$

Ω_t is the angular speed of the turbine, ρ is the air density, S is the swept area of the turbine and v is the wind speed. The power coefficient C_p represents the aerodynamic efficiency of the wind turbine. It depends on the blade design, the tip speed ratio λ and the pitch angle of the blades β .

The tip speed ratio is defined as the ratio between the blade tip speed and the wind speed:

$$R_2: \lambda = \frac{R\Omega_t}{v} \quad (\text{II-2})$$

For the wind turbine in this study, the following mathematical expression has been derived from [75]:

$$R_3: C_p(\lambda, \beta) = (0.5 - 0.167(\beta - 2)) \sin\left[\frac{\pi(\lambda + 0.1)}{18.5 - 0.3(\beta - 2)}\right] - 0.00184(\lambda - 3)(\beta - 2) \quad (\text{II-3})$$

Thus the COG and EMR of the considered wind turbine are depicted in Figure II-2.

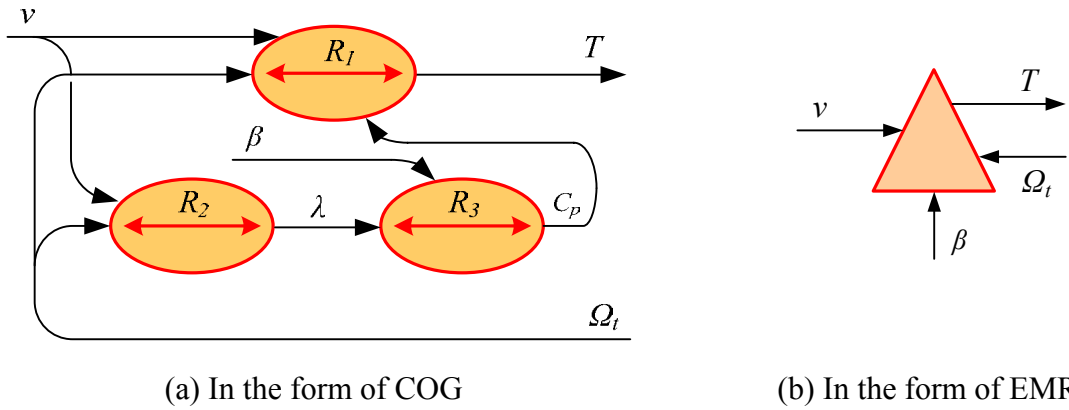


Figure II-2 : COG and EMR of the wind turbine

II.1.2. Modeling of the shaft.

The drive train is composed of the mass corresponding to the large turbine rotor inertia with the blades and the hub, and a small inertia representing the rotor mass of the generator. The proposed equivalent integrated model includes both masses. Hence the acceleration can be simply modeled by a first order differential equation:

$$R_4: J \frac{d\Omega_t}{dt} = T_t \quad (\text{II-4})$$

Where J represents the total inertia of the equivalent shaft, which is $J_t + J_g / G^2$. J_t is the large turbine rotor inertia, J_g is the small generator rotor inertia and G is the gear ratio of the gearbox.

The equivalent total torque T_t on the shaft is expressed as:

$$R_5: T_t = T - T_g - T_{vis} \quad (\text{II-5})$$

Where T_g is the torque from the gearbox, and T_{vis} can be expressed as:

$$R_6: T_{vis} = f\Omega_t \quad (\text{II-6})$$

With the friction coefficient of the equivalent shaft f , which is equal to $f_t + f_g / G^2$. J_t and J_g are the friction coefficient of the turbine and the generator respectively.

Therefore, the COG and EMR of the drive train are shown in Figure II-3.

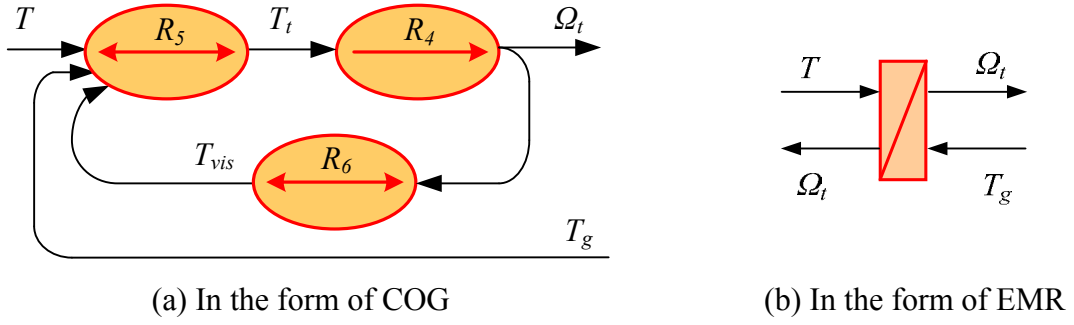


Figure II-3 : COG and EMR of the shaft

II.1.3. Modeling of the gearbox.

The gearbox transfers the aero dynamical power from the slow rotating turbine shaft to the fast rotating shaft through the gear ratio G , which drives the generator at the mechanical speed Ω . It is mathematically described by the following equations:

$$R_7: \Omega = G\Omega_t \tag{I-7}$$

$$R_8: T_g = GT_{em} \tag{I-8}$$

With T_{em} is the electromagnetic torque of the generator.

The COG and EMR of the gearbox is shown in Figure II-4.

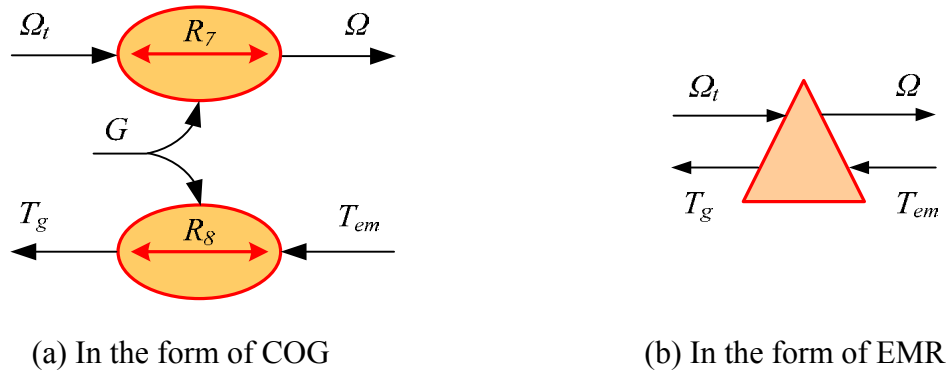


Figure I-4 : COG and EMR of the gearbox

II.1.4. Modeling of the DFIG.

A fifth-order dynamic model of the DFIG is adopted in this paper in order to use a more detailed representations of the fault current contribution and to investigate the required ratings of the converters [76]. Although the finite element method (FEM) based model is more precise with considering the stator and rotor leakage inductance variation (which is caused by the magnetic saturation), the fifth-order model is enough to be used for the dynamic performance analysis during a grid fault in order to save simulation time [77].

The model in the two-axis d-q synchronous reference frame is given as:

$$v_{sd} = R_s i_{sd} + \frac{d\psi_{sd}}{dt} - \omega_s \psi_{sq} \quad (\text{II-9})$$

$$v_{sq} = R_s i_{sq} + \frac{d\psi_{sq}}{dt} + \omega_s \psi_{sd} \quad (\text{II-10})$$

$$v_{rd} = R_r i_{rd} + \frac{d\psi_{rd}}{dt} - \omega_r \psi_{rq} \quad (\text{II-11})$$

$$v_{rq} = R_r i_{rq} + \frac{d\psi_{rq}}{dt} + \omega_r \psi_{rd} \quad (\text{II-12})$$

$$\psi_{sd} = L_s i_{sd} + M i_{rd} \quad (\text{II-13})$$

$$\psi_{sq} = L_s i_{sq} + M i_{rq} \quad (\text{II-14})$$

$$\psi_{rd} = M i_{sd} + L_r i_{rd} \quad (\text{II-15})$$

$$\psi_{rq} = M i_{sq} + L_r i_{rq} \quad (\text{II-16})$$

In these equations, R_s , R_r , L_s and L_r are the resistances and inductances of the stator and rotor windings, M is the mutual inductance, v_{sd} , v_{sq} , v_{rd} , v_{rq} , i_{sd} , i_{sq} , i_{rd} , i_{rq} , ψ_{sd} , ψ_{sq} , ψ_{rd} and ψ_{rq} are the d and q components of the space vectors of the stator and rotor voltages, currents and flux, ω_r is the slip speed and ω_s is the synchronous speed.

In order to obtain the COG of the DFIG, these equations are expressed in the form:

$$R_9: \frac{d\psi_{sd}}{dt} = v_{sd} - R_s i_{sd} + \omega_s \psi_{sq} \quad (\text{II-17})$$

$$R_{10}: \frac{d\psi_{sq}}{dt} = v_{sq} - R_s i_{sq} - \omega_s \psi_{sd} \quad (\text{II-18})$$

$$R_{11}: \frac{d\psi_{rd}}{dt} = v_{rd} - R_r i_{rd} + \omega_r \psi_{rq} \quad (\text{II-19})$$

$$R_{12}: \frac{d\psi_{rq}}{dt} = v_{rq} - R_r i_{rq} - \omega_r \psi_{rd} \quad (\text{II-20})$$

$$R_{13}: \begin{bmatrix} i_{sd} \\ i_{rd} \end{bmatrix} = \begin{bmatrix} L_s & M \\ M & L_r \end{bmatrix}^{-1} \begin{bmatrix} \psi_{sd} \\ \psi_{rd} \end{bmatrix} \quad (\text{II-21})$$

$$R_{14}: \begin{bmatrix} i_{sq} \\ i_{rq} \end{bmatrix} = \begin{bmatrix} L_s & M \\ M & L_r \end{bmatrix}^{-1} \begin{bmatrix} \psi_{sq} \\ \psi_{rq} \end{bmatrix} \quad (\text{II-22})$$

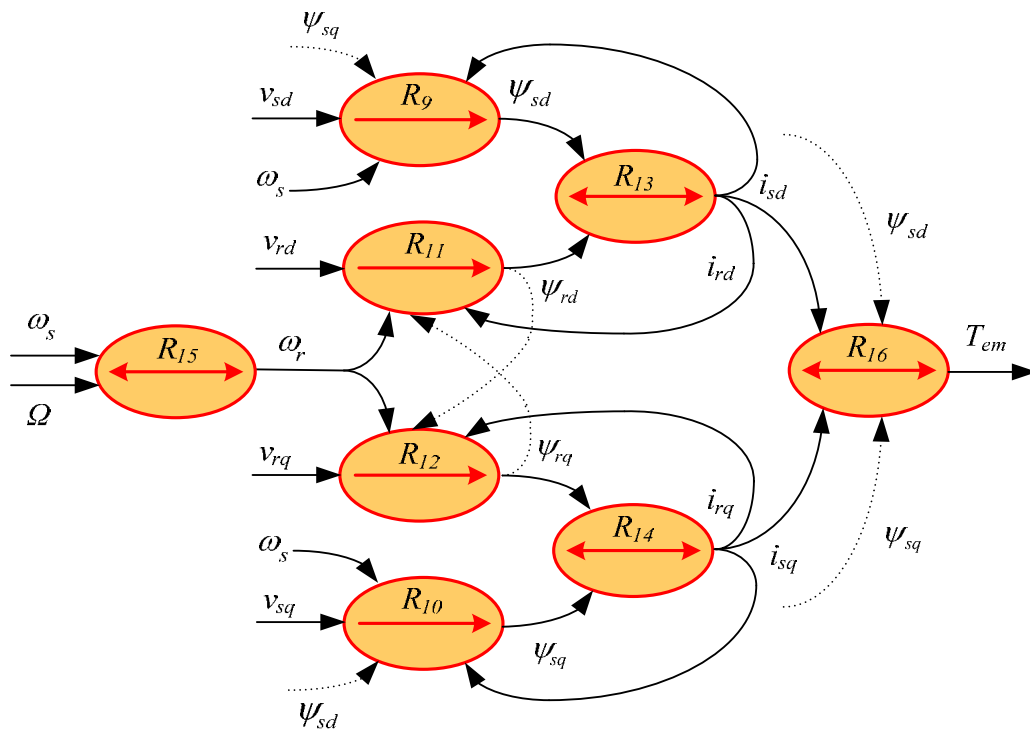
Since the stator frequency must be constant, the slip speed is deduced from:

$$R_{15}: \omega_r = \omega_s - p\Omega \quad (\text{II-23})$$

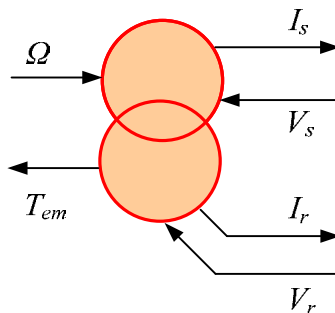
The electromagnetic torque is expressed with stator quantities and the number of pole-pairs p :

$$R_{16}: T_{em} = p(\psi_{sd} i_{sq} - \psi_{sq} i_{sd}) \quad (\text{II-24})$$

Thus the corresponding COG and EMR of the DFIG can be derived in Figure II-5.



(a) In the form of COG



(b) In the form of EMR

Figure II-5 : COG and EMR of the DFIG

II.1.5. Modeling of the power converters.

For the modeling of power electronic converters, the semiconductors are considered to be ideal: no power dissipation and instantaneous commutations. Then the power electronic converter may be considered as three commutation cells of two ideal switches.

A switching function s_{ij} is defined for each power switch. It represents the ideal commutation orders and takes the values 1 when the switch is closed and 0 when it is open:

$$s_{ij} \in \{0,1\}, \text{ with } \begin{cases} i \in \{1,2,3\} \\ j \in \{1,2\} \end{cases} \quad (\text{II-25})$$

This switching function is the theoretical (and considered effective) state of the switch. In each commutation cell both switching functions have complementary states:

$$s_{i1} + s_{i2} = 1 \quad \forall i \in \{1,2,3\} \quad (\text{II-26})$$

Then modulated voltages may be written as a product between the DC voltage u and two modulation functions, which can be defined from the switching function [78]:

$$m = \begin{bmatrix} m_1 \\ m_2 \end{bmatrix} = \begin{bmatrix} 1 & 0 & -1 \\ 0 & 1 & -1 \end{bmatrix} \begin{bmatrix} s_{11} \\ s_{12} \\ s_{13} \end{bmatrix} \quad (\text{II-27})$$

Then the modulated voltages and current of the converter can be expressed as:

$$\begin{cases} u_m = \begin{bmatrix} u_{m1} \\ u_{m2} \end{bmatrix} = mu \\ i_m = m^T \begin{bmatrix} i_1 \\ i_2 \end{bmatrix} = m^T i \end{cases} \quad (\text{II-28})$$

As line modulated voltages are balanced, phase voltages can then be expressed as:

$$v_m = \frac{1}{3} \begin{bmatrix} 2 & -1 \\ -1 & 2 \end{bmatrix} u_m \quad (\text{II-29})$$

Then the equivalent model of the rotor side converter can be expressed as:

$$R_{17}: m_r = \begin{bmatrix} 1 & 0 & -1 \\ 0 & 1 & -1 \end{bmatrix} s_r \quad (\text{II-30})$$

$$R_{18}: u_r = m_r u \quad (\text{II-31})$$

$$R_{19}: i_{rm} = m_r^T i_r \quad (\text{II-32})$$

$$R_{20}: v_r = \frac{1}{3} \begin{bmatrix} 2 & -1 \\ -1 & 2 \end{bmatrix} u_r \quad (\text{II-33})$$

With m_r is the modulation function of the rotor-side converter.

In the same way, the grid side converter can be modeled as:

$$R_{21}: m_g = \begin{bmatrix} 1 & 0 & -1 \\ 0 & 1 & -1 \end{bmatrix} s_g \quad (\text{II-34})$$

$$R_{22}: u_t = m_g u \quad (\text{II-35})$$

$$R_{23}: i_{gm} = m_g^T i_t \quad (\text{II-36})$$

$$R_{24}: v_t = \frac{1}{3} \begin{bmatrix} 2 & -1 \\ -1 & 2 \end{bmatrix} u_t \quad (\text{II-37})$$

Where i_t is the current in the filter.

The COG and EMR of the power converters is obtained as shown in Figure II-6 and

Figure II-7.

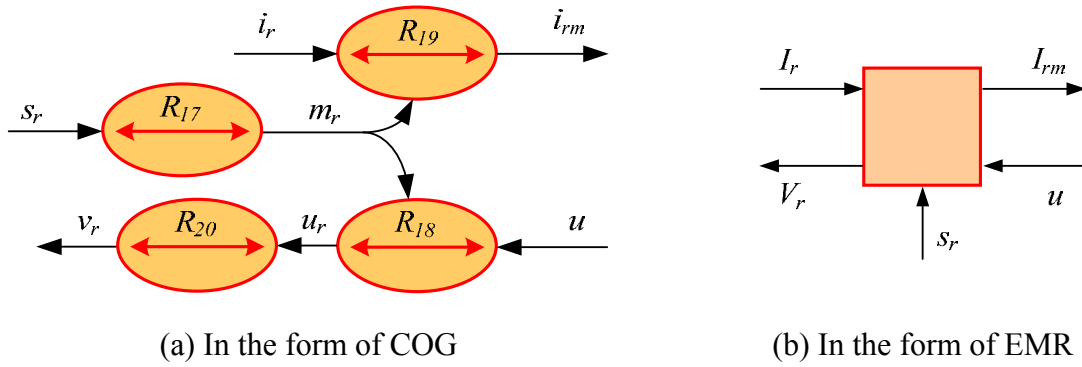


Figure II-6 : COG and EMR of the rotor-side converter

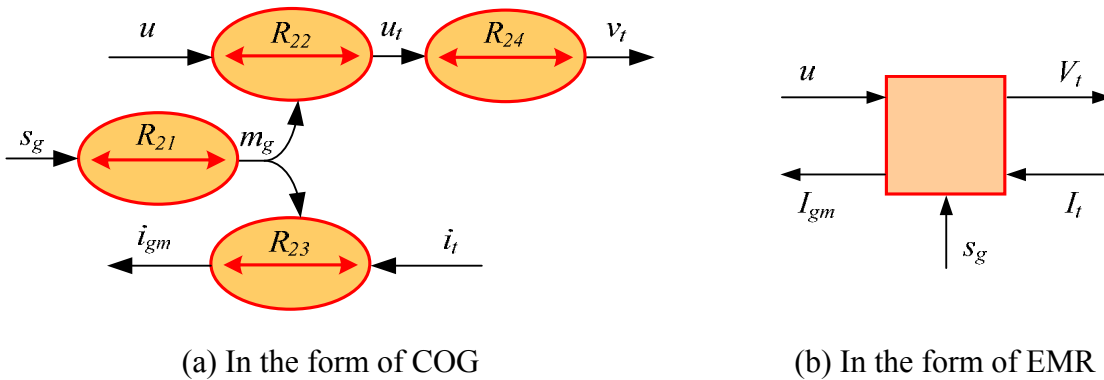


Figure II-7 : COG and EMR of the grid-side converter

II.1.6. Modeling of the DC bus.

The evolution of the DC bus voltage is given by the following equation:

$$R_{25}: C \frac{du}{dt} = i_c \tag{II-38}$$

$$R_{26}: i_c = i_{rm} - i_{gm} \tag{II-39}$$

Where C is the total capacity value of the DC bus. The COG and EMR of the DC-link is shown in Figure II-8.

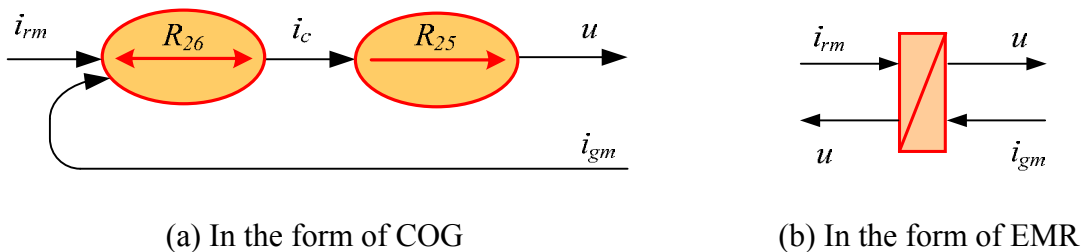


Figure II-8 : COG and EMR of the DC bus

II.1.7. Modeling of the filter.

Filter currents can be deduced from following differential equations:

$$R_{27}: L_t \frac{di_t}{dt} = v_f \quad (\text{II-40})$$

$$R_{28}: v_f = v_t - v_r - v_g \quad (\text{II-41})$$

$$R_{29}: v_r = R_t i_t \quad (\text{II-42})$$

Where L_t is the filter inductance, R_t is the filter resistance. The COG and EMR of the filter is obtained in Figure II-9.

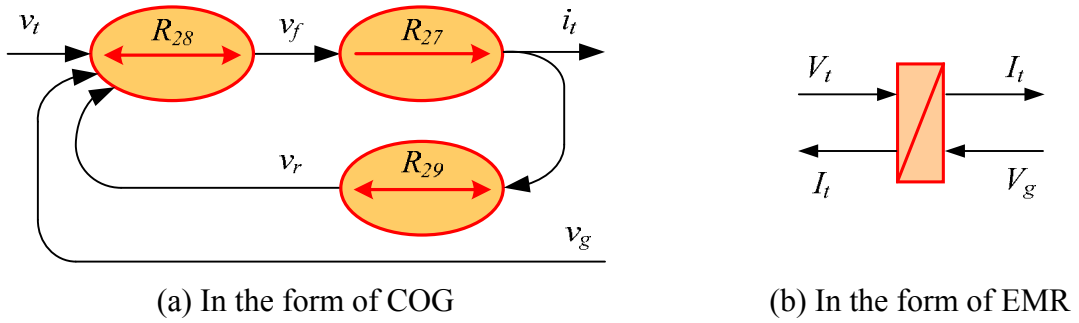


Figure II-9 : COG and EMR of the filter

II.1.8. Explanation of the connection.

Since the stator of the DFIG is directly connected to the grid while the grid side converter is connected via three filters, the grid side connection can be expressed as:

$$R_{30}: i_g = i_s + i_t \quad (\text{II-43})$$

$$R_{31}: v_s = v_g \quad (\text{II-44})$$

The COG and EMR of the grid-side connection is shown in Figure II-10.

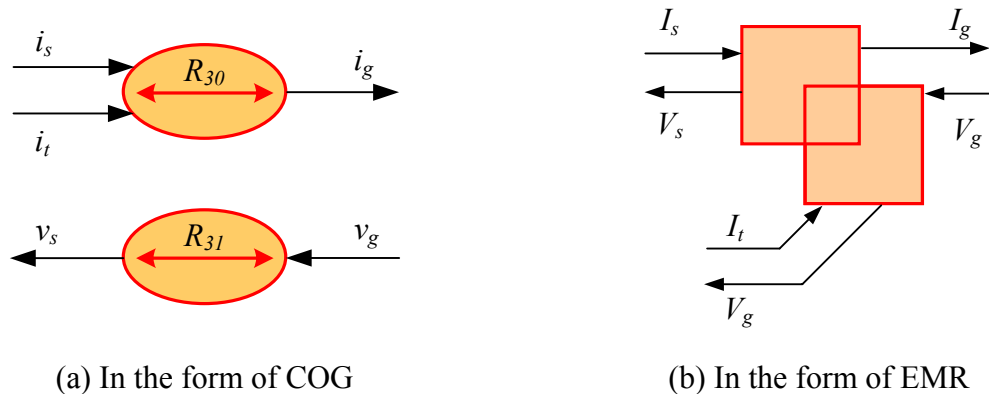


Figure II-10 : COG and EMR of the grid-side coupling

II.2. CONTROL STRATEGY OF THE SYSTEM.

A power monitoring gives a prescribed torque-speed curve that the DFIG has to track and the pitch angle according to four speed operating regions, as it is shown in Figure II-11 [79].

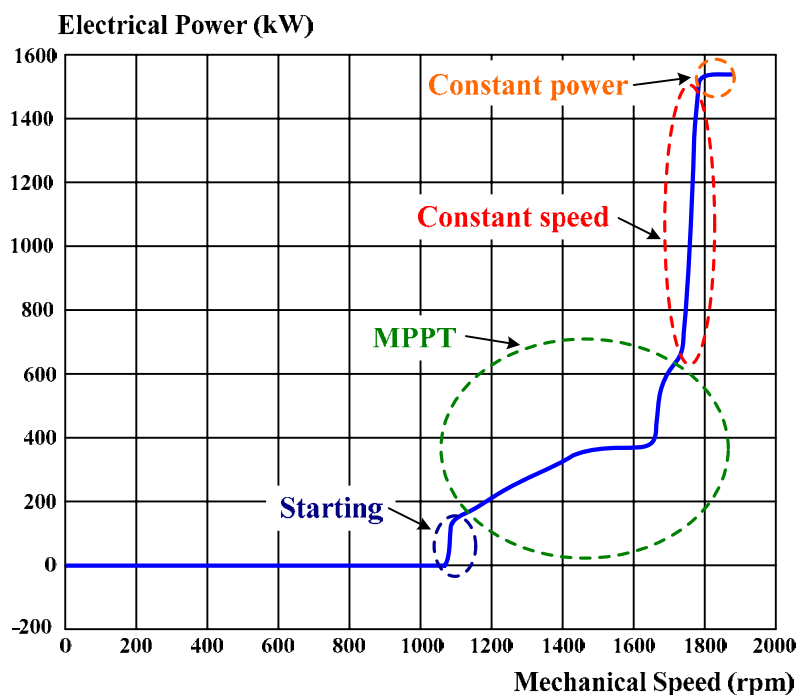


Figure II-11 : Operating regions of the wind turbine

After the starting, a control strategy is designed to extract the maximum power from the wind by setting a torque reference in the Maximum Power Point Tracking (MPPT) region. In the constant speed region the speed is regulated to a value higher than the synchronous speed to get a super synchronous operation by a closed loop control of the speed. In the constant power region the pitch control enables the power limitation to the maximum rated value while the tip speed ratio is forced to decrease the absorbed power.

When gathering all the COGs together, the EMR, which gives a synthetic description of the overall system, can be obtained. A Maximum Control Structure (MCS) can then be deduced from EMR by using specific inversion rules. Such a control leads to a maximum of control operations and measurements assuming that all variables are measurable in a first step. In a second step, simplification and estimation of non-measured variables have to be made [80-82]. The EMR and MCS of the whole system are depicted in Figure I-12.

To control the speed (Ω), two action chains appear. The first one uses the pitch angle (β) in order to modify the produced torque from the wind turbine (T) and then the gearbox torque (T_g) and so the speed. This action chain will be used to set the speed operating point

when the wind velocity is too high, so it will not be detailed here. A second one uses the rotor side converter to modify the modulated rotor voltage (V_r), then the electromagnetic torque (T_{em}) and so the speed. The electromagnetic torque can be set by the Maximum Power Point Tracking (MPPT) algorithm. This second action chain is used to apply the dynamic regulation of the speed control via two main control functions:

- A vector control of the DFIG calculates the rotor current references in order to set the electromagnetic torque and the generator reactive power;
- A converter controller calculates the necessary duty cycle.

Meanwhile the grid side converter can be used to control filter currents via modulated voltages (V_t) and the DC bus voltage (u) via the modulated current (I_{gm}). In this way, the control system of the grid side converter keeps the DC-link voltage constant and guarantees a converter operation with an expected power factor. Thus the entire control scheme can be obtained in Figure II-12.

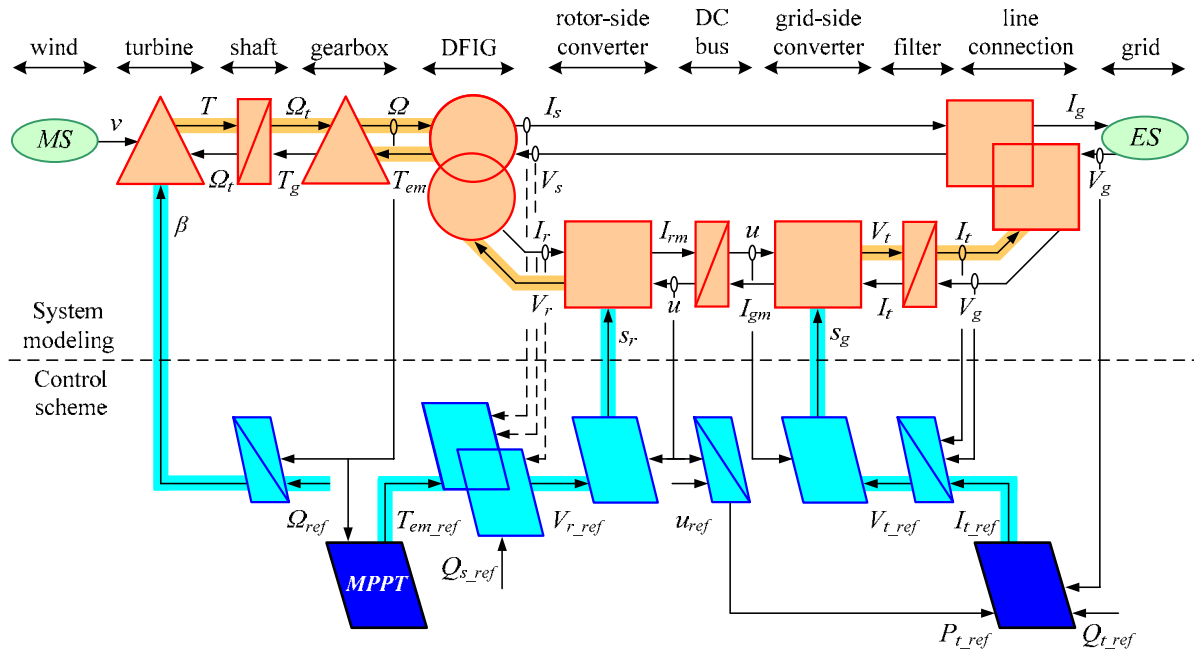


Figure II-12 : The EMR and SMC of the DFIG wind turbine system

II.2.1. MPPT strategy

As the velocity of the wind is usually difficult to measure, a MPPT strategy without measuring the wind speed is presented.

By assuming that the wind speed does not change acutely in a short time, the speed of the wind turbine remains constant during this short duration as the total inertia of the equivalent shaft is commonly very large. When the friction of the shaft is ignored, from differential equations (II-4) ~ (II-6), we can obtain:

$$R_{Sc}: \tilde{T}_g = \tilde{T} \quad (\text{II-45})$$

Then the electromagnetic torque of the generator can be derived from the turbine torque:

$$R_{8c}: T_{em_ref} = \frac{\tilde{T}_g}{G} \quad (\text{II-46})$$

In order to track the optimal rotor speed with changing wind velocity, the power coefficient should always be maintained at its maximum value (C_{p_max}). Then the absorbed aerodynamical torque can be expressed as:

$$R_{1c}: \tilde{T} = \frac{1}{2\tilde{\Omega}_t} C_{p_max} \rho S \tilde{v}^3 \quad (\text{II-47})$$

Where the speed of the turbine can be derived from the rotor speed of the generator :

$$R_{7c}: \tilde{\Omega}_t = \frac{\hat{\Omega}}{G} \quad (\text{II-48})$$

Meanwhile, for a constant pitch angle β , the tip speed ratio λ is kept constant and is equal to λ_{Cp_max} . Then the velocity of the wind can be estimated as:

$$R_{2c}: \tilde{v} = \frac{R\tilde{\Omega}_t}{\lambda_{Cp_max}} \quad (\text{II-49})$$

Therefore, the reference of the electromagnetic torque can be obtained:

$$T_{em_ref} = \frac{1}{2\lambda_{Cp_max}^3 G^3} C_{p_max} \rho \pi R^5 \hat{\Omega}^2 \quad (\text{II-50})$$

The COG of this MPPT strategy is shown in Figure II-13.

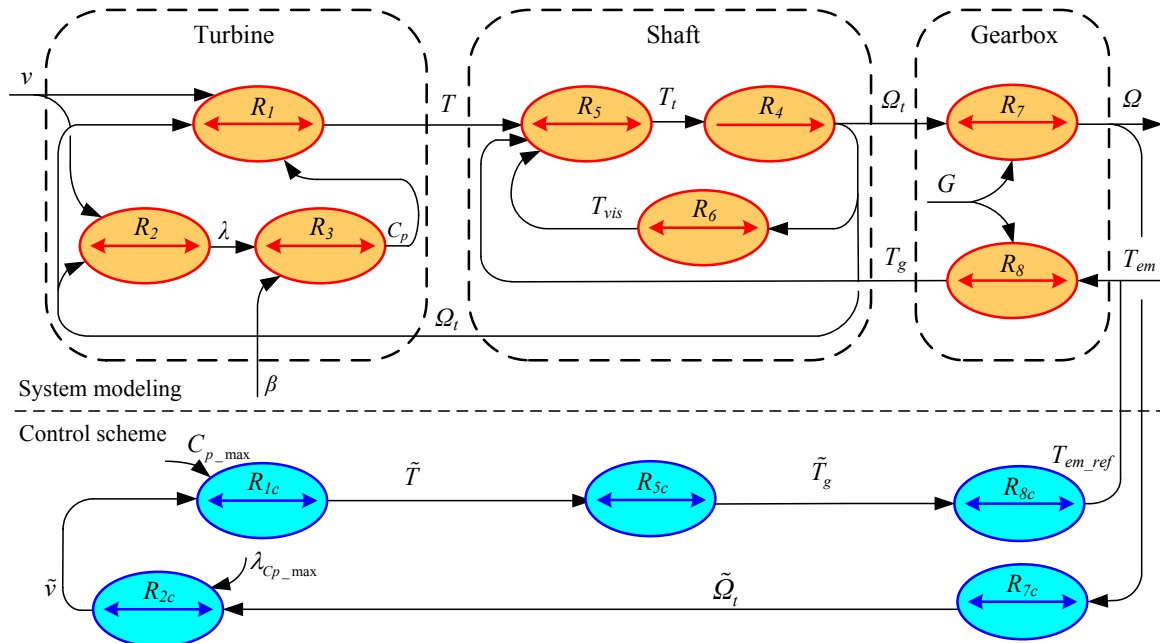


Figure II-13 : The COG of MPPT strategy without measuring wind velocity

Then the related block diagram can be obtained as shown in Figure II-14.

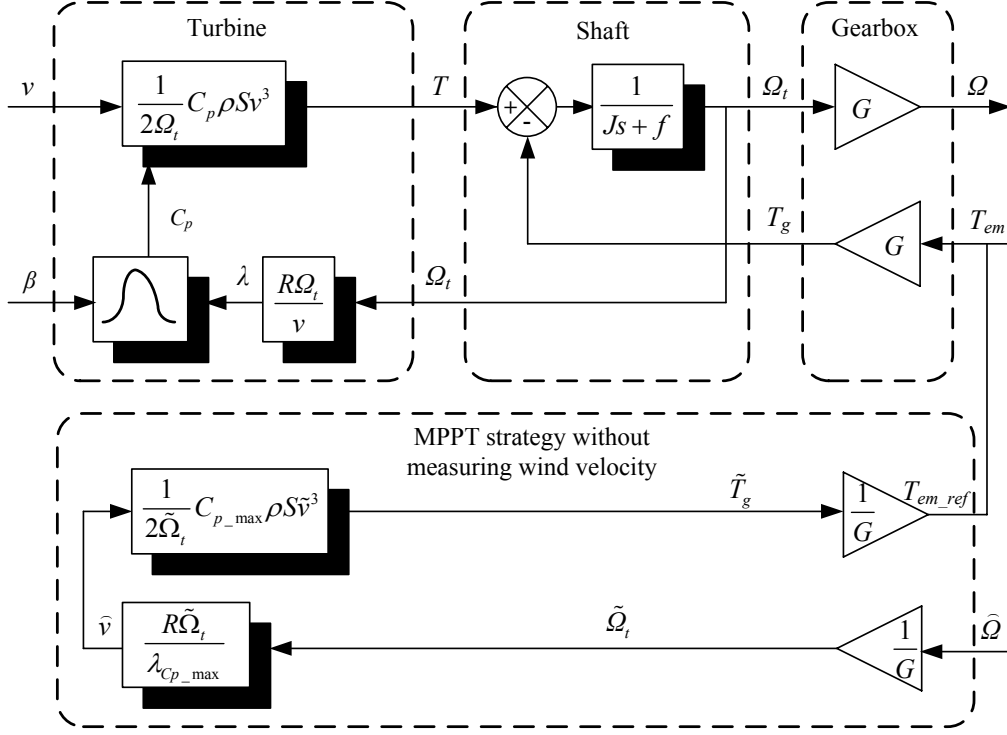


Figure II-14 : The block diagram of MPPT strategy without measuring wind velocity

II.2.2. Vector control of the DFIG

Many vector control algorithms for the DFIG have already been discussed in a variety of publications [83-86]. Vector control based on stator flux orientation enables the rotor side converter to control the electromagnetic torque and the stator reactive power independently. Currents of the power electronic converter are regulated; the quadrature axis current is used to extract the desired electromagnetic torque and the direct axis current component is used to control the reactive power.

In a synchronous rotating dq axis frame with the d -axis oriented along the stator flux vector, the relationship between the torque and the dq axis voltages, currents and fluxes can be simplified as:

$$v_{sd} = R_s i_{sd} + \frac{d\psi_{sd}}{dt} \quad (\text{II-51})$$

$$v_{sq} = R_s i_{sq} + \omega_s \psi_{sd} \quad (\text{II-52})$$

$$v_{rd} = R_r i_{rd} + \sigma L_r \frac{di_{rd}}{dt} - \omega_r \sigma L_r i_{rq} \quad (\text{II-53})$$

$$v_{rq} = R_r i_{rq} + \sigma L_r \frac{di_{rq}}{dt} + \omega_r \sigma L_r i_{rd} + \omega_r \frac{M}{L_s} \psi_s \quad (\text{II-54})$$

$$\psi_{sd} = L_s i_{sd} + M i_{rd} = \psi_s = M i_{ms} \quad (\text{II-55})$$

$$\psi_{sq} = L_s i_{sq} + M i_{rq} = 0 \quad (\text{II-56})$$

$$\psi_{rd} = \sigma L_r i_{rd} + \frac{M}{L_s} \psi_{sd} \quad (\text{II-57})$$

$$\psi_{rq} = \sigma L_r i_{rq} \quad (\text{II-58})$$

Where i_{ms} is defined as the magnetizing current, $\sigma = 1 - M^2/L_s L_r$ is the leakage coefficient.

The magnitude of the stator flux remains approximately constant since the stator circuit is directly connected to the grid. Then the torque is proportional to the q -axis component of the rotor current, so a torque control can be achieved by regulating i_{rq} :

$$T_{em} = p\psi_{sd}i_{sq} = -p\psi_s \frac{M}{L_s} i_{rq} \quad (\text{II-59})$$

As the stator resistor is very small, the d -axis component of the stator voltage is colsed to a null value. So that the stator reactive power can be derived as:

$$Q_s = v_{sq}i_{sd} = \frac{v_s\psi_s}{L_s} - \frac{v_s M}{L_s} i_{rd} \quad (\text{II-60})$$

Which means that the reactive power can be controlled by regulating i_{rd} .

In order to obtain the vector control strategy in the form of COG, we can transform these equations and then the control scheme can be deduced:

Model	Control
$R_{r1}: \frac{di_{rd}}{dt} = \frac{1}{\sigma L_r} (v_d - R_r i_{rd})$	$R_{r1c}: v_{d_ref} = C_{ir} (i_{rd_ref} - \hat{i}_{rd})$
$R_{r2}: \frac{di_{rq}}{dt} = \frac{1}{\sigma L_r} (v_q - R_r i_{rq})$	$R_{r2c}: v_{q_ref} = C_{ir} (i_{rq_ref} - \hat{i}_{rq})$
$R_{r3}: v_d = v_{rd} - e_q$	$R_{r3c}: v_{rd_ref} = v_{d_ref} + e_{q_ref}$
$R_{r4}: v_q = v_{rq} - e_d - e_\psi$	$R_{r4c}: v_{rq_ref} = v_{q_ref} + e_{d_ref} + e_{\psi_ref}$
$R_{r5}: e_d = \sigma L_r \omega_r i_{rd}$	$R_{r5c}: e_{d_ref} = \sigma L_r \omega_r \hat{i}_{rd}$
$R_{r6}: e_q = -\sigma L_r \omega_r i_{rq}$	$R_{r6c}: e_{q_ref} = -\sigma L_r \omega_r \hat{i}_{rq}$
$R_{r7}: e_\psi = \frac{M}{L_s} \omega_r \psi_s$	$R_{r7c}: e_{\psi_ref} = \frac{M}{L_s} \omega_r \tilde{\psi}_s$
$R_{r8}: T_{em} = -p\psi_s \frac{M}{L_s} i_{rq}$	$R_{r8c}: i_{rq_ref} = -\frac{1}{p\psi_{s_ref}} \frac{L_s}{M} T_{em_ref}$
$R_{r9}: Q_s = \frac{v_s\psi_s}{L_s} - \frac{v_s M}{L_s} i_{rd}$	$R_{r9c}: i_{rd_ref} = \frac{\psi_{s_ref}}{M} - \frac{L_s}{v_{s_ref} M} Q_{s_ref}$

Table II-1 : Relationship of the model and control scheme of vector controlled DFIG

Therefore, the COG of the vector control strategy can be expressed as Figure II-15.

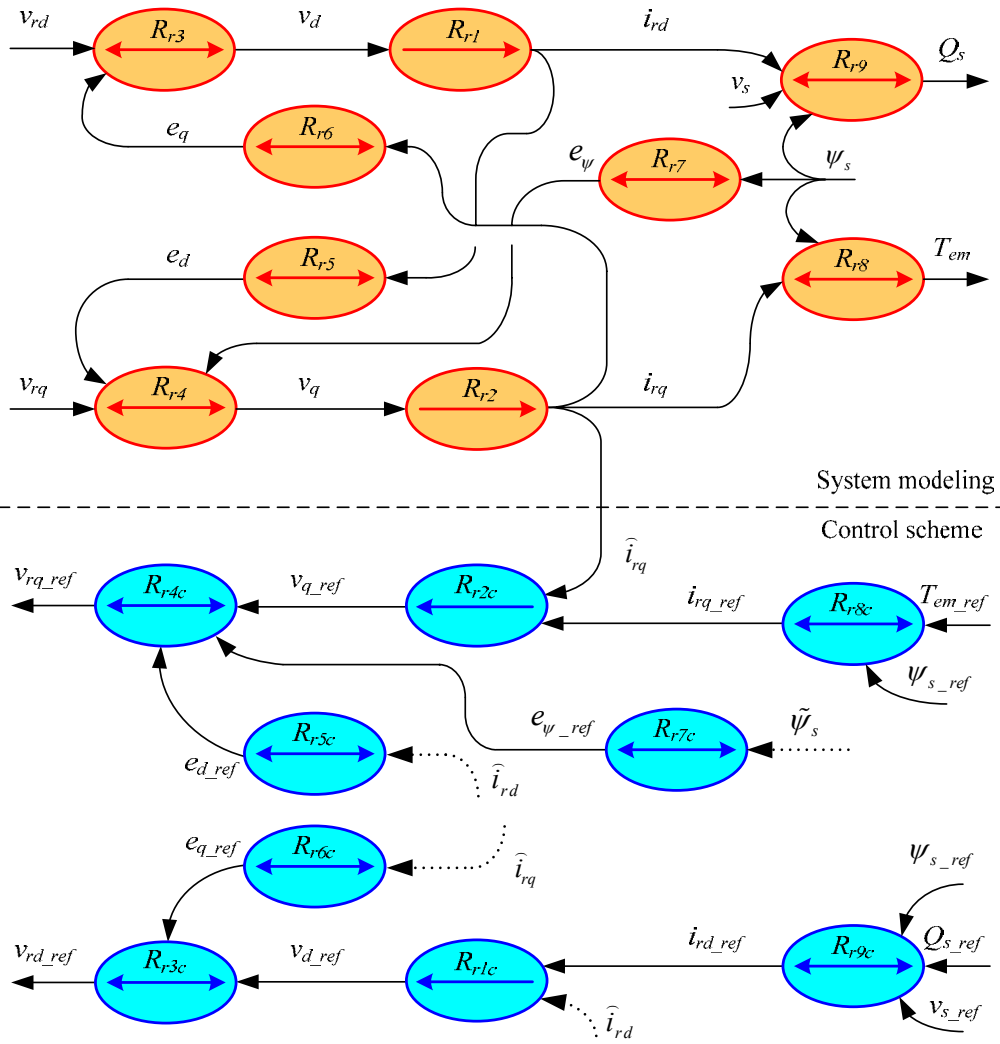


Figure II-15 : The COG of the vector control strategy of the DFIG

And the related block diagram can be obtained as Figure II-16.

COG, we can transform these equations and then the control scheme can be deduced:

Model	Control
$R_{g1}: v_{td} = v_d - e_q + v_g$	$R_{g1c}: v_{td_ref} = v_{d_ref} - e_{q_ref} + \hat{v}_g$
$R_{g2}: v_{tq} = v_q - e_d$	$R_{g2c}: v_{tq_ref} = v_{q_ref} - e_{d_ref}$
$R_{g3}: v_d = R_t i_{td} + L_t \frac{di_{td}}{dt}$	$R_{g3c}: v_{d_ref} = C_{ig} (i_{td_ref} - \hat{i}_{td})$
$R_{g4}: v_q = R_t i_{tq} + L_t \frac{di_{tq}}{dt}$	$R_{g4c}: v_{q_ref} = C_{ig} (i_{tq_ref} - \hat{i}_{tq})$
$R_{g5}: e_d = -L_t \omega_s \hat{i}_{td}$	$R_{g5c}: e_{d_ref} = -L_t \omega_s \hat{i}_{td}$
$R_{g6}: e_q = L_t \omega_s \hat{i}_{tq}$	$R_{g6c}: e_{q_ref} = L_t \omega_s \hat{i}_{tq}$
$R_{g7}: P_t = v_g i_{td}$	$R_{g7c}: i_{td_ref} = \frac{P_{t_ref}}{\hat{v}_g}$
$R_{g8}: Q_t = -v_g i_{tq}$	$R_{g8c}: i_{tq_ref} = -\frac{Q_{t_ref}}{\hat{v}_g}$

Table II-2 : Relationship of the model and vector control scheme of the grid side converter

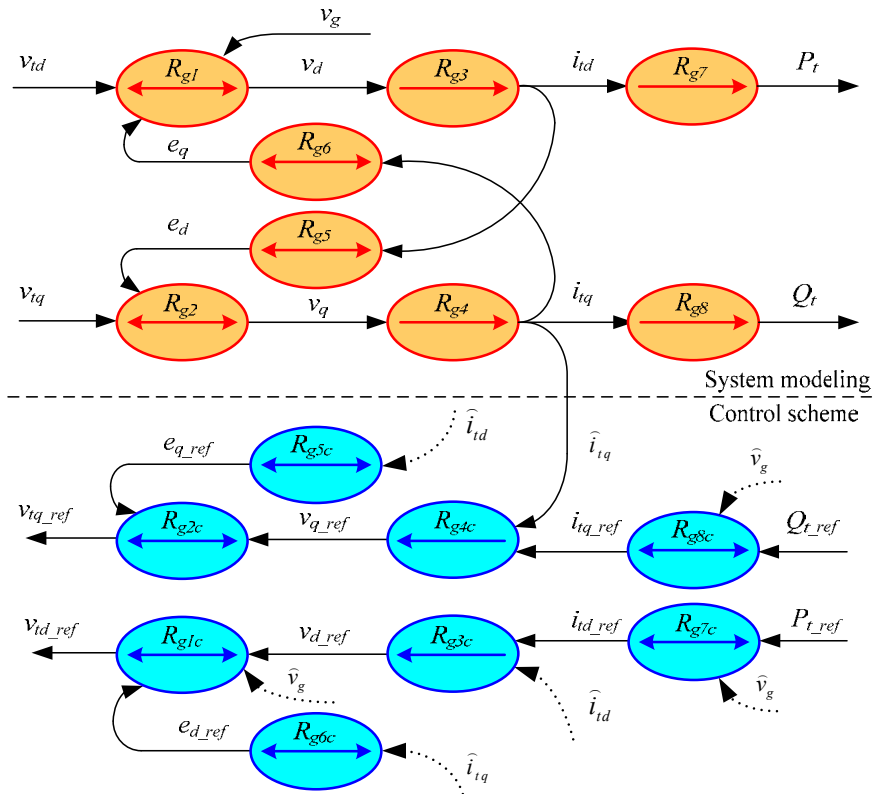


Figure II-17 : The COG of the vector control strategy of the grid-side converter

Then the COG of the vector control strategy of the grid-side converter can be expressed as Figure II-17.

And the related block diagram can be obtained as Figure II-18.

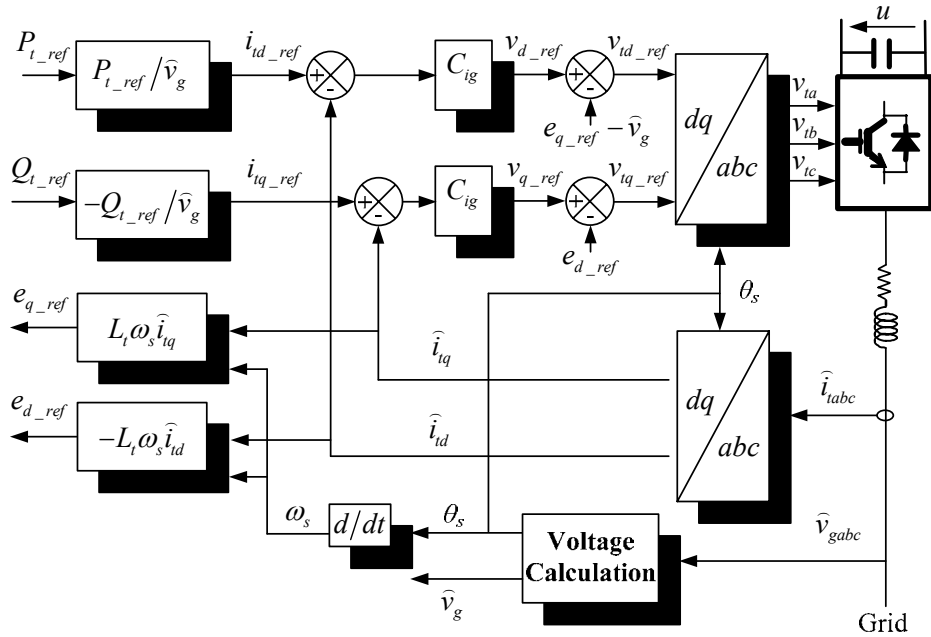


Figure II-18 : The block diagram of the vector control strategy of the grid-side converter

By neglecting harmonics due to switching and the losses in the filter and in the converter, we can get:

$$P_r = u i_c + P_t \tag{II-65}$$

As the active power comes from the converted rotor power and the variation of the capacitor DC power, the capacitor current can then be set to regulate the DC voltage to a prescribed value by a PI controller.

$$R_{c1c}: i_{c_ref} = C_u (u_{ref} - \hat{u}) \tag{II-66}$$

So the COG of the voltage control of the DC bus can be depicted in Figure II-19.

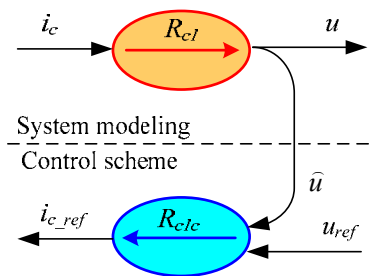


Figure II-19 : The COG of the DC-link voltage control

And the related block diagram is shown in Figure II-20.

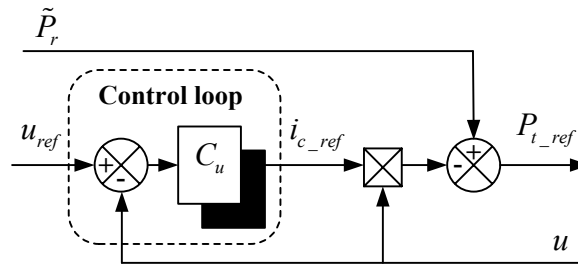


Figure II-20 : The block diagram of the DC-link voltage control

It is proved that with this instantaneous power feedback, the fluctuation of the DC-link voltage can be effectively reduced [87].

II.3. SIMULATION RESULTS.

The proposed global model and control system have been simulated with the help of Matlab Simulink™, by considering a practical 1.5MW DFIG wind turbine.

Figure I-21 shows various active and reactive power step changes corresponding to rotor current step changes. The quadrature rotor current changes to the half value of the reference at 6s, and changes back at 6.4 s, so that the generated active power reduces to the half value at 6s and resumes in normal value at 6.4 s. The direct rotor current changes from zero to i_{ms} from 5 to 5.4 s, thus the generator does not absorb reactive power during this duration. The transients is finished within in a few milliseconds, and there is no overshoot when either active or reactive power changes.

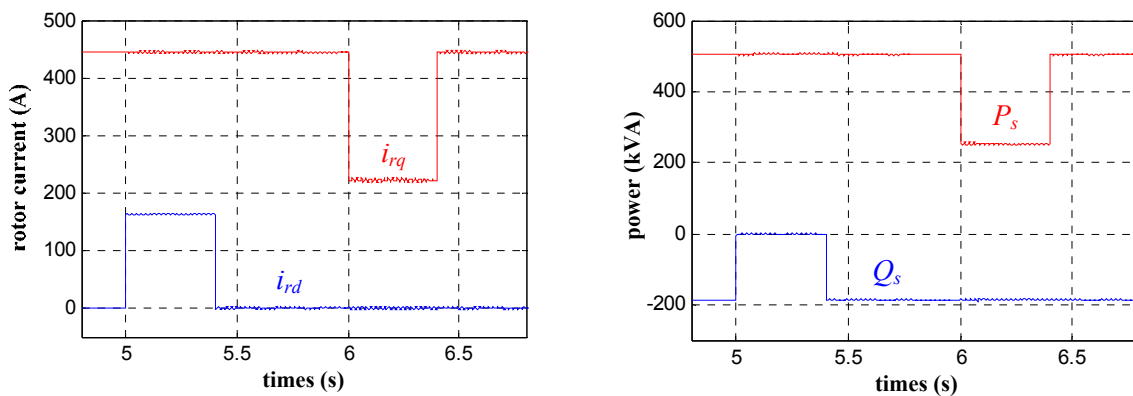


Figure II-21 : Decoupled control of active and reactive power

Figure I-22 shows the DC bus voltage and rotor current during a transition from sub-synchronous to super-synchronous speed. The DFIG experiences a smooth operation through synchronous speed, while the DC bus voltage remains stable.

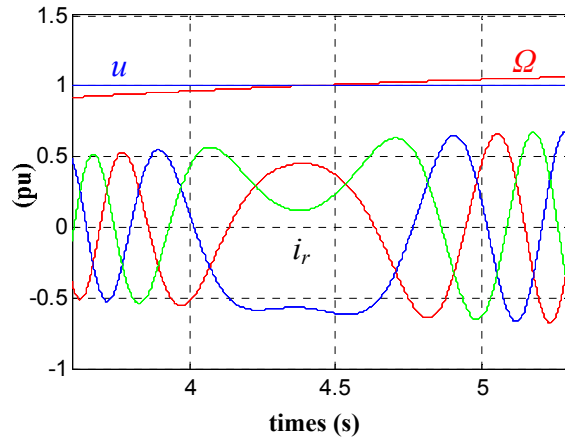


Figure II-22 : Smooth operation responding to variable rotor speed

II.4. EXPERIMENTAL RESULTS.

The obtained model and control strategies are validated with a 4.5kW DFIG laboratory test platform, which is shown in Figure II-23.

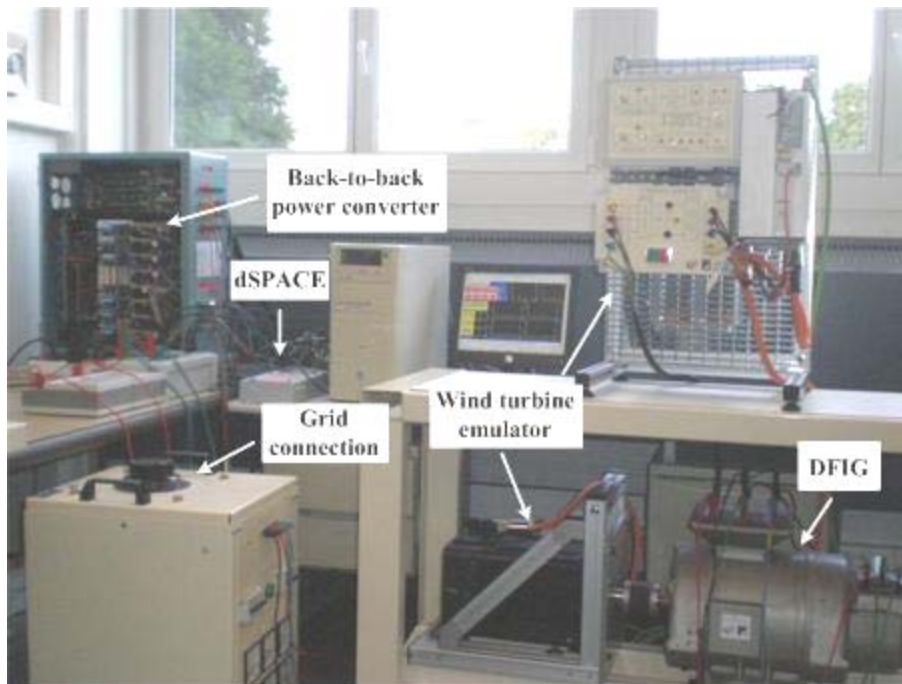


Figure II-23 : Experiment platform of the DFIG wind turbine system

The DFIG is driven by a permanent magnet synchronous motor (PMSG), which simulates the wind turbine. The PMSG is controlled by a variable speed driver that provides speed regulation. The rotor of DFIG is feeding by a back-to-back power converter. The control system is implemented on the dSPACE DS1103 DSP board. The system parameters are listed as follows.

DFIG: rated power = 4.5 kW, number of poles = 4, rated stator voltage = 380 V, rated stator current = 11 A, stator/rotor turns ratio = 2.97, stator resistance $R_s = 0.4 \Omega$, rotor resistance $R_r = 0.8 \Omega$, stator inductance $L_s = 0.082$ H, rotor inductance $L_r = 0.082$ H, mutual inductance $M = 0.081$ H (The parameters are referred to the stator side).

Figure II-24 shows the DC bus voltage and the filter current when the grid-side converter is activated. As it is shown in the figure, the DC bus voltage is controlled to be the reference value in a short time and the filter current responses quickly after the grid-side converter is started.

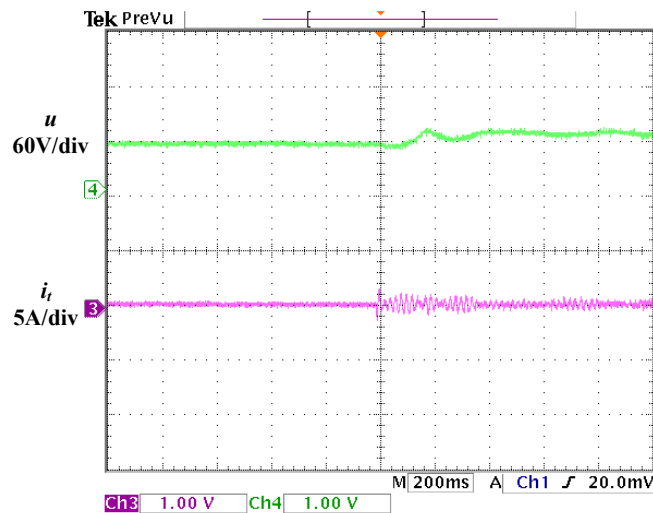


Figure II-24 : Experimental results of grid-side converter activation

The synchronization experimental result is shown in Figure II-25. Since the stator voltage maintains a good consistency with the grid voltage before the generator is connected to the network, the surge current of synchronization is very small as it is shown in the figure, which means a soft connection to the grid.

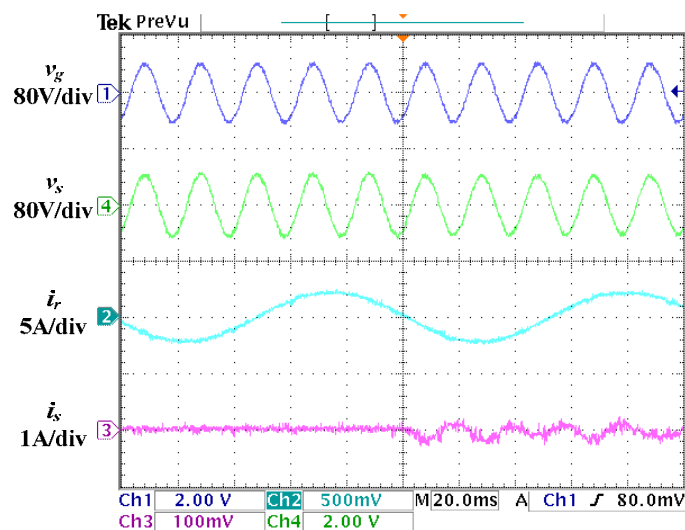


Figure II-25 : Experimental results of synchronization

Figure II-26 shows the steady-state operation of the DFIG after synchronization. The phase difference between the stator voltage and stator current is 180° , so that the generator only supplies active power to the grid. In the meantime, the stator current and the rotor current have sinusoidal waveforms with low harmonics.

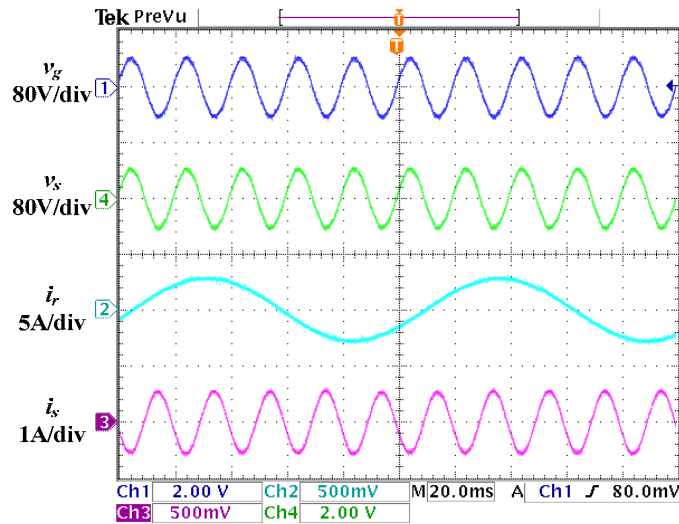


Figure II-26 : Steady operation results after synchronization

A decoupled control of the active power and the reactive power can be seen on the figure II-27, which corresponds to the simulation results. When the direct rotor current and quadrature rotor current are changed separately, the reactive power and active power will also change respectively.

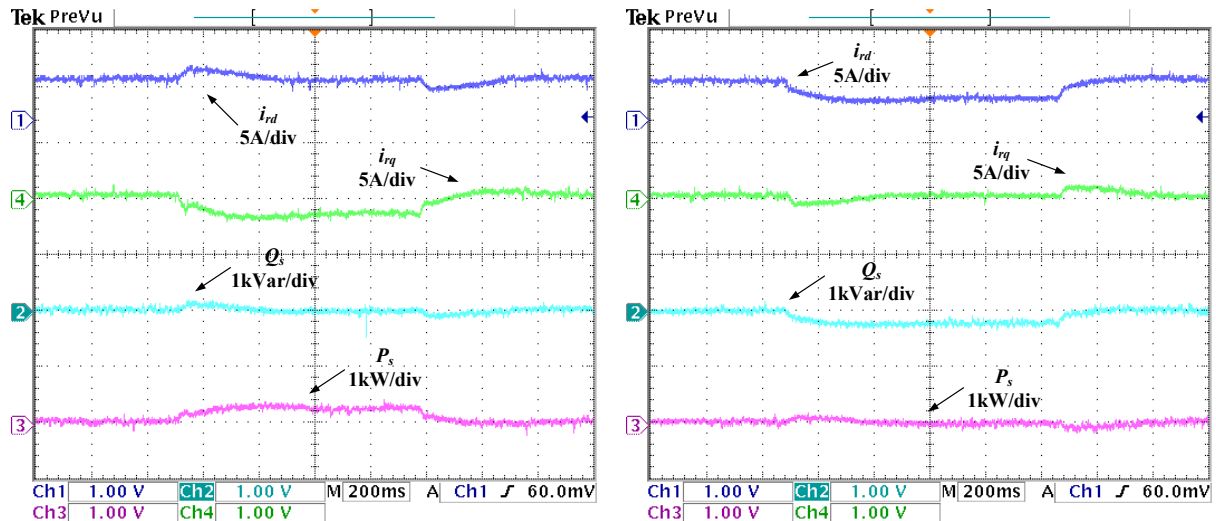


Figure II-27 : Decoupled control of active and reactive power

Figure II-28 shows the experimental results with the change of the generator speed. Either when the speed rises to super-synchronous speed or when it drops under sub-synchronous speed, the frequency of the rotor current can change with it. Thus the DFIG can operate in variable speed constant frequency (VSCF) mode.

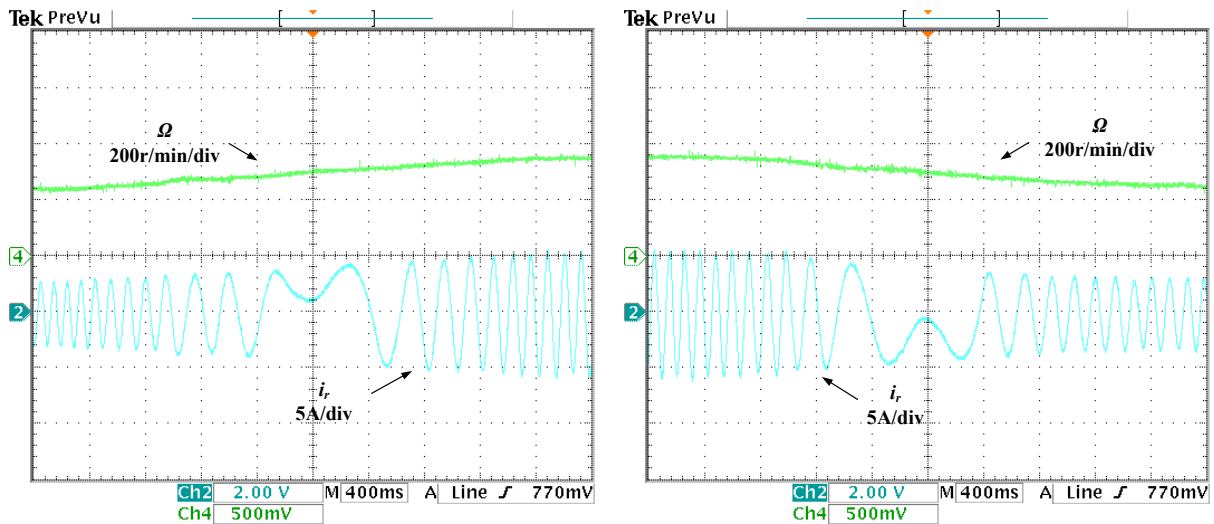


Figure II-28 : Experimental results of VSCF operation

II.5. CONCLUSION.

The DFIG based wind turbine system is modeled by using the graphical representation method COG and EMR. The conventional vector control strategies are presented to show the excellent performance of the system during normal grid condition. The decoupled control of the active and reactive power as well as an unity power factor can be easily obtained to improve the power quality. And the DFIG can operate in VSCF mode. Simulation and experimental results have proven the precision of the obtained model and the control strategies.

CHAPITRE III

MODIFIED VECTOR CONTROL STRATEGY OF THE DFIG AGAINST GRID VOLTAGE DIPS

As the wind power penetration continues to increase, many countries (especially in Europe) have issued dedicated grid codes for wind turbines with a special focus on their ride-through capability, including Fault Ride-Through (FRT) at the Point of Common Coupling (PCC) for wind farms and Low Voltage Ride-Through (LVRT) for wind turbine generators. A summary of the voltage profile for ride-through capabilities in the grid codes is shown in Figure III-1 [88]. Only when the grid voltage goes below the curves, the turbines are allowed to be disconnected. Moreover, when the voltage is in the special area, the turbines should supply reactive power.

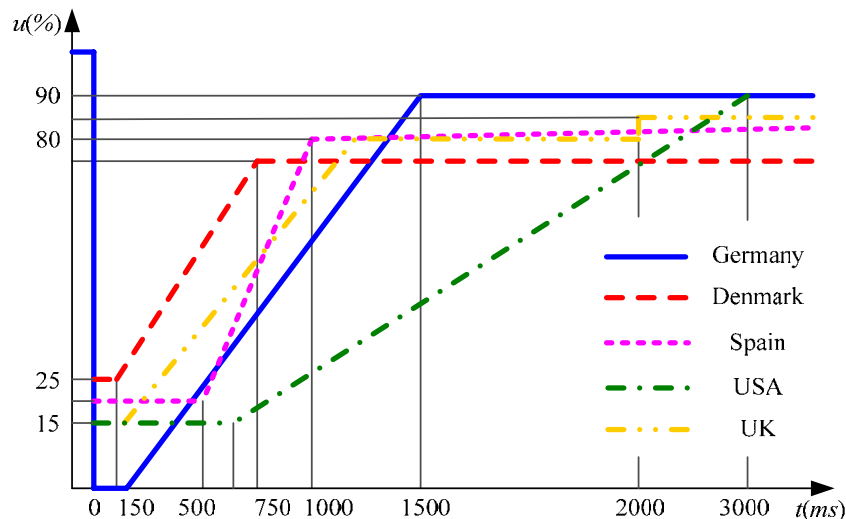


Figure III-1 : Voltage profile for LVRT in different countries

Faults in the power system, even far away from the location of the turbine, can cause a voltage dip at the connection point of the wind turbine. Even though the performance of the DFIG wind turbine is excellent in normal grid condition, a partial control of the system is obtained because of the relative small rating of the rotor side converter compared to the

generator rating. As a result, the dip in the grid voltage will result in an increase of the current in the stator windings of the DFIG. Because of the magnetic coupling between stator and rotor, this current will also flow into the rotor circuit and the power converters. So that it will cause an over current in the rotor windings and over voltage in the DC bus of the power converters [89-104]. Without any protection, this will lead to the destruction of the converters. Thus the main objective of the control system during grid faults is to limit the rotor over current and the DC bus over voltage. Vector control [97-99], direct torque control (DTC) [100], rotor flux magnitude and angle control (FMAC) [101] as well as some nonlinear control schemes [102-104] have already been applied to the DFIG during grid fault conditions. In this chapter, a modified vector control strategy will be proposed and compared with conventional vector control scheme in order to show the influence on the dynamic behavior of the wind turbine system against voltage dips.

III.1. GRID VOLTAGE DIPS.

Voltage dips are one of the most serious power quality problems and represent a major concern for the industry. They may cause interruption of industrial processes and may lead to economical losses and distorted quality products. A voltage dip (sag) is a sudden reduction (between 10% and 90%) of the voltage at a point in the electrical system, which lasts for an half of a cycle to 1 min [105].

There can be many causes for a voltage dip: short circuits somewhere in the grid, switching operations associated with a temporary disconnection of a supply, the flow of peak currents that are caused by the start of large motors, or peak currents drawn by arc furnaces or by transformer saturations. Voltage dips due to short-circuit faults cause the tripping of the majority of equipments and are therefore of most interest. Faults are either symmetrical (three-phase faults) or nonsymmetrical (two-phase-to-ground, phase-to-phase and single-phase-to-ground faults). Depending on the type of fault, the magnitudes of the voltage dips of each phase might be equal (symmetrical fault) or unequal (nonsymmetrical faults).

III.1.1. Characteristics of the voltage dip.

Figure III-2. shows the typical profile of a voltage dip. In all the referred documents it is assumed that a voltage dip can be characterized by two parameters to quantify its severity: magnitude (or “remaining voltage”) and duration. The magnitude is the lowest one-cycle rms voltage while the duration is the length of time during which the rms voltage is below a threshold. The magnitude of a voltage dip at a certain point in the system depends mainly on the type of the fault, the distance to the fault, the system configuration, and the fault impedance. As it is assumed that the rms voltage can be described by only one single-phase value, these characteristics are sufficient for a single-phase system. However, in fact the

power system is three-phase and a large fraction of equipment tripping due to voltage dips concerns three-phase loads.

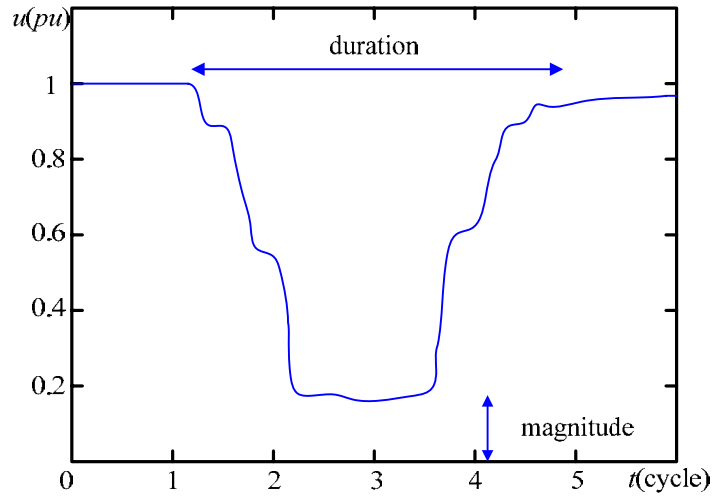


Figure III-2 : The typical profile of a voltage dip

This problem is commonly solved by characterizing three-phase voltage dips with the lowest retained voltage and the longest duration of all the three-phase rms voltages. But this method can not reflect the actual severity of the grid faults especially for equipments. And it is much harder to identify the fault type and location with this missing information.

Thus during the last few years, discussions have been started on extending these characteristics with phase-angle jump, three-phase unbalance and point-on-wave [106].

III.1.2. Classification of voltage dips.

A famous classification method is based on a space vector transformation. It leads to a more intuitive representation of voltage dips. This space vector methodology allows extracting characteristic features of the dip, to determine its type and evaluate its severity. Seven dip types can be obtained from the space vector classification method, which are due to different fault types (three-phase, two-phase-to-ground, phase-to-phase and single-phase-to-ground) under the assumption that positive-sequence, negative-sequence and zero-sequence impedance are equal [107-108]. Expressions for the complex voltages for these seven types are given in Table III-1.

Type	Phasors	Voltages	Description
A		$V_a = V$ $V_b = -\frac{1}{2}V - \frac{\sqrt{3}}{2}jV$ $V_c = -\frac{1}{2}V + \frac{\sqrt{3}}{2}jV$	Three-phase fault: it leads to an equal drop in voltage in all three phases.

B		$V_a = V$ $V_b = -\frac{1}{2}E - \frac{\sqrt{3}}{2}jE$ $V_c = -\frac{1}{2}E + \frac{\sqrt{3}}{2}jE$	<p>Single-phase-to-ground fault: it causes only the affected phase voltage to drop whereas the two other voltages remain unchanged.</p>
C		$V_a = E$ $V_b = -\frac{1}{2}E - \frac{\sqrt{3}}{2}jE$ $V_c = -\frac{1}{2}E + \frac{\sqrt{3}}{2}jE$	<p>Phase-to-phase fault: it causes two phase voltages to move towards each other whereas the third phase voltage does not change at all. Or type B after a Dy transformer.</p>
D		$V_a = V$ $V_b = -\frac{1}{2}V - \frac{\sqrt{3}}{2}jE$ $V_c = -\frac{1}{2}V + \frac{\sqrt{3}}{2}jE$	<p>Type C after a Dy transformer or Type B after two Dy transformers.</p>
E		$V_a = E$ $V_b = -\frac{1}{2}V - \frac{\sqrt{3}}{2}jV$ $V_c = -\frac{1}{2}V + \frac{\sqrt{3}}{2}jV$	<p>Two-phase-to-ground fault: it causes the affected two phase voltages to drop whereas the third phase voltage is unaffected.</p>
F		$V_a = V$ $V_b = -\frac{1}{2}V - \frac{\sqrt{3}}{3}jE - \frac{\sqrt{3}}{6}jV$ $V_c = -\frac{1}{2}V + \frac{\sqrt{3}}{3}jE + \frac{\sqrt{3}}{6}jV$	<p>Type E after a Dy transformer.</p>
G		$V_a = \frac{2}{3}E + \frac{1}{3}V$ $V_b = -\frac{1}{3}E - \frac{1}{6}V - \frac{\sqrt{3}}{2}jV$ $V_c = -\frac{1}{3}E - \frac{1}{6}V + \frac{\sqrt{3}}{2}jV$	<p>Type E after two Dy transformers.</p>

Table III -1 : Seven types of grid voltage dips

The complex pre-fault phase voltage is indicated by E . The voltage in the faulted phase or between the faulted phases is indicated by V . The transformers will transfer the three-phase unbalanced voltage dips while this change depends on the transformer type. For example, a Dy transformer change phase to phase voltages into phase-to-ground voltages, and two Dy transformers remove the zero-sequence component.

One of the main advantages of this method is the use of only the space vector and zero sequence voltage for voltage dips analysis. In addition, it especially gives a very easy graphical interpretation of the transfer of three-phase unbalanced dips through transformers. Another clear advantage is that it offers an exhaustive classification and complete characterization of three phase voltage dips by limited number of possible cases. This makes it more appropriate as basis for testing protocols, e.g. during the development of control algorithms for grid-connected power electronic converters. Types B and E can be ignored when considering the impact of the voltage dip on the wind generator. This is because these two types include a zero-sequence component that does not have to be considered [109].

III.2. MODIFIED VECTOR CONTROL STRATEGY OF DFIG.

Vector control has been widely used in DFIG based wind turbine systems. In conventional stator flux oriented vector control schemes of the DFIG, the stator flux is always considered to be constant to simplify the current controller design. However, during a voltage dip, the stator flux will drop because of the direct connection of the stator circuit to the grid. Moreover, the stator flux may lose the orientation along the d -axis during the voltage dip. Therefore, the dynamics of the stator flux should not be ignored for the design of the current controller.

In a synchronous rotating dq axis frame, the dq axis voltages of DFIG can be expressed as:

$$v_{sd} = R_s i_{sd} + \frac{d\psi_{sd}}{dt} - \omega_s \psi_{sq} \quad (\text{III-67})$$

$$v_{sq} = R_s i_{sq} + \frac{d\psi_{sq}}{dt} + \omega_s \psi_{sd} \quad (\text{III-68})$$

$$v_{rd} = R_r i_{rd} + \frac{d\psi_{rd}}{dt} - \omega_r \psi_{rq} \quad (\text{III-69})$$

$$v_{rq} = R_r i_{rq} + \frac{d\psi_{rq}}{dt} + \omega_r \psi_{rd} \quad (\text{III-70})$$

From the dq axis stator flux equations:

$$\psi_{sd} = L_s i_{sd} + M i_{rd} \quad (\text{III-71})$$

$$\psi_{sq} = L_s i_{sq} + M i_{rq} \quad (\text{III-72})$$

Note that the quadrature stator flux does not equal to zero during a voltage dip, we can

then obtain the following relationship between the stator current and rotor current:

$$i_{sd} = \frac{\psi_{sd} - Mi_{rd}}{L_s} \quad (\text{III-73})$$

$$i_{sq} = \frac{\psi_{sq} - Mi_{rq}}{L_s} \quad (\text{III-74})$$

By replacing these stator current expressions into the dq axis rotor flux equations:

$$\psi_{rd} = Mi_{sd} + L_r i_{rd} \quad (\text{III-75})$$

$$\psi_{rq} = Mi_{sq} + L_r i_{rq} \quad (\text{III-76})$$

We can obtain:

$$\psi_{rd} = \sigma L_r i_{rd} + \frac{M}{L_s} \psi_{sd} \quad (\text{III-77})$$

$$\psi_{rq} = \sigma L_r i_{rq} + \frac{M}{L_s} \psi_{sq} \quad (\text{III-78})$$

When we replace the stator current expressions (II-7) and (II-8) into the stator voltage equations (II-1) and (II-2), we can get:

$$v_{sd} = \frac{R_s}{L_s} \psi_{sd} - \frac{R_s}{L_s} i_{rd} + \frac{d\psi_{sd}}{dt} \quad (\text{III-79})$$

$$v_{sq} = \frac{R_s}{L_s} \psi_{sq} - \frac{R_s}{L_s} i_{rq} + \frac{d\psi_{sq}}{dt} \quad (\text{III-80})$$

Then by replacing the rotor flux expressions (II-11) and (II-12) into the rotor voltage equations (II-3) and (II-4), we can obtain:

$$v_{rd} = R_r i_{rd} + \sigma L_r \frac{di_{rd}}{dt} - \omega_r \sigma L_r i_{rq} - \omega_r \frac{M}{L_s} \psi_{sq} + \frac{M}{L_s} \frac{d\psi_{sd}}{dt} \quad (\text{III-81})$$

$$v_{rq} = R_r i_{rq} + \sigma L_r \frac{di_{rq}}{dt} + \omega_r \sigma L_r i_{rd} + \omega_r \frac{M}{L_s} \psi_{sd} + \frac{M}{L_s} \frac{d\psi_{sq}}{dt} \quad (\text{III-82})$$

From these equations, the PI controller of rotor current can be designed for the modified vector controller. It must take into account the quadrature stator flux (ψ_{sq}) and the dynamics of the stator flux ($\frac{d\psi_{sd}}{dt}$, $\frac{d\psi_{sq}}{dt}$) in the case of grid voltage dips.

In order to obtain the vector control strategy in the form of COG, we can transform these equations and then the control scheme can be deduced:

Model	Control
$R_{m1}: \frac{di_{rd}}{dt} = \frac{1}{\sigma L_r} (v_d - R_r i_{rd})$	$R_{m1c}: v_{d_ref} = C_{ir} (i_{rd_ref} - \hat{i}_{rd})$
$R_{m2}: \frac{di_{rq}}{dt} = \frac{1}{\sigma L_r} (v_q - R_r i_{rq})$	$R_{m2c}: v_{q_ref} = C_{ir} (i_{rq_ref} - \hat{i}_{rq})$
$R_{m3}: v_d = v_{rd} - e_q - e_{\psi d}$	$R_{m3c}: v_{rd_ref} = v_{d_ref} + e_{q_ref} + e_{\psi d_ref}$
$R_{m4}: v_q = v_{rq} - e_d - e_{\psi q}$	$R_{m4c}: v_{rq_ref} = v_{q_ref} + e_{d_ref} + e_{\psi q_ref}$
$R_{m5}: e_d = \sigma L_r \omega_r i_{rd}$	$R_{m5c}: e_{d_ref} = \sigma L_r \omega_r \hat{i}_{rd}$
$R_{m6}: e_q = -\sigma L_r \omega_r i_{rq}$	$R_{m6c}: e_{q_ref} = -\sigma L_r \omega_r \hat{i}_{rq}$
$R_{m7}: e_{\psi d} = \frac{M}{L_s} (-\omega_r \psi_{sq} + \frac{d\psi_{sd}}{dt})$	$R_{m7c}: e_{\psi d_ref} = \frac{M}{L_s} (-\omega_r \tilde{\psi}_{sq} + \frac{d\psi_{sd_est}}{dt})$
$R_{m8}: e_{\psi q} = \frac{M}{L_s} (\omega_r \psi_{sd} + \frac{d\psi_{sq}}{dt})$	$R_{m8c}: e_{\psi q_ref} = \frac{M}{L_s} (\omega_r \tilde{\psi}_{sd} + \frac{d\psi_{sq_est}}{dt})$
$R_{m9}: v_{sd} = \frac{R_s}{L_s} \psi_{sd} - \frac{R_s}{L_s} i_{rd} + \frac{d\psi_{sd}}{dt}$	$R_{m9c}: \frac{d\psi_{sd_est}}{dt} = \hat{v}_{sd} - \frac{R_s}{L_s} \tilde{\psi}_{sd} + \frac{R_s}{L_s} \hat{i}_{rd}$
$R_{m10}: v_{sq} = \frac{R_s}{L_s} \psi_{sq} - \frac{R_s}{L_s} i_{rq} + \frac{d\psi_{sq}}{dt}$	$R_{m10c}: \frac{d\psi_{sq_est}}{dt} = \hat{v}_{sq} - \frac{R_s}{L_s} \tilde{\psi}_{sq} + \frac{R_s}{L_s} \hat{i}_{rq}$

Table III-2 : Relationship of the model and control scheme of modified vector controller
 Therefore, the COG of the modified vector control strategy is depicted in figure III-3.

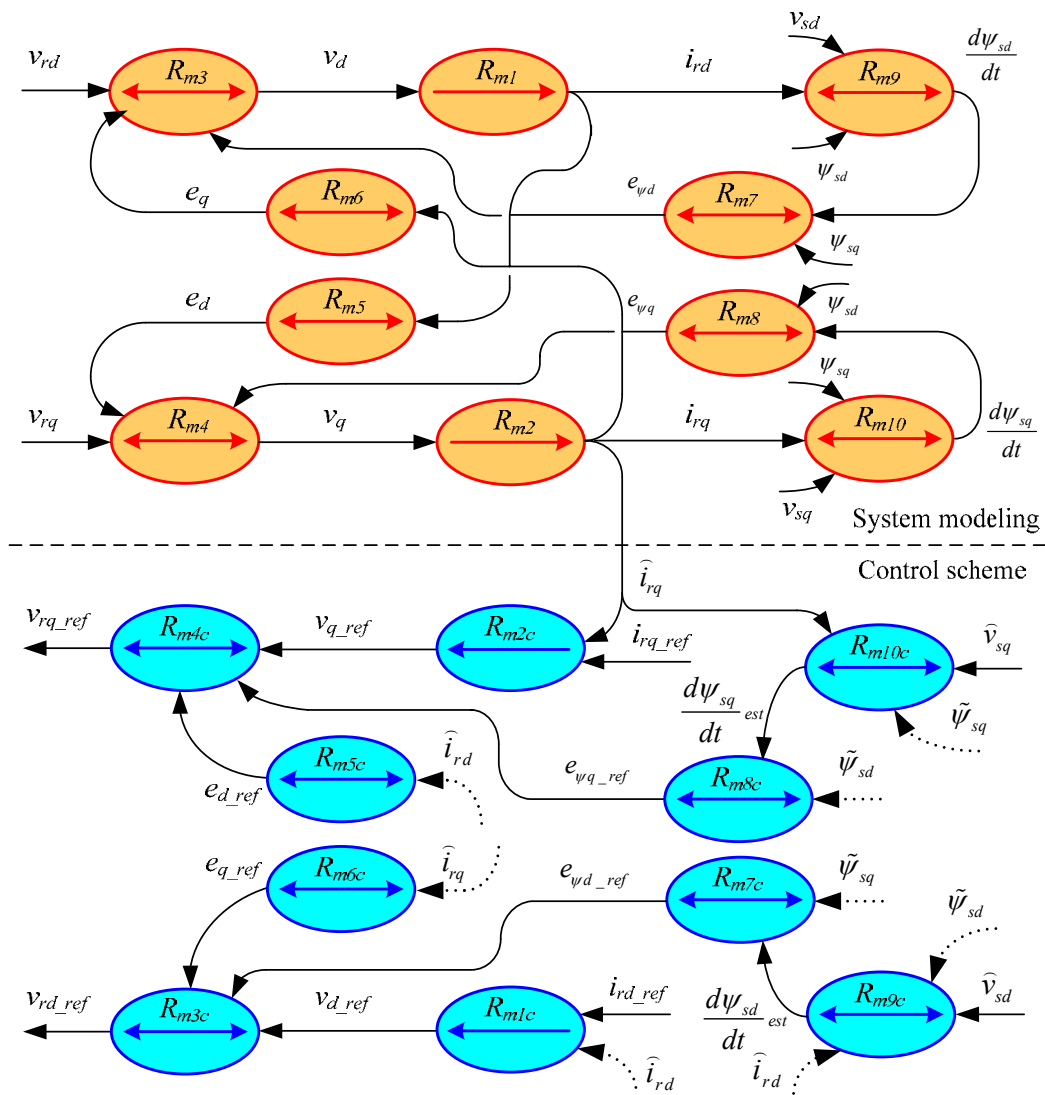


Figure III-3 : The COG of the modified vector control strategy of the DFIG
 And the related block diagram can be obtained as in figure III-4.

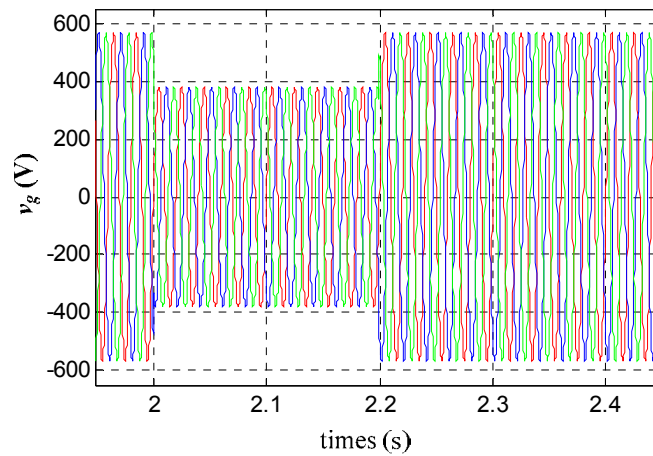


Figure III-5 : Grid voltage during a common three-phase fault

Figure II-6 shows the simulated results of the proposed vector control strategy compared to the conventional one in the synchronous frame.

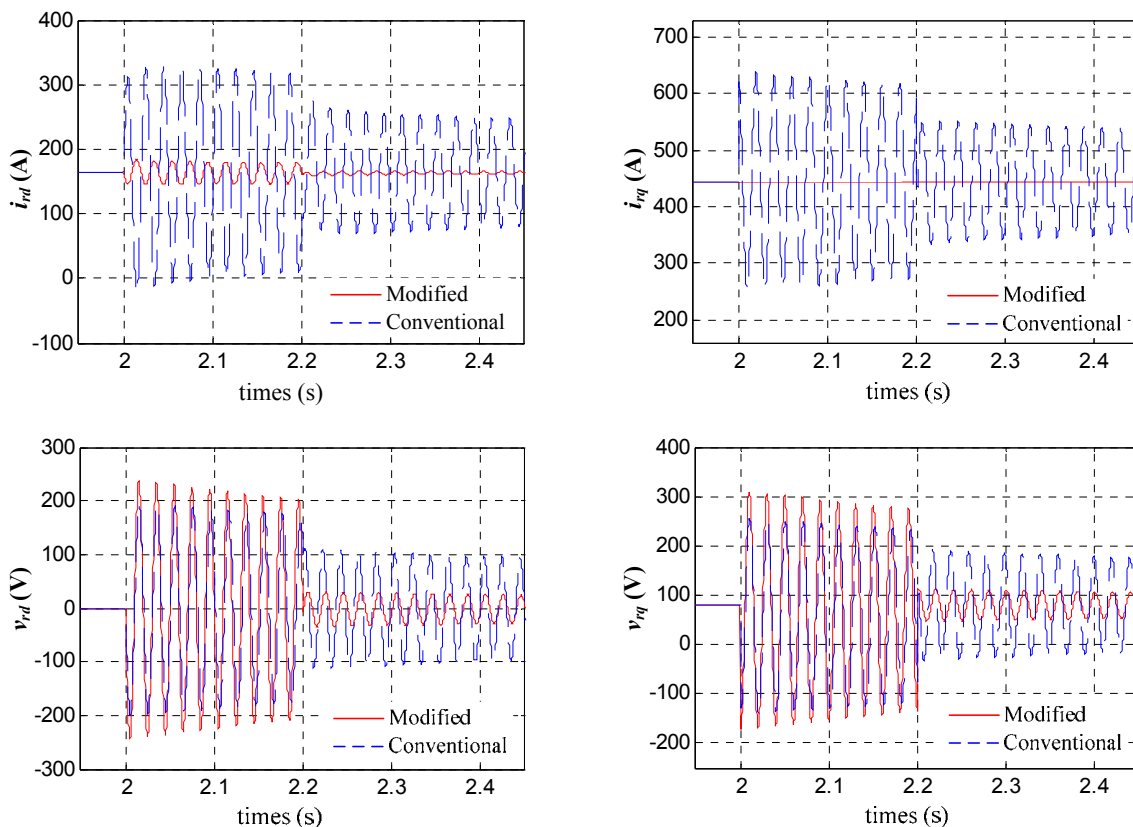


Figure III-6 : Rotor variable of the DFIG in the dq frame during the voltage dip

According to Figure III-6, the proposed control scheme results in much smaller rotor over current than the conventional one, which indicates that the modified vector control strategy can provide adequate control of the rotor current during voltage dips. In the meanwhile, the rotor voltage with the proposed control scheme is larger than that with the conventional during the voltage dip because the dynamics of the stator flux is taken into

account. Therefore, the required rotor voltage is very large during the voltage dip compared to that in normal condition. It indicates that the effective control of the rotor current is on the basis of increasing the output voltage of the rotor-side converter.

Figure III-7 compares the dynamic behavior of the wind turbine system with the modified and conventional vector control strategy. The rotor current nearly does not change with the modified control strategy while it distorts severely in conventional control scheme as we can see in the figure II-7. However, the stator current oscillates according to the used approach. The conventional control strategy results in larger oscillations and transient unbalances on this current.

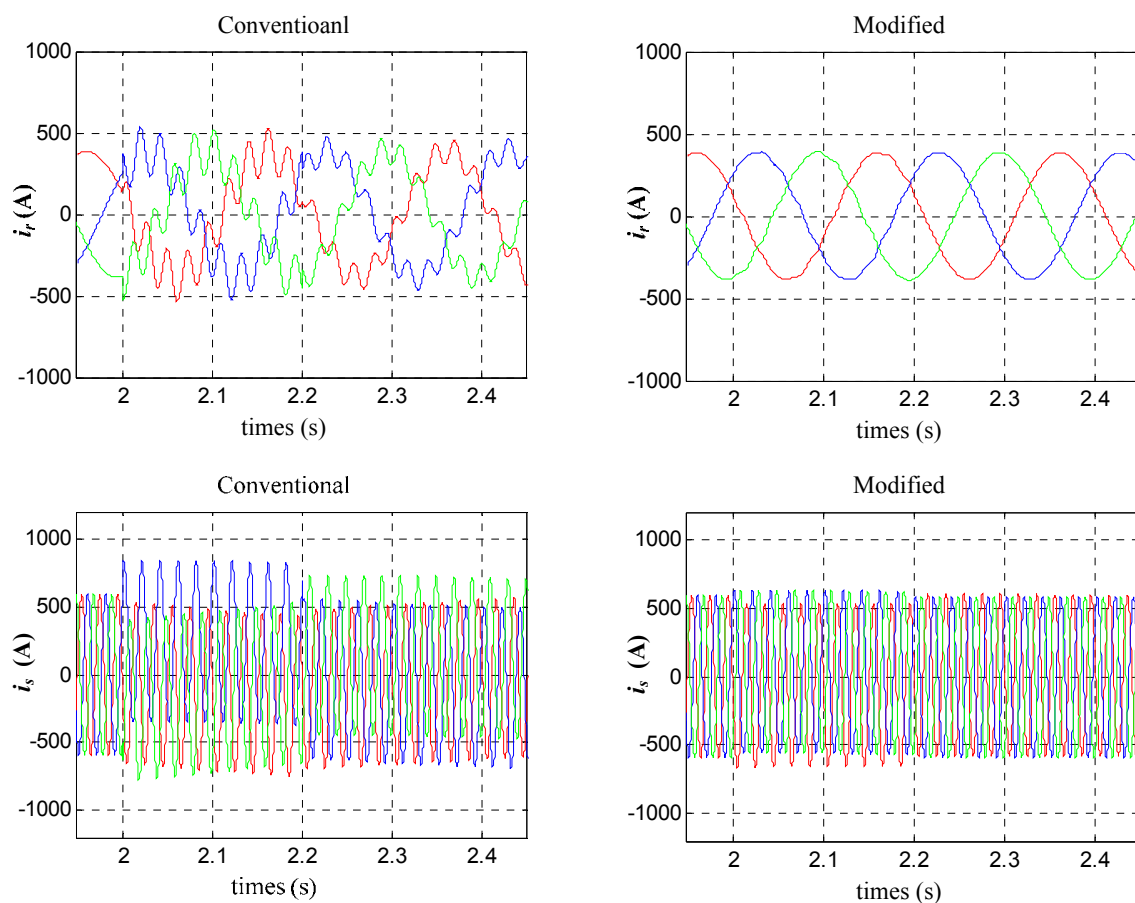


Figure III-7 : Comparison of the dynamic behavior of the DFIG during the voltage dip

Figure III-8 shows that the electromagnetic torque of the DFIG also oscillates because of the voltage dip. After a voltage dip occurs, as the stator flux drops, the generated torque will also drop. As the absorbed wind power nearly does not change during the voltage dip, the rotor will accelerate due to the mismatch between mechanical and electromagnetic torque. With the modified control strategy, the oscillation can be reduced, so that the mechanical stress to the turbine shaft will be much smaller.

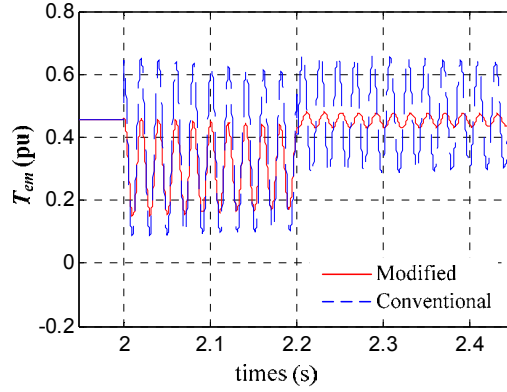


Figure III-8 : Electromagnetic torque of the DFIG during the voltage dip

Figure III-9 shows the DC bus voltage of the power converter during the voltage dip. Although the DC-link voltage increases because a significant power flow is induced to the converter, the control scheme can control it back to its reference value. Moreover, with considering the dynamics of the stator flux, the DC bus voltage is much smaller.

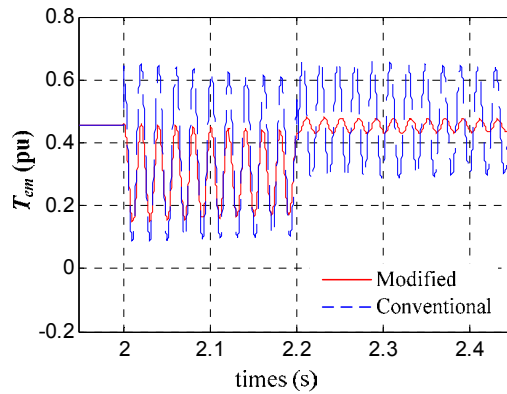


Figure III-9 : DC bus voltage of the power converter during the voltage dip

III.4. EXPERIMENTAL RESULTS.

In order to validate the proposed modified vector control strategy, experiments have been carried out on the 4.5kW DFIG laboratory test platform equipped with a voltage dip generator that is presented in Figure III-10.

It is composed by two transformers TY_1 and TY_2 , with m_1 is the voltage ratio of TY_1 and m_2 is that of TY_2 :

$$m_1 > 1, m_2 < 1, \text{ and } m_1 \cdot m_2 = 1 \quad (\text{III-83})$$

In normal operation mode, the switch K_1 is closed and K_2 is open, so that the voltage at the stator side is equal to the grid voltage. And if we open K_1 and close K_2 at the same time, a voltage dip will be created across the generator. The magnitude of the voltage dip can be

easily regulated by changing m_1 and m_2 . After K_2 is opened and K_1 is closed again, the stator voltage will recover to normal value and the voltage dip is over.

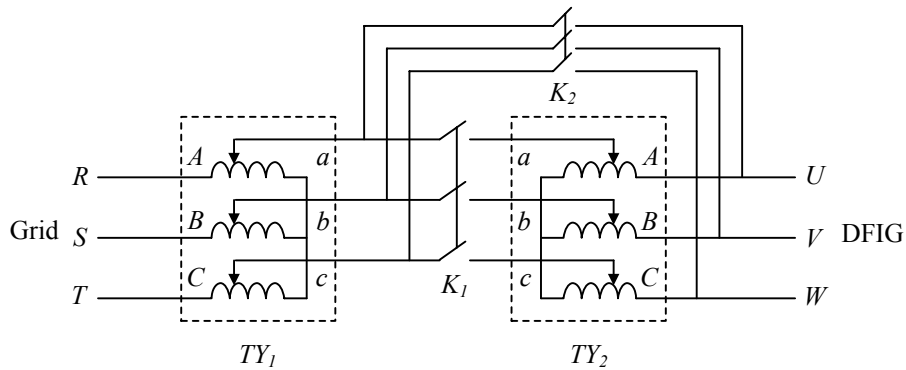


Figure III-10 : Voltage dip generator based on transformers

Figure III-11 shows the stator flux during a voltage dip of 67%. As it is shown in the figure, as soon as the stator voltage drops, an oscillation appears in the stator flux. Therefore, both the quadrature stator flux and the dynamics of the stator flux should be considered when designing the rotor current controller.

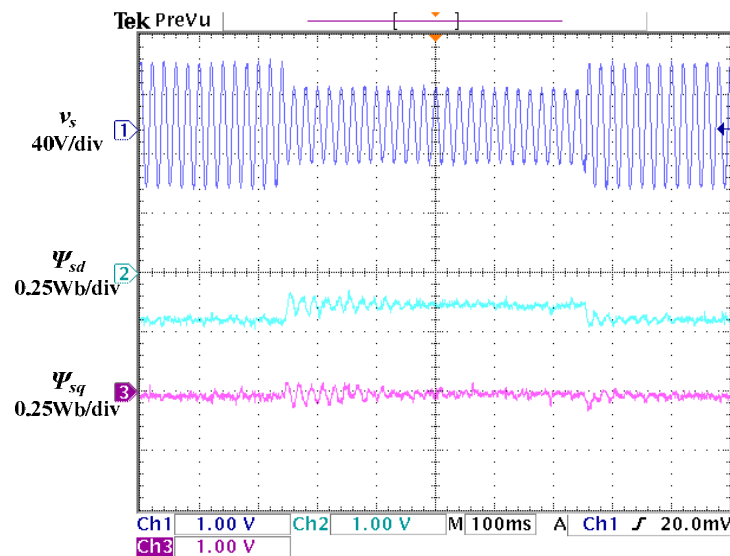


Figure III-11 : Stator flux during the voltage dip

As shown in the simulation results, the transients of rotor current is very small when the dip occurs and the voltage recovers thanks to the proposed vector control strategy according to figure III-12. Thus the rotor over-current can be effectively reduced by considering the dynamics of the stator flux (induced by the voltage dip).

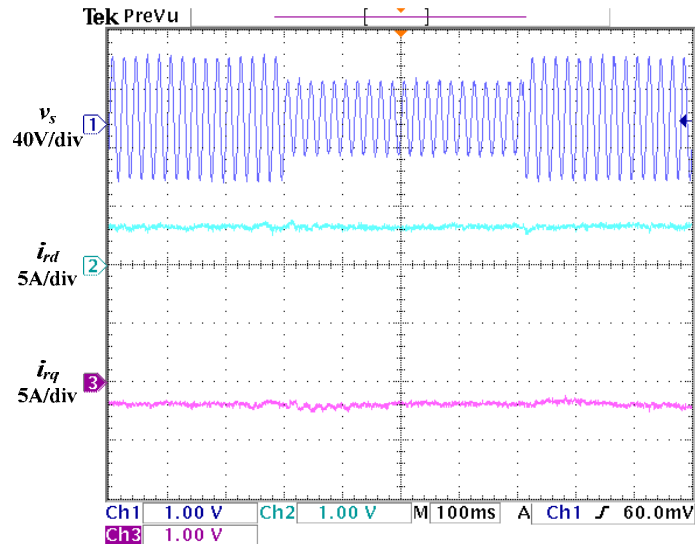


Figure III-12 : Direct and quadrature rotor current during the voltage dip

Figure III-13 shows the rotor current and stator current during the voltage dip. Although the rotor current nearly does not change with the modified control strategy, there is still an oscillation in the stator current. This is caused by the dynamic changes of the stator flux. Anyway, the LVRT capability of the DFIG can be greatly enhanced by the proposed scheme.

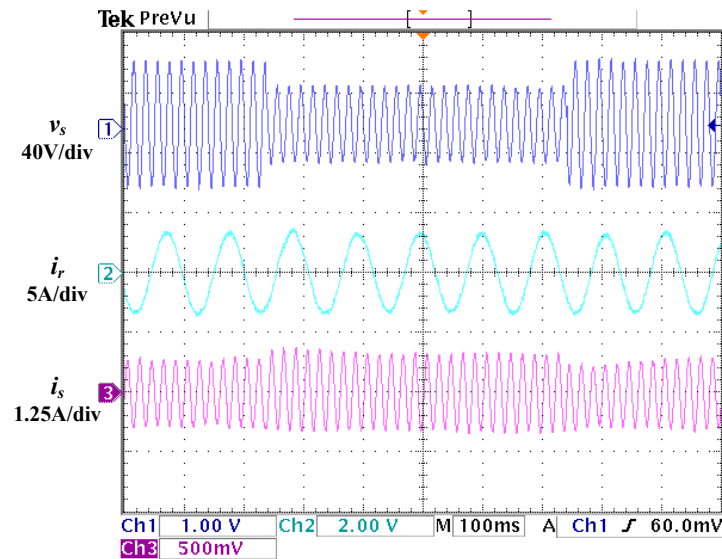


Figure III-13 : Rotor and stator current during the voltage dip

The output active power and reactive power can be seen in Figure II-14. The active power drops during the dip because the stator voltage is smaller than the rated value. Meanwhile, the generator can supply some reactive power to the grid, which can support the voltage.

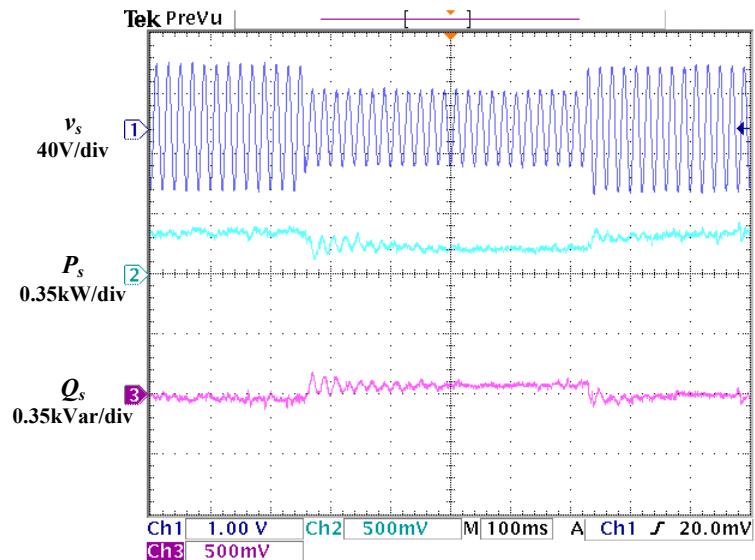


Figure III-14 : Decoupled control of active and reactive power

III.5. FEASIBILITY REGION OF THE STRATEGY.

Unfortunately, the ride-through capability of the proposed scheme is limited by the relatively small rating of the power converters compared to the whole system. The control effect is affected mainly by the severity of the fault and the generator speed (slip). The feasibility region of the proposed modified vector control strategy of the DFIG against voltage dips is therefore investigated by simulation. Although a voltage dip is commonly characterized by two parameters to quantify its severity: magnitude (or “remaining voltage”) and duration. The magnitude is only considered in our study to define the grid fault severity. And the slip covers the whole normal speed range, which is from -0.3 to 0.3. The criterion is in response to whether the rotor current is constrained to be small than 2 p.u. The obtained feasibility region against symmetrical fault is shown in Figure III-15.

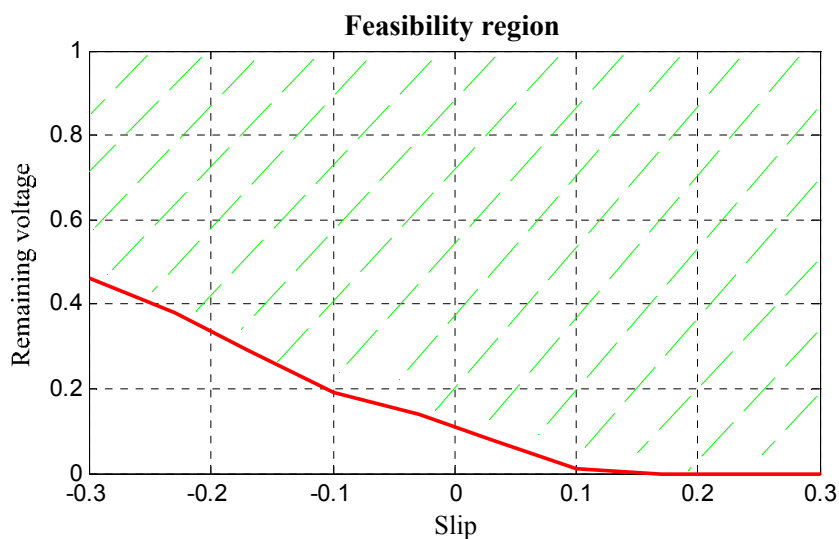


Figure III-15 : Feasibility region of modified vector control strategy

The DFIG can ride-through the voltage dip in any operation point above the red boundary. It is shown that when the generator speed is higher before the fault, the DFIG is more difficult to be accurately controlled. This is because the generator is prescribed to supply more active power at a high speed, which means that the rotor current is also controlled to be larger before the fault occurs.

III.6. CONCLUSION.

When the situation after the fault is not enough serious, the proposed control strategy, which takes the dynamics of the stator flux into account and can provide adequate control of the DFIG during voltage dips. The over current in the rotor windings and over voltage in the DC bus can be well limited thanks to the modified control strategy, which can improve the LVRT capability of DFIG based wind turbines. However, its capability is limited by the relatively small rating of the power converters compared to the DFIG. When the grid fault is serious enough, the rotor current will increase and will be too large to be controlled by the power converters because they have a current limitation. Therefore, the feasibility region in terms of the fault severity and generator speed of the modified control scheme is obtained by simulations. It is shown that the most challenging operation situation is with the maximum generator speed.

CHAPITRE IV

PERFORMANCE OF THE DFIG DURING VOLTAGE DIPS WITH AN ACTIVE CROWBAR

Although the modified vector control strategy can provide adequate control of the DFIG during grid voltage dips, its ride-through capability is limited by the relative small rating of the rotor side converter compared to the generator rating. If the depth of the dip is small and the required voltage does not exceed the maximum voltage that the rotor side converter can generate, the current remains controlled. But for larger dips, an increased rotor voltage will be needed to control the rotor currents. When this required voltage exceeds the voltage limit of the converter, it is not possible any longer to control the current as desired. It is confirmed that if the stator voltage decreases to zero, the required rotor voltage is close to the stator rated voltage instead of the small percentage induced in normal operation [110]. So, a converter with a rated power similar to that of the generator is required therefore the advantages of this wind energy conversion structure are lost. Therefore, an additional protection device is always needed in the case of large voltage dips. Protection devices such as crowbar circuits [111-114], energy storage system [115], stator switches [116] and auxiliary parallel grid-side rectifier [117] have already been used to protect DFIG during grid faults. In this chapter, an active crowbar protection system will be modeled. And then an improved control strategy for the crowbar protection coordinated with a demagnetization method of the DFIG and voltage support by both the generator and the grid-side converter will be proposed to enhance the ride-through capability.

IV.1. CROWBAR PROTECTION CIRCUIT.

Crowbar protection systems are commonly used to protect the power converters during voltage dips. The key of this solution is to limit the high current in the rotor and the high voltage across the DC bus. With a crowbar protection circuit, it is possible to ride-through grid faults without disconnection of the turbine from the grid.

IV.1.1. Development of the crowbar circuit.

The crowbar circuit is usually implemented between the rotor circuit and rotor-side converter to provide a bypass for the high transient rotor current, which is induced by voltage dips. Initially, the industrial solution implemented was just to short circuit the rotor windings with the crowbar circuit. This conventional crowbar circuit can be constructed in many ways, as illustrated in Figure IV-1 [111].

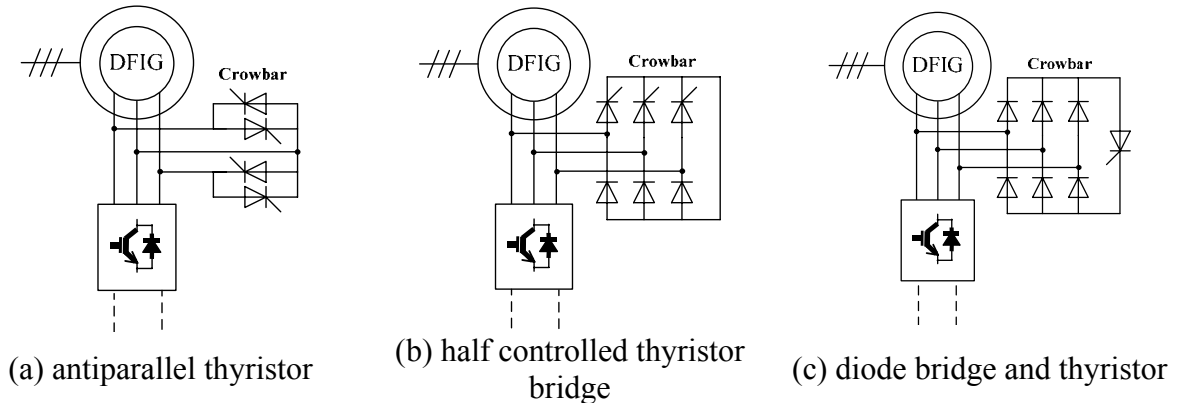


Figure IV-1 : Conventional crowbars

In Figure IV-1(a), the rotor can be short-circuited by two pairs of antiparallel thyristors connected between the phases. Another alternative is to use a half-controlled thyristor bridge, as it is shown in Figure IV-1(b). The third possibility as in Figure IV-1(c) is to rectify the phase currents with diode bridge and to use a single thyristor to trigger the crowbar. The main drawback of this solution is that the wind turbines are not able to resume in normal operation cooperating with the grid because of its turn-off problem. For crowbars of Figure IV-1(a) and (b), because the rotor currents may have a significant DC component, the phase current reversals that would turn the thyristors off do not exist when they would be needed. And for the crowbar of Figure IV-1(c), as the current through the thyristor is continuous, it does not allow the thyristor to turn off. Moreover, the snubber design for the thyristors of the crowbar may be problematic. In order to fulfill the newest grid codes, the crowbar circuit should be tripped off after the clearance of the grid faults. Thus fully controllable semiconductor switches are needed to construct an active crowbar [112]. From the conventional crowbars, the antiparallel thyristor one is difficult to convert into active crowbar because of the large number of the controlled components. The same problem is faced by the half-controlled bridge one. However, the crowbar circuit with a diode bridge has only one controlled component, thus it is optimal in this transformation. Either a GTO or an IGBT can be used as the fully controllable switch for the active crowbar circuit, as it is shown in Figure IV-2 (a) and (b). As an improvement on the active crowbar, resistances are added to the crowbar to restrict the high rotor current. This solution is most widely used by the manufacturers nowadays. Another kind of improved active crowbar can be constructed by three-phase AC switches and resistors, as illustrated in Figure IV-2 (c).

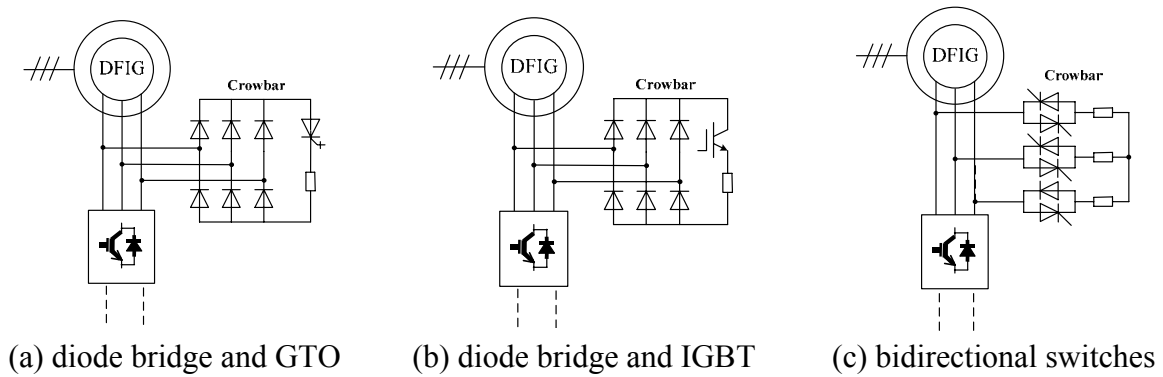


Figure IV-2 : Improved active crowbars

With this improved crowbar, the wind turbine can remain connected to the grid during the dips. Because of the generator and converter can stay connected during the grid fault, they can resume in normal operation immediately after the fault has been cleared. Recently, there are some papers that discuss the protection scheme of the DFIG with active crowbars during grid disturbances. However, most papers give little information of the protection scheme that is implemented [118-123].

DC side crowbar consists of a chopper and a resistor that are added across to the DC bus of the converter. It can limit the DC voltage from exceeding safe range, as shown in Figure IV-3. The chopper module is not essential for fault ride-through operation but it increases the normal range of DFIG operation by smoothing the dc-link voltage during heavy imbalances of active power on the rotor side and grid side converters. The rotor side converter has to be dimensioned to handle the high current transients in addition to the normal load. Thus oversized components have to be used and makes this scheme unattractive [111]

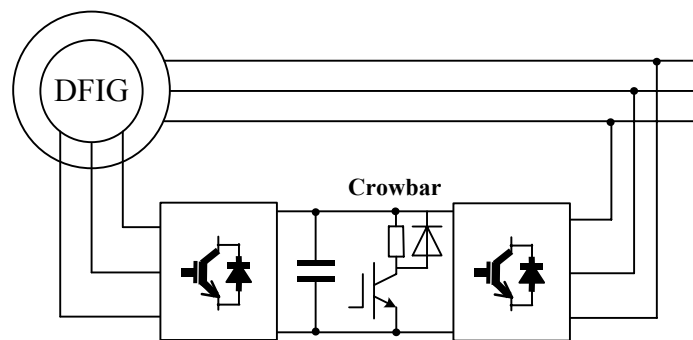


Figure IV-3 : DC side crowbar

IV.1.2. Modeling of the active crowbar.

As we can see in Figure IV-4, the crowbar protection circuit is connected between the rotor of DFIG and the rotor-side converter.

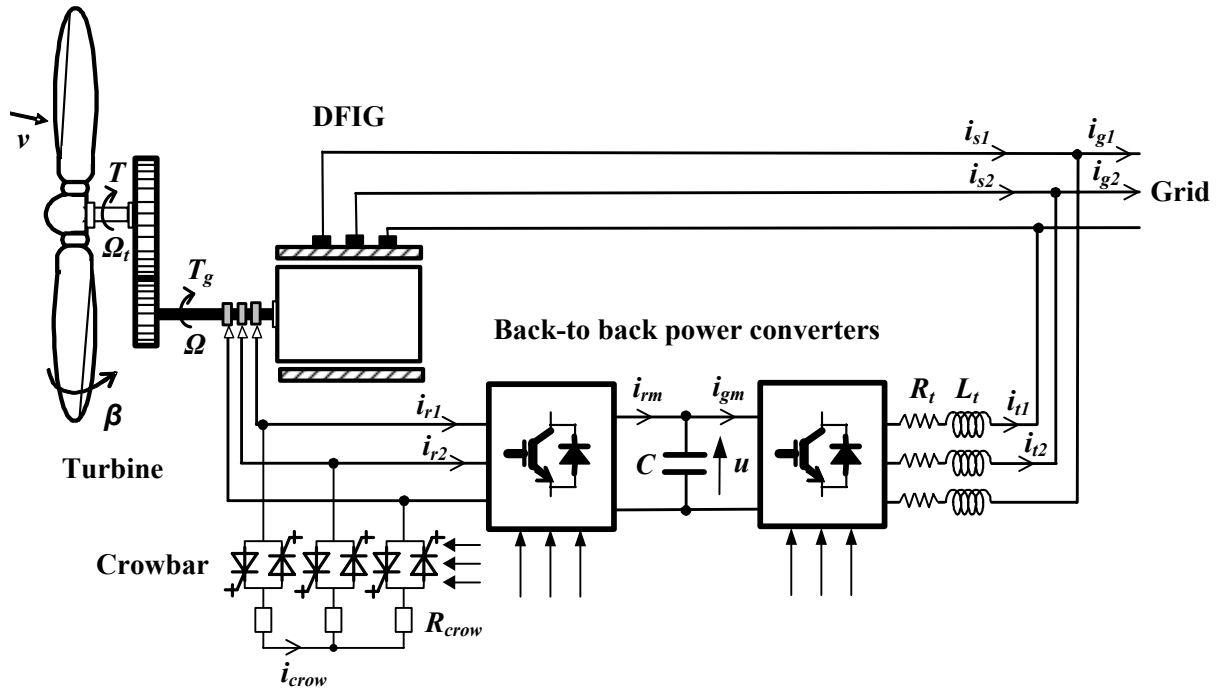


Figure IV-4 : DFIG based wind turbine with crowbar protection

The crowbar protection circuit is composed of three phase bidirectional switches and bypass resistors. The semiconductors are considered to be ideal and a switching function s_c is defined for the switches, which takes the values 1 when the switch is closed and 0 when it is open. Then Crowbar protection component can be modeled by a simple equation as:

$$v_{crow} = s_c R_{crow} i_{crow} \quad (IV-84)$$

The behavior of such systems during grid faults is greatly affected by the resistor value of crowbar. It has been shown by simulation in [124] that a low crowbar resistance leads to a higher electrical torque, over currents and low rotor voltages. High values for the crowbar resistor will result in a lower electrical torque and rotor currents but also higher rotor voltages. Therefore, the crowbar resistors should be sufficiently low to avoid large voltages on the converter terminals. On the other hand, they should be high enough to limit the rotor current. In our study, this resistance value is chosen to be equal to $30 R_r$.

IV.2. SYNTHETIC CONTROL AND PROTECTION STRATEGY.

Although there are many papers, which discuss the control and protection strategy of the DFIG under grid faults, the most of them gives little information of the protection scheme that is implemented. In this chapter, a hysteresis control strategy of crowbar circuit is designed to protect the system in serious grid faults. And a demagnetization method of the DFIG is adopted to decrease the oscillations of the transient current. Moreover, the grid voltage can be supported by both the generator and the grid-side converter.

IV.2.1. Hysteresis control of the crowbar.

Commonly the crowbar is triggered in case of over voltage across the DC bus or over current in rotor windings. When the crowbar is triggered, the rotor side converter will be disconnected from the rotor circuit at the same time. As a result, the controllability of the DFIG is lost during the voltage dip, which is the main drawback of the crowbar protection. Moreover, the DFIG then behaves as a classical squirrel cage induction generator with a variable rotor resistance until the crowbar is cut off and the rotor side converter resumes normal operation. In this situation, the DFIG absorbs reactive power from the grid for magnetization, which will even deteriorate the stability of the weak grid. Therefore it is better to reduce the activation time of crowbar.

In order to reduce the operation time of the crowbar, an improved hysteresis control strategy is adopted, as it is shown in Figure IV-5. The maximum absolute value of rotor current $|\hat{i}_r|_{\max}$ is compared with a threshold value i_{th} and a safety value i_{sa} . If $|\hat{i}_r|_{\max}$ is greater than i_{th} , the crowbar is activated for protecting the power converters. And when $|\hat{i}_r|_{\max}$ decreases to be less than i_{sa} , the crowbar will be cut off and the rotor side converter is restarted to control the DFIG.

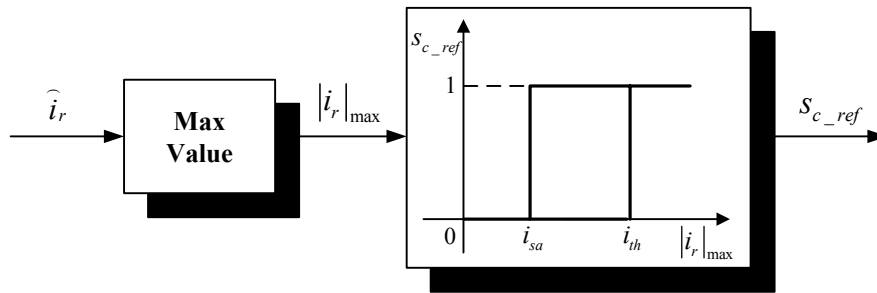


Figure IV-5 : Hysteresis control of the active crowbar

IV.2.2. Demagnetization control of the DFIG.

During a symmetrical voltage dip, the transient stator flux can be divided into two parts: the forced flux ψ_{sf} and the natural flux ψ_{sn} , which can be defined as [1]:

$$\vec{\psi}_s = \vec{\psi}_{sf} + \vec{\psi}_{sn} = \frac{V_2}{j\omega_s} e^{j\omega_s t} + \frac{V_1 - V_2}{j\omega_s} e^{-t/\tau_s} \quad (\text{IV-85})$$

Where V_1 is the voltage magnitude before the fault whereas V_2 is the magnitude of the remaining voltage. ω_s is the synchronous speed and $\tau_s = -R_s / L_s$.

It is shown that the oscillations of the stator and rotor current come from the dc component of the stator flux ψ_{sn} . Thus a demagnetization method can be designed to compensate for the natural flux. This method is based on a closed-loop control of the stator flux, which gives the reference of the rotor current:

$$i_{rd_ref} = C_\psi [\psi_{sd_ref} - \psi_{sd_est}] \quad (\text{IV-86})$$

$$i_{rq_ref} = C_{\psi} [\psi_{sq_ref} - \psi_{sq_est}] \quad (\text{IV-87})$$

Where $C_{\psi}[X_{ref} - X_{est}]$ is the mathematical equation of a PI controller, ψ_{sd_est} and ψ_{sq_est} are the estimated flux. In order to count the natural flux, the stator flux references are set to be equal to the forced flux according to the remained voltage:

$$\psi_{sd_ref} = \psi_{sfd} = \frac{V_2}{\omega_s} \quad (\text{IV-5})$$

$$\psi_{sq_ref} = \psi_{sfq} = 0 \quad (\text{IV-6})$$

This method is used as soon as a voltage dip is detected and a few hundred milliseconds after the clearance of the fault in order to avoid large transients.

IV.2.3. Grid voltage support.

The voltage control strategy is proposed to deal with the reactive power contribution, which is performed by both the DFIG and the grid-side converter in a coordinated manner.

If the voltage dip lasts for a long time, the crowbar can be removed and the rotor-side converter is restarted to control the DFIG to supply maximum reactive power to the grid. In the meantime, the grid-side converter is also controlled to supply the reactive power in order to enhance the grid voltage support capability of the total system.

Therefore, the proposed synthetic LVRT strategy for the DFIG based wind turbine system can be illustrated as figure IV-6.

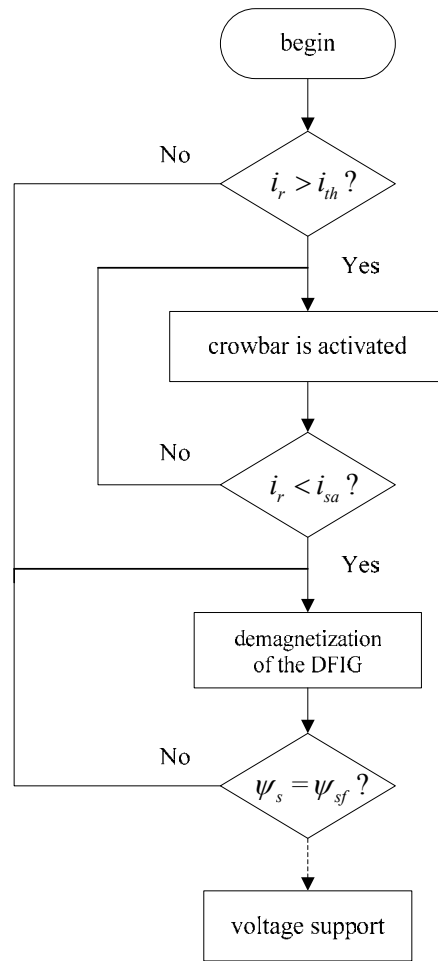
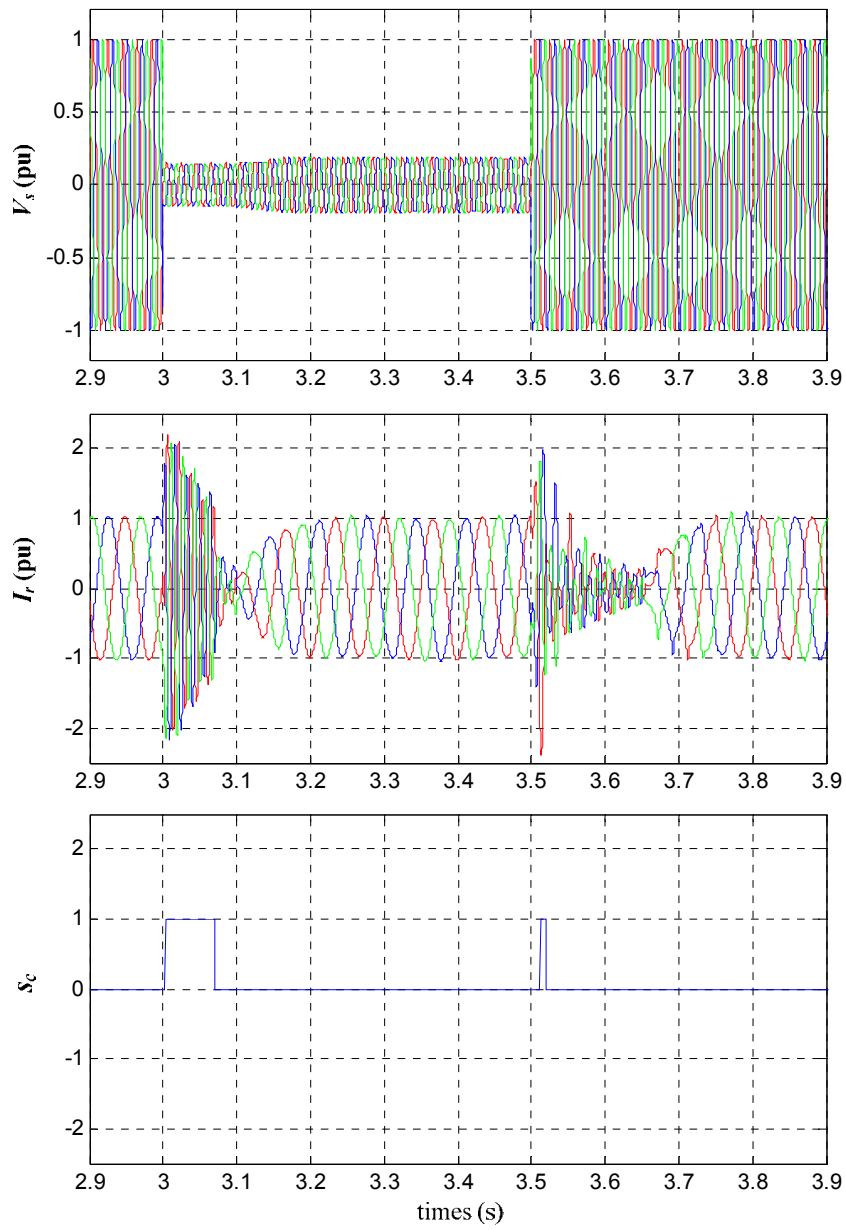


Figure IV-6 : Synthetic LVRT strategy of DFIG system

It should be noticed that when the grid voltage recovers just after the fault has been cleared, the active crowbar is also needed to protect the system. The synthetic control and the protection progress are almost the same as when the voltage dip occurs except that the grid support control is no longer included.

IV.3. SIMULATION RESULTS.

In order to validate the proposed strategy, a serious grid fault is taken into account, which causes the voltage drop to 15% of its nominal value and last for 500 ms. As the most challenging operation situation is with the minimum slip, the generator speed is supposed to be at the rated speed of 1950 r/min.



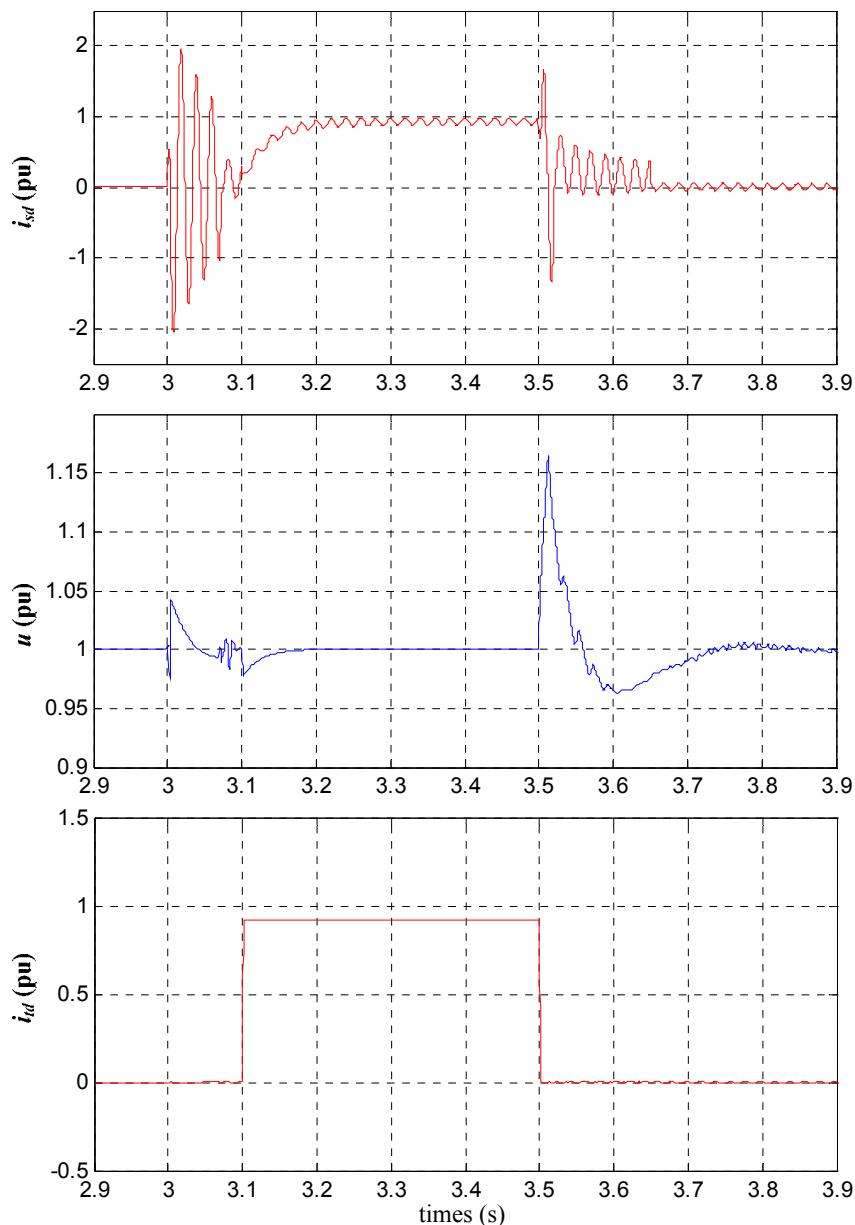


Figure IV-7 : Simulation results under a voltage dip of 85% which lasts for 0.5 s

Figure III-7 shows the simulated results of the LVRT operation with the proposed strategy. As soon as the voltage at the wind turbine terminal drops at 3 s, the demagnetization method is adopted, but the rotor current still exceeds the threshold value because of the limited capability of the power converter. Thanks to the crowbar protection, the rotor current decreases to the secure region rapidly. And the crowbar only works for a few milliseconds. So the DFIG is controllable for most of the time during the voltage dip. As a result, less reactive power will be absorbed during the demagnetization, which controls the stator flux equal to the forced flux value during the fault. In addition, in most time of the voltage dip, the system can supply reactive power from both the generator and the grid-side converter to the weak grid, which increases the grid voltage and help the grid recovery.

The supplied reactive power is not as large as in normal grid condition due to the reduced grid

voltage. Because of the demagnetization method, the DFIG can resume normal operation about 0.25 s after the grid voltage recovers. But it should be noticed that larger transients still appear at the moment when the dip is cleared.

IV.4. CONCLUSION.

A synthetic control and a protection strategy are proposed for the DFIG wind turbine system, which is equipped with an active crowbar. In order to reduce the activated time of the crowbar as much as possible, an improved hysteresis control strategy is proposed. Moreover, a demagnetization method is proposed to decrease the oscillations of the transient current both during the voltage dips and after the clearance of the faults. It is based on a closed-loop control of the stator flux. With the cooperation of this two control schemes, the DFIG is controllable for most of the time during voltage dips while the crowbar provides sufficient protection. So that the DFIG can provide reactive power to the weak grid during voltage dips. In the meantime, the grid-side converter is also controlled to supply reactive power in order to enhance the grid voltage support capability of the total system. Moreover, the wind turbine system can resume normal operation in a few hundred milliseconds after the fault is cleared.

CHAPITRE V

RECONFIGURATION OF CONTROL STRATEGIES FOR HIGH POWER DFIG SYSTEM

Nowadays, there is a tendency to increase the size and the power rating of wind turbines. For example, the 5MW wind turbine of REpower and 6MW wind turbine of Enercon have already been installed. This kind of high power wind turbine system is especially suitable for off-shore application, since the installation and maintenance costs for one turbine can be reduced. Due to their advantageous characteristics, most of the grid-connected wind turbines operate at a variable speed at present. The power electronic technology plays an important role in variable-speed wind power generation in order to match the intermittent wind source characteristics as well as meet the grid connection requirements [125-126]. For such high power applications, parallel power electronic structures with multilevel converters are preferred due to their significant advantages as they can increase the output voltage magnitude, reduce the output voltage and current harmonics without increasing the switching frequency or decreasing the output power [127]. In addition, they present better efficiency as converter losses are reduced. Thus multilevel converters, especially three-level converters, are a realistic alternative to conventional converters in high power wind energy applications [128-129]. This chapter aims to implement a reconfiguration scheme of control strategies on DFIG based high power wind turbine system in order to enhance the ride-through capability and fulfill the grid code requirements.

V.1. MODELING OF THE THREE-LEVEL CONVERTER.

Figure V-1 illustrates the overall wind generation system. Unlike the conventional one, high power DFIG wind turbine uses back-to-back three-level Neutral Point Clamped (NPC) power converters.

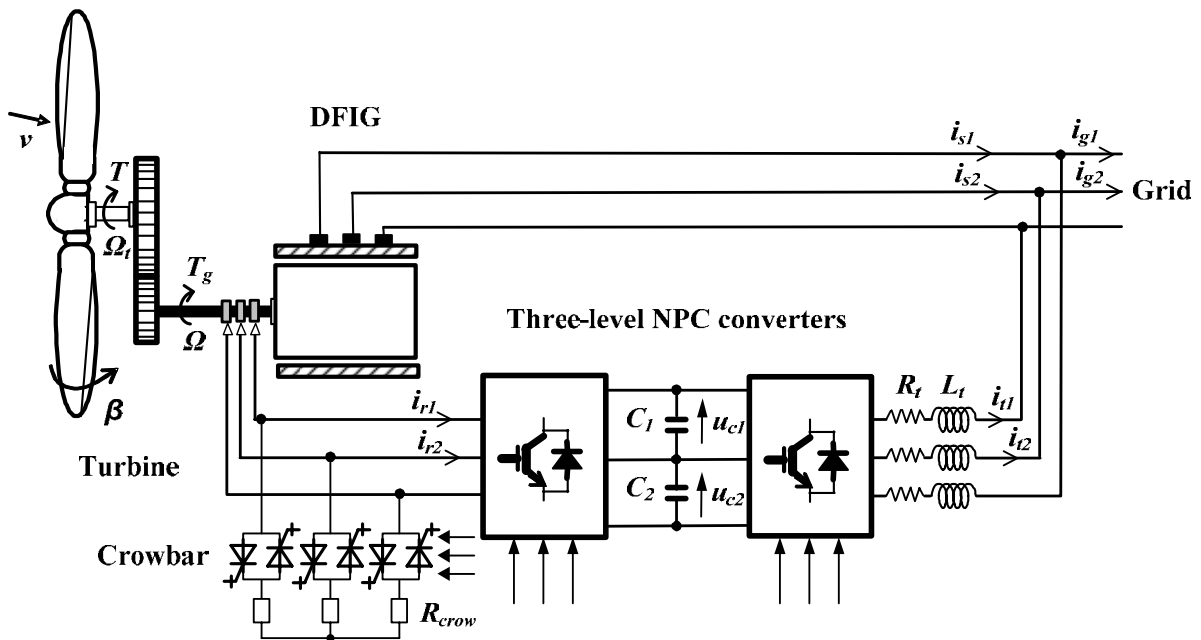


Figure V-1 : High power DFIG wind turbine system using three-level NPC converters

The topology of a three-level NPC converter consists of three commutation circuits, which are fed with a capacitive divider, as it is shown in Figure V-2. To produce three voltage levels, two capacitors are connected in series to a dc voltage source u_{dc} .

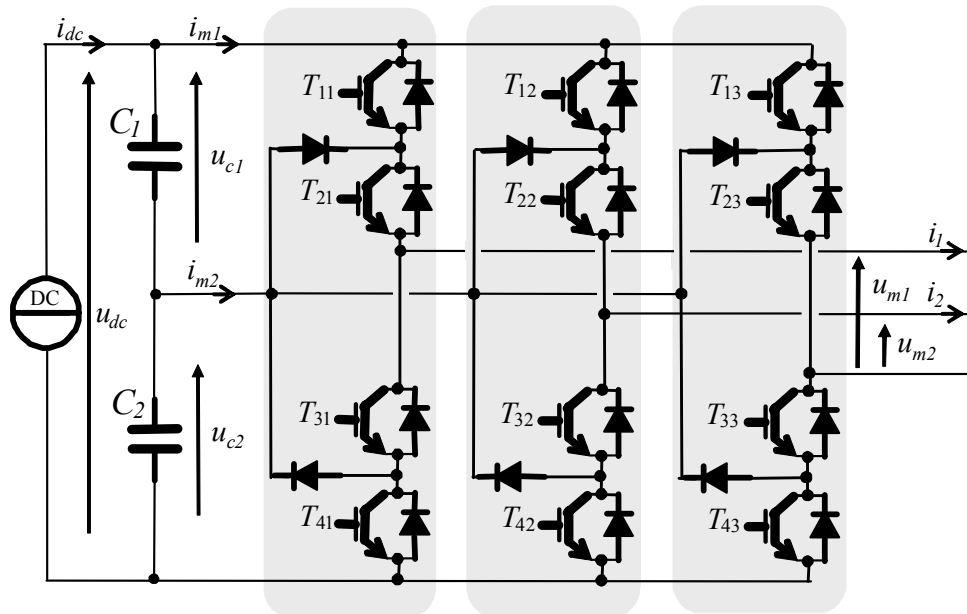


Figure V-2 : Schematic diagram of a three-level NPC converter

For the modeling of power electronic converters semiconductors are considered ideal: no power dissipation and instantaneous commutations. Then the clamped commutation circuit is equivalent to a commutation circuit with three ideal switches. And one ideal switch among the three must be at any time switched on.

By considering a continuous conduction mode of semiconductors, an equivalent matrix converter with ideal switches as in Figure V-3 can be considered for an easier study.

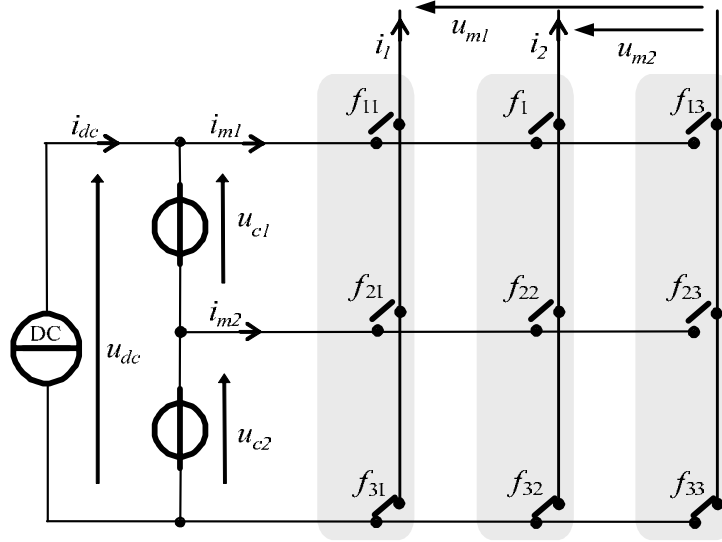


Figure V-3 : Equivalent matrix structure of the three-level converter

A switching function f_{ij} is defined for each power switch. It represents the ideal commutation orders and takes the values 1 when the switch is closed and 0 when it is open:

$$f_{ij} \in \{0,1\}, \text{ with } \begin{cases} i \in \{1,2,3\} \text{ number of the leg} \\ j \in \{1,2,3\} \text{ number of the switch in the leg} \end{cases} \quad (\text{V-88})$$

This defined switching function is the theoretical (and considered effective) state of the switch. In each commutation circuit, the last switching function is decided by the other ones as:

$$f_{3j} = \bar{f}_{1j} \cdot \bar{f}_{2j}, j \in \{1,2,3\} \quad (\text{V-89})$$

The modulated voltages may be written as a product of the DC bus voltages (u_{c1} and u_{c2}) and modulation functions, which can be defined from switching functions [130]:

$$m = \begin{bmatrix} m_{11} & m_{12} \\ m_{21} & m_{22} \end{bmatrix} = \begin{bmatrix} 1 & 0 & -1 \\ 0 & 1 & -1 \end{bmatrix} \begin{bmatrix} f_{11} & f_{21} \\ f_{12} & f_{22} \\ f_{13} & f_{23} \end{bmatrix} \quad (\text{V-90})$$

Then the modulated voltages and current of the three-level NPC converter can be expressed as:

$$u_m = \begin{bmatrix} u_{m1} \\ u_{m2} \end{bmatrix} = m \begin{bmatrix} u_{c1} + u_{c2} \\ u_{c2} \end{bmatrix} = mu \quad (\text{V-91})$$

$$i_m = \begin{bmatrix} i_{m1} \\ i_{m2} \end{bmatrix} = m^T \begin{bmatrix} i_1 \\ i_2 \end{bmatrix} = m^T i \quad (\text{V-92})$$

In this way, the rotor-side and grid-side converter can be modeled respectively as:

$$\begin{cases} u_{rm} = m_r u \\ i_{rm} = m_r^T i_r \end{cases} \quad (\text{V-93})$$

$$\begin{cases} u_{tm} = m_g u \\ i_{gm} = m_g^T i_t \end{cases} \quad (\text{V-94})$$

With u_{rm} and u_{gm} are the output line voltages of rotor side and grid side converters, i_{rm} and i_{gm} are the modulated currents of relevant power converters respectively, i_r is the rotor current and i_t is the current in the choke.

As line modulated voltages are balanced, line voltages can then be expressed by:

$$v_r = \frac{1}{3} \begin{bmatrix} 2 & -1 \\ -1 & 2 \end{bmatrix} u_{rm} \quad (\text{V-95})$$

$$v_t = \frac{1}{3} \begin{bmatrix} 2 & -1 \\ -1 & 2 \end{bmatrix} u_{tm} \quad (\text{V-96})$$

Where v_r and v_t are the output line phase voltages of rotor side and grid side converters.

As shown in Figure V-4, the DC bus of back-to-back three-level NPC converters is shared with two capacitors.

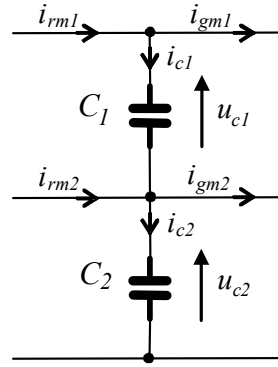


Figure V-4 : DC bus of the three-level NPC converter

From the Kirchhoff's current law, the voltage dynamics of the capacitors can be obtained as follows:

$$\begin{cases} i_{c1} = i_{rm1} - i_{gm1} \\ i_{c2} = i_{rm2} + i_{c1} - i_{gm2} \\ C \frac{d}{dt} u_{c1} = i_{c1} \\ C \frac{d}{dt} u_{c2} = i_{c2} \end{cases} \quad (\text{V-97})$$

With C is the capacity value of each capacitor ($C = C_1 = C_2$).

In this way, the three-level converter can be modeled by the same graphical descriptions as the conventional one in Chapter I.

V.2. CONTROL STRATEGY OF THE SYSTEM.

The EMR of the whole system is depicted in Figure IV-5. As the power converters have two independent switching functions F_r and F_g , two separated tuning chains can be chosen to control the system and to achieve the objective. One is an electromechanical chain F_r, V_r, T_{em} , and the other one is an electrical chain F_g, V_i, I_i . In the meantime, a mechanical tuning chain $\beta, T, \Omega_t, \Omega$ can be obtained to control the pitch angle. By using inversion rules on these three chains, a Maximum Control Structure (MCS) can be obtained from the EMR.

The pitch angle control is implemented to prevent over-speeding of the turbine by setting the speed reference to the maximum value. The rotor-side converter is designed to control the electromagnetic torque and the stator reactive power respectively. Meanwhile the grid side converter keeps the DC-link voltage constant and guarantees a converter operation with a wished power factor. Since the these two control strategies are based on regulating the related currents, a Space-Vector Hysteresis Current Control (SVHCC) with a neutral point voltage balancing can be applied on the three-level NPC converters. Therefore, a simplified control structure can be obtained, as it is depicted in Figure V-5.

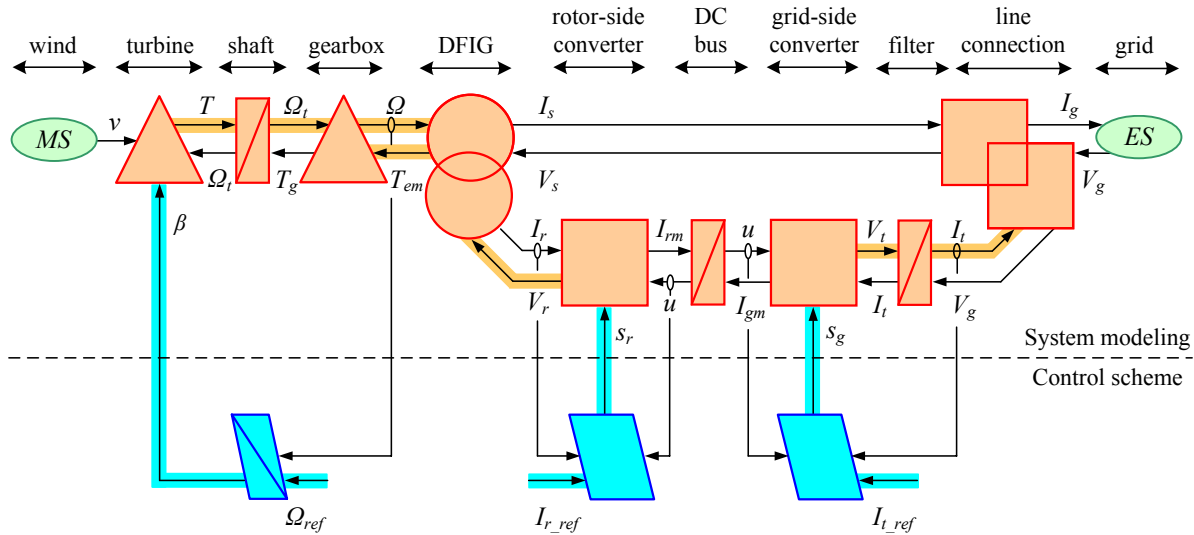


Figure V-5 : Macroscopic representation of the system model with the control scheme of the system

V.2.1. Space-vector hysteresis current control.

Conventional DFIG vector control system is usually based on a rotor current controller with $d-q$ decoupling. However, its performance depends highly on accurate generator parameters and deteriorates greatly in the case of grid voltage dips. The main advantages of hysteresis current control are simplicity, outstanding robustness, lack of tracking errors, independence of load parameter changes and extremely good dynamics limited only by the switching speed and the load time constant [132-134]. The switching frequency can be reduced effectively by means of using space-vector while increasing the used coefficient of the DC bus [135-136]. Therefore, a Space-Vector Hysteresis Current Control (SVHCC)

strategy is proposed to control the three-level converter instead of the conventional current controller.

The basic idea of the proposed hysteresis current control is to keep the measured rotor currents within their hysteresis boundaries r_1, r_2 as well as to balance the neutral point voltage. Figure V-6 illustrates the general control scheme of the NPC inverter. The proposed SVHCC consists of four blocks: error calculation, area detection, sector detection and voltage vector selection.

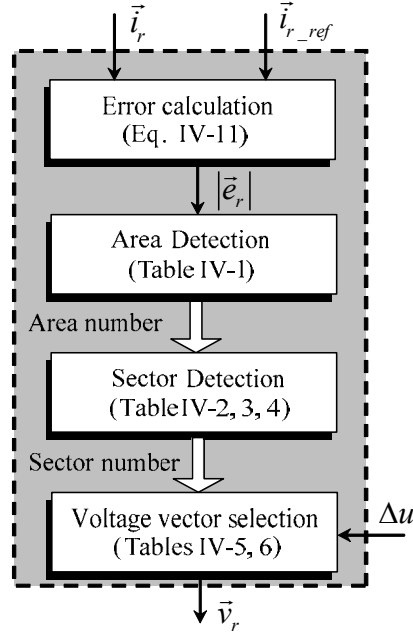
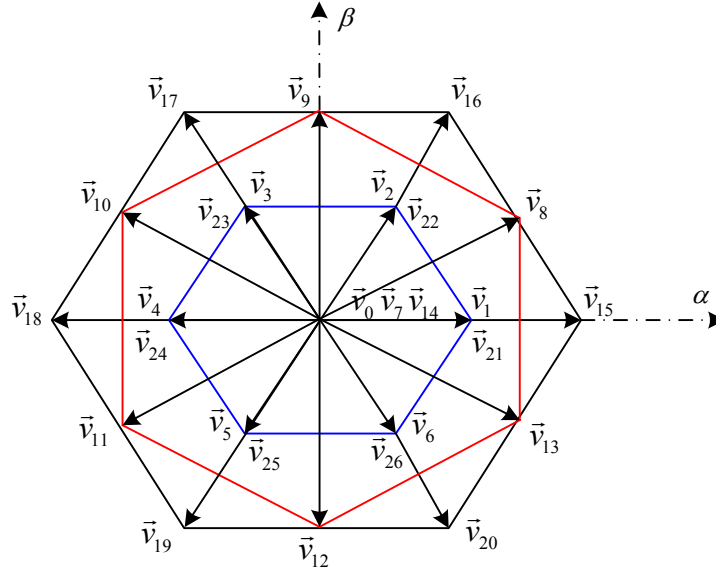


Figure V-6 : General scheme of Space-Vector Hysteresis Current Control

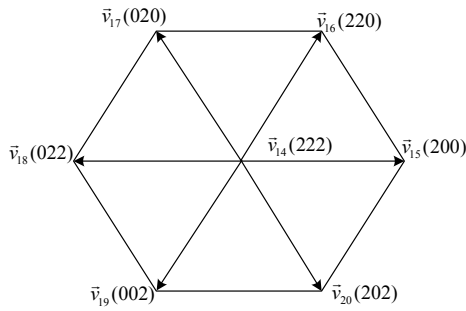
The reference and the measured rotor currents are transformed into a $\alpha\text{-}\beta$ reference frame. Then the error vector is defined as:

$$\vec{e}_r = \vec{i}_r - \vec{i}_{r_ref} = \vec{e}_{r\alpha} + j\vec{e}_{r\beta} \quad (\text{V-98})$$

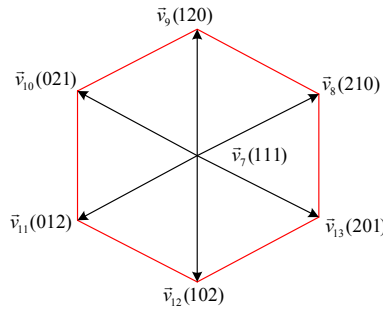
The 27 switching states of the NPC inverter result in 27 voltage vectors. Among these vectors, 3 are zero voltage vectors and 24 are non-zero voltage vectors. By drawing these 27 voltage vectors in the $\alpha\text{-}\beta$ frame, three hexagons are distinguished (large, medium and small) as illustrated in Figure V-7.



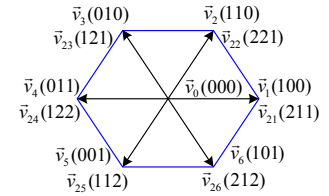
(a) The three distinguished hexagons



(b) Large hexagon



(c) Medium hexagons



(d) Small hexagons

Figure V-7 : Three-level converter voltage vectors

As it is illustrated in Figure V-8(a), the tip of the reference current vector \vec{i}_{r_ref} is located in the center of area I whereas the tip of the measured current \vec{i}_r can be located in one of the three areas (I, II, and III), which are limited by the hysteresis boundaries r_1, r_2 respectively. The values of r_1 and r_2 depend on the value of the current reference and on the desired control dynamics. Two hysteresis bands are chosen in order to use three categories of available voltage vectors, which are zero, small, medium and large. Table V-1 summarizes the conditions that must be satisfied for the error vector to be located in each particular area.

Condition	Area
$ \vec{e}_r < r_1$	Area I
$r_1 < \vec{e}_r < r_2$	Area II
$ \vec{e}_r > r_2$	Area III

Table V-1 : Areas and corresponding conditions

Area I is defined as the surface surrounded by the circle with radius r_1 . Area II is defined as the surface delimited by the two circles with radius r_1 and r_2 respectively. Area III is the area outside the circle of radius r_2 . As shown in Figure V-8(a), Area I and II are bounded by the hysteresis boundaries r_1 and r_2 respectively, whereas Area III has no upper limit.

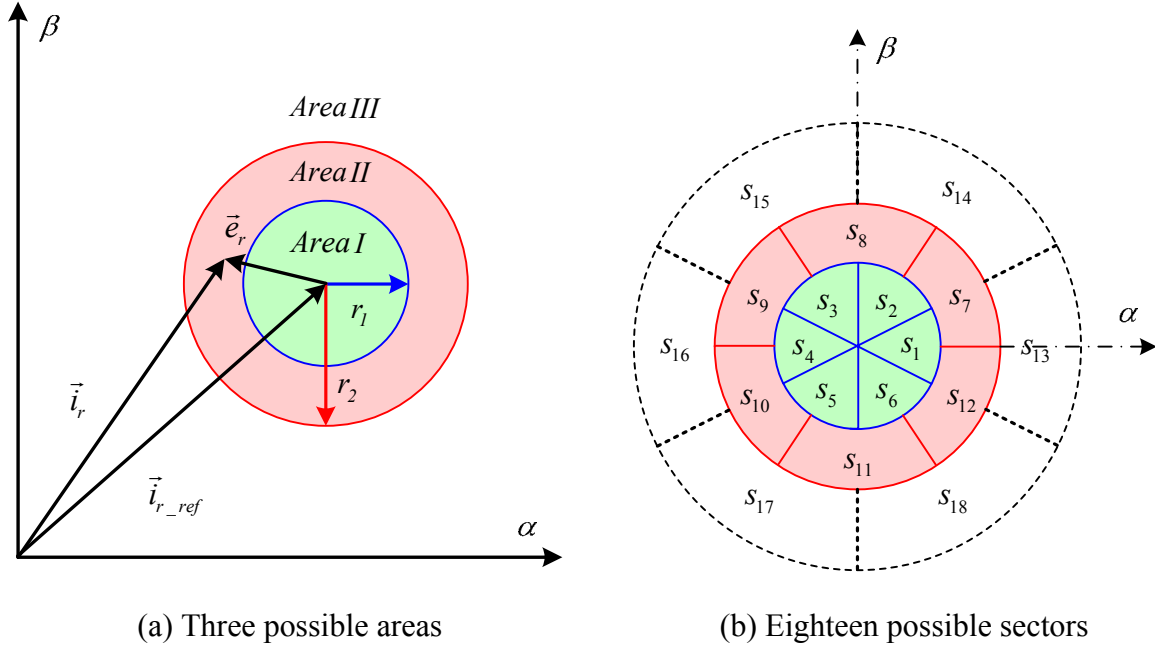


Figure V-8 : Current error vector tip location

Each one of the three areas is divided into six sectors, as shown in Figure V-8(b), which are numbered from 1 to 18. the angle between any two consecutive sectors is 60° . For instance, sector s_1 is located between -30° and 30° .

The detection of the sector, in which the tip of the current error vector is located, is made according to the following two conditions:

- the area to which the current error vector pertains,
- the angle θ between the error vector \vec{e}_r and the parallel to the α axis.

The angle θ is defined by the following expression:

$$\theta = \arctan \left(\frac{|\vec{e}_{r\beta}|}{|\vec{e}_{r\alpha}|} \right) \tag{V-99}$$

In this way, the error vector tip can be located in any of the 18 sectors depending on the value of the angle θ and the area number. Table V-2, 3, 4 give the conditions that must be satisfied for the error vector \vec{e}_r to belong to each particular sector.

Angle θ	Secteur
$-30^\circ < \theta < 30^\circ$	s_1
$30^\circ < \theta < 90^\circ$	s_2
$90^\circ < \theta < 150^\circ$	s_3
$150^\circ < \theta < 210^\circ$	s_4
$210^\circ < \theta < 270^\circ$	s_5
$270^\circ < \theta < 330^\circ$	s_6

Table IV-2 : Definition of the sectors in Area I

Angle θ	Secteur
$0^\circ < \theta < 60^\circ$	s_7
$60^\circ < \theta < 120^\circ$	s_8
$120^\circ < \theta < 180^\circ$	s_9
$180^\circ < \theta < 240^\circ$	s_{10}
$240^\circ < \theta < 320^\circ$	s_{11}
$320^\circ < \theta < 360^\circ$	s_{12}

Table IV-3 : Definition of the sectors in Area II

Angle θ	Secteur
$-30^\circ < \theta < 30^\circ$	s_{13}
$30^\circ < \theta < 90^\circ$	s_{14}
$90^\circ < \theta < 150^\circ$	s_{15}
$150^\circ < \theta < 210^\circ$	s_{16}
$210^\circ < \theta < 270^\circ$	s_{17}
$270^\circ < \theta < 330^\circ$	s_{18}

Table IV-4 : Definition of the sectors in III

As it is illustrated in Figure V-9, when the error vector tip is located in Area I, one of the small hexagon voltage vectors will be applied. In the same way, one of the medium hexagon voltage vectors will be applied if the error vector tip is located in Area II. Otherwise, one of the large hexagon voltage vectors will be applied when the error vector tip is located in Area

III.

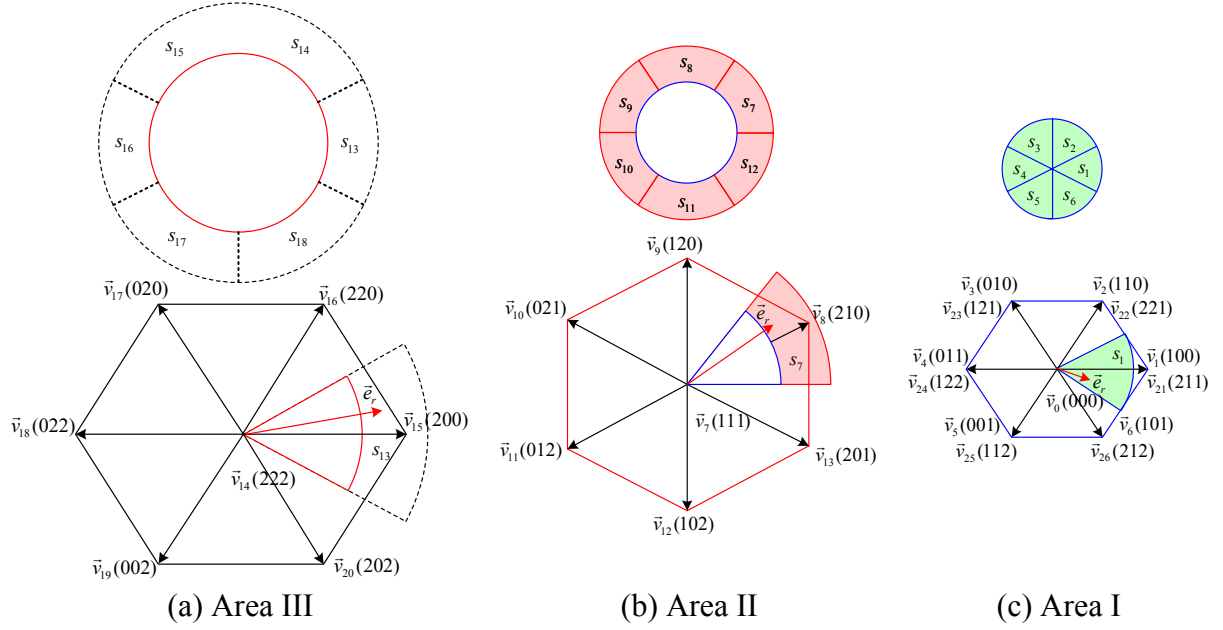


Figure IV-9 : Error vector tip location and corresponding selected voltage vector category

To understand the selection rule of the appropriate voltage vector, a sector from each area is considered (Figure V-9).

If the error vector tip is located in sector s_{13} of Area III, the best choice to get back the error towards the hysteresis Area II is \vec{v}_{18} (Figure V-9(a)). If the error vector tip is located in sector s_7 of Area II, \vec{v}_{11} is the suitable voltage vector to get back the error towards the hysteresis Area I (Figure V-9(b)). If the error vector tip is located in sector s_l of Area I, the appropriate voltage vector to move the error back towards the zero point is either \vec{v}_4 or \vec{v}_{24} (Figure V-9(c)). The choice between \vec{v}_4 and \vec{v}_{24} is made according to the sign of the NP voltage $\Delta u = u_{c1} - u_{c2}$.

In fact, the neutral point voltage unbalance appears when $\Delta u = u_{c1} - u_{c2} \neq 0$ or $i_{m2} \neq 0$. Moreover, a positive current i_{m2} produces a charge in the upper capacitor (C_1), while a negative current produces a discharge in the same capacitor. The voltage vectors of the three-phase converter are divided into three categories according to their lengths: large, medium and small, as shown in Figure V-8.

Only the small vectors have two realisations: one positive and one negative switching function [137-139]. The positive one ($\vec{v}_1, \vec{v}_2, \vec{v}_3, \vec{v}_4, \vec{v}_5, \vec{v}_6$) charges the upper capacitor C_1 , whereas the negative one ($\vec{v}_{21}, \vec{v}_{22}, \vec{v}_{23}, \vec{v}_{24}, \vec{v}_{25}, \vec{v}_{26}$) discharges it. The neutral point voltage balancing is achieved by applying the appropriate small vectors to charge or discharge the upper capacitor C_1 according to the sign of the neutral point voltage Δu .

The selection of the appropriate voltage vector must satisfy both following conditions:

- the control of the load currents with the proposed SVHCC,
- the control of the NP voltage by using the redundant inverter switching states.

After the location of the current error vector is detected and the neutral point voltage is sensed, an appropriate voltage vector should be selected and applied on the converter. When the error vector tip is located in area I, one among the small hexagon voltage vectors will be applied. By the same way, if the error vector tip is located in area II, one of the medium hexagon voltage vectors will be selected. Otherwise, one of the large hexagon voltage vectors will be applied. The selection between the three zero voltage vectors ($\vec{v}_0, \vec{v}_7, \vec{v}_{14}$) is determined by adopting the principle to switch only one inverter leg at once in order to minimise the switching frequency.

Therefore two simple look-up tables (Table V-5, 6), which uses the sector information and the neutral point voltage sign, can be obtained.

	s_1	s_2	s_3	s_4	s_5	s_6
$\Delta u > 0$	\vec{v}_{24}	\vec{v}_{25}	\vec{v}_{26}	\vec{v}_{21}	\vec{v}_{22}	\vec{v}_{23}
$\Delta u < 0$	\vec{v}_4	\vec{v}_5	\vec{v}_6	\vec{v}_1	\vec{v}_2	\vec{v}_3

Table V-5 : Switching table for the proposed SVHCC in Area I

s_7	s_8	s_9	s_{10}	s_{11}	s_{12}
\vec{v}_{11}	\vec{v}_{12}	\vec{v}_{13}	\vec{v}_8	\vec{v}_9	\vec{v}_{10}
s_{13}	s_{14}	s_{15}	s_{16}	s_{17}	s_{18}
\vec{v}_{18}	\vec{v}_{19}	\vec{v}_{20}	\vec{v}_{15}	\vec{v}_{16}	\vec{v}_{17}

Table V-6 : Switching table for the proposed SVHCC in Area II and Area III

V.2.2. Reconfiguration of the control algorithms.

In an energy conversion system, power converters are usually used to introduce some control inputs for the power conversion. The hierarchical structure of the control system can be divided into four different levels, as shown in Figure V-10 [140].

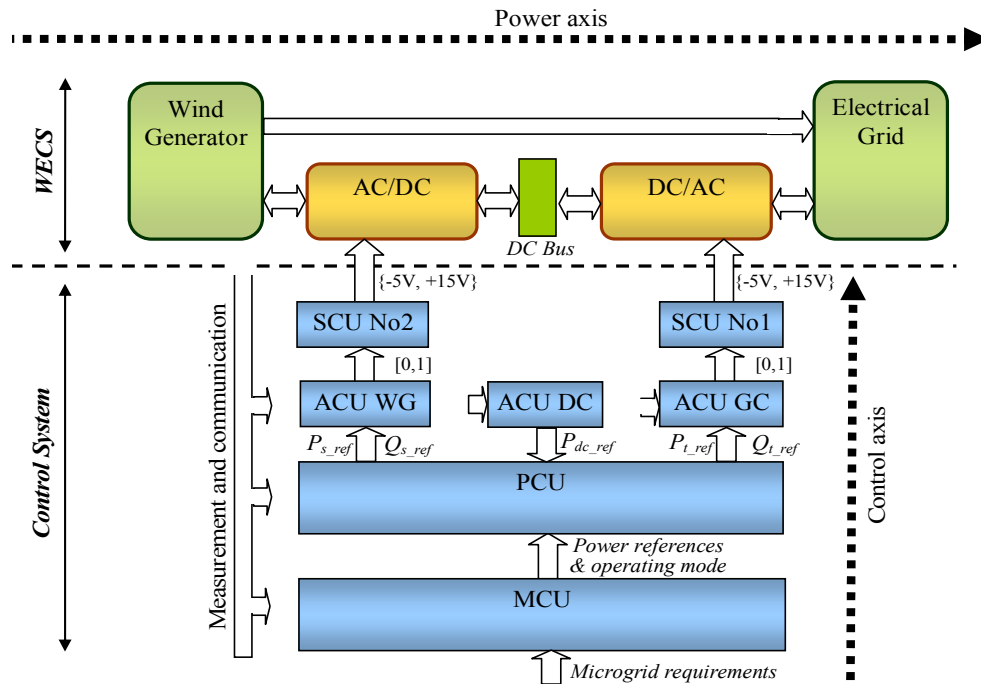


Figure V-10 : Hierarchical control structure of an wind energy conversion system

The roles of each control unit in the control system are explained as below:

The Switching Control Unit (SCU) is designed for each power converter. In a SCU, the drivers generate the transistor's ON/OFF signals from the ideal states of the switching function $\{0,1\}$ from the modulation function.

The Automatic Control Unit (ACU) is designed for each energy source and its power conversion system. In an ACU, the control algorithms calculate the modulation index of each power converter through the regulation of some physical quantities according to their reference values.

The Power Control Unit (PCU) is designed to perform the instantaneous power balancing of the system. In a PCU, some power balancing algorithms are implemented to coordinate the power mission of the generator with the power converters.

The Mode Control Unit (MCU) is designed for the energy management of the system. In a MCU, the climate condition, the generator's state and the grid condition should be supervised to make the right decision of the operating mode in order to ensure good energy availability.

In this way, the control structure of high power DFIG wind turbine system is derived in Figure V-11.

the same value as before the fault. However, if the voltage dip lasts for a long time, for example, more than 150 ms, the wind turbine is required to supply a maximum reactive current to the grid without exceeding generator limit. Thus the reactive component of the rotor current should be set to:

$$i_{rd_ref} = \sqrt{i_{r_max}^2 - \hat{i}_{rq}^2} \quad (\text{V-100})$$

Thus the reference value of the generator reactive power should be set to:

$$Q_{s_ref} = \frac{\hat{v}_s \tilde{\psi}_s}{L_s} - \frac{\hat{v}_s M}{L_s} i_{rd_ref} \quad (\text{V-101})$$

In order to implement this reconfiguration scheme, a voltage dip detection system is necessary to identify the severity and duration of the dip. The grid voltages v_a, v_b, v_c are usually transformed to voltages v_d, v_q in the synchronous reference frame by using Clark and Park transformations. As the grid voltage vector is commonly oriented along the quadrature axis, which means that v_q denotes the grid voltage level, a simple comparator can be used to detect a voltage dip as it is shown in Figure V-12. When v_q is lower than a threshold value $v_{th} = 90\%v_n$ (v_n is the nominal value), the voltage dip signal is set to be 1, else, Dip_{signal} is zero. Then an integrator is used to calculate the dip duration. If it is more than 150 ms, the reconfiguration signal will be set to be 1 in order to control the DFIG to provide the maximum reactive power.

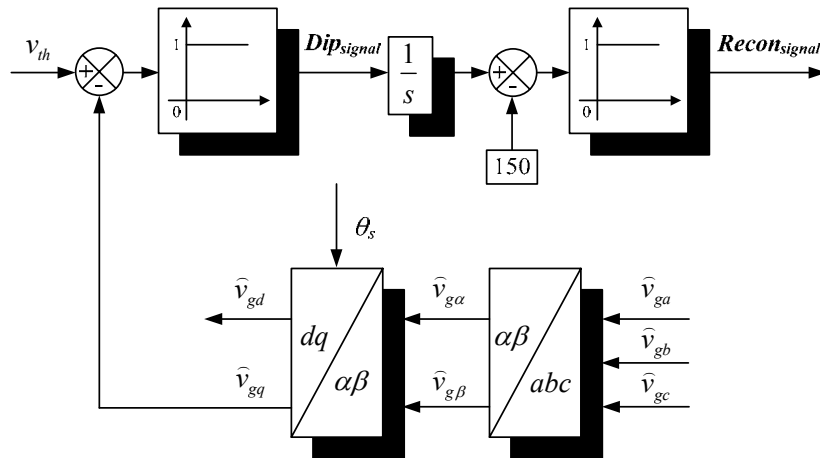


Figure V-12 : Voltage dip detection system

Moreover, the wind turbine should resume active power exportation as quickly as the technology allows and in any event within 1 second of the grid voltage recovering to the normal operating range.

V.3. SIMULATION RESULTS.

In order to study the operation performance of the system with the proposed scheme, simulation has been carried out by using Matlab Simulink™, with a 5MW DFIG. Figure V-13 shows the schematic diagram of the simulated system. The wind turbine is equipped with a step-up 0.96 kV/34.5 kV transformer and is connected to the point of common coupling (PCC, bus 3) by a 1 km cable. The PCC and the utility grid are connected through the 132 kV transmission line with a length of 30 km. And the utility grid is represented by an infinite bus.

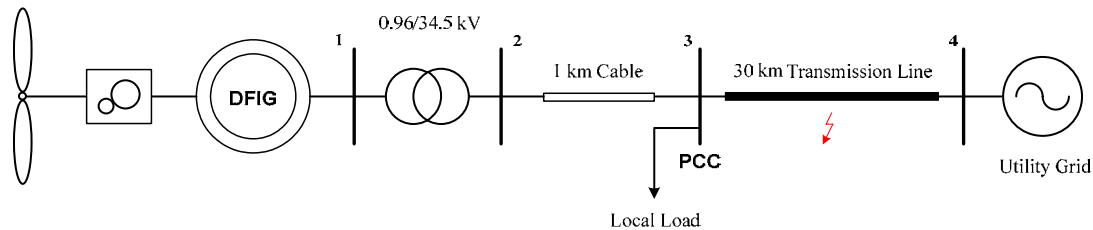


Figure V-13 : Schematic diagram of the simulated DFIG based wind turbine system

A severe three-phase short circuit grid fault is considered to happen in the middle of the transmission line. The fault lasts for 0.5 s and is subsequently cleared by restoring the initial transmission line impedance. Since the large inertia of the wind turbine results in a much larger mechanical time constant than the electrical one, the wind speed is assumed to be constant at 8 m/s throughout the duration of the event.

Figure V-14 shows the simulated results. The grid fault occurs at 3s, which causes a voltage dip of almost 60% at the PCC. And it is removed at 3.5s. Figure IV-14 (a) and (b) shows a comparison of the system responses without and with the proposed reconfiguration scheme. Although the system can ride-through the fault without reconfiguration (as the rotor currents remain in a safe range during the fault), the voltage at the PCC also remains at a lower level of about 40% rated value. In contrast, the reconfiguration method controls the generator to supply a maximum reactive current after 3.15 s, which effectively raises the voltage at PCC to about 50% of the nominal value. Thus the ancillary reactive power can help the grid voltage recovery during the fault. However, this voltage control ability is limited by the relatively small rating of the power converter. From Figure IV-14, the generator can provide adequate active power in proportion to the retained voltage during the dip, and it resumes normal operation shortly after the clearance of the fault.

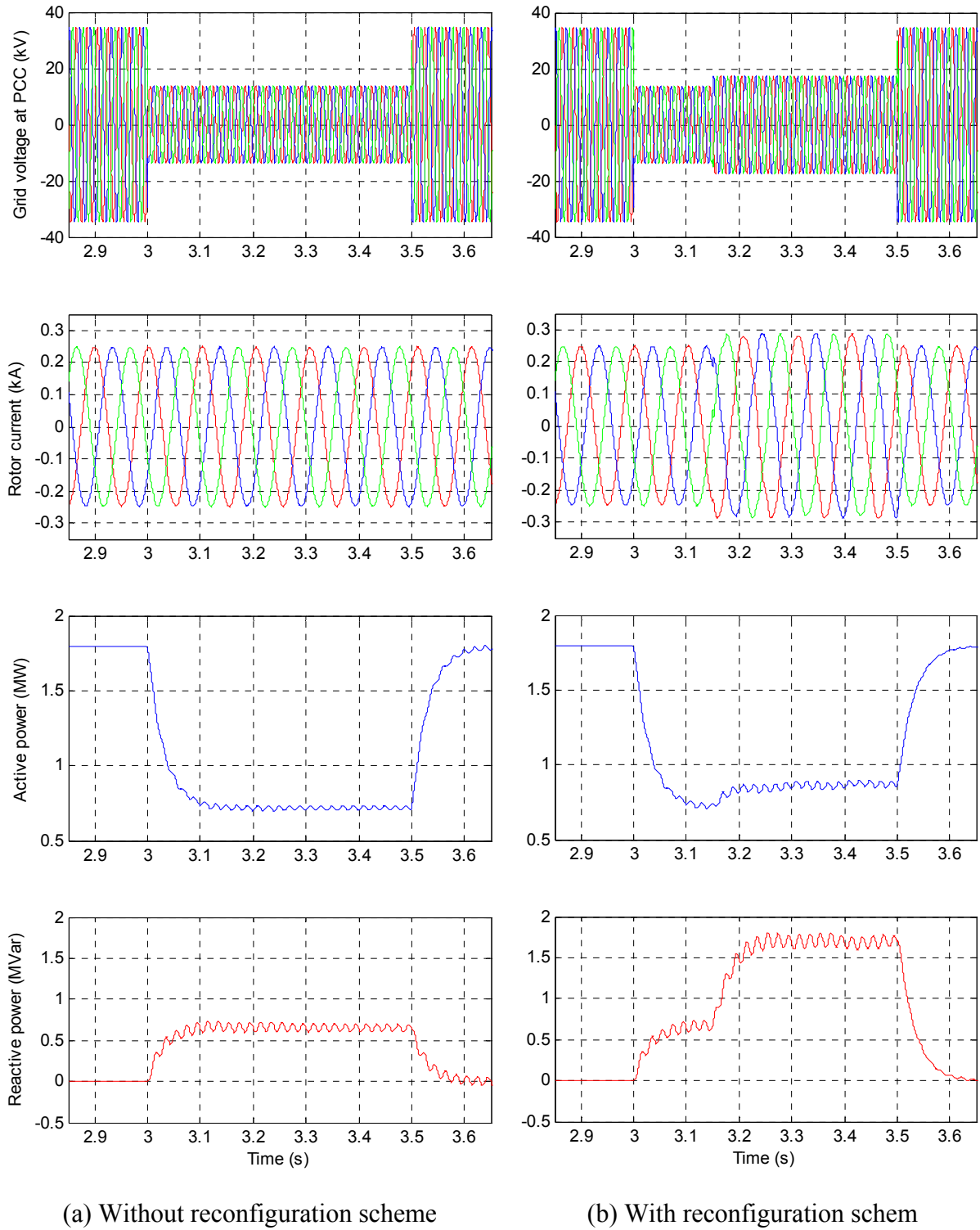


Figure V-14 : Simulation results in the case of grid fault

V.4. EXPERIMENTAL RESULTS

Based on security considerations, a 4.5kW DFIG laboratory test platform has been built up to validate the proposed control scheme. The DFIG is driven by a permanent magnet

synchronous motor (PMSG) which simulates the wind turbine. The PMSG is controlled by a variable speed driver that provides speed regulation. The rotor circuit of the DFIG is feeding by a three-level converter. The control system is implemented on the DSpace DS1104 DSP board. The experimental platform is shown in Figure V-15. A three-phase voltage dip with a 50% depth and 500 ms duration at the grid side will be considered while the rotor speed of the DFIG is set at around 1200 r/min.

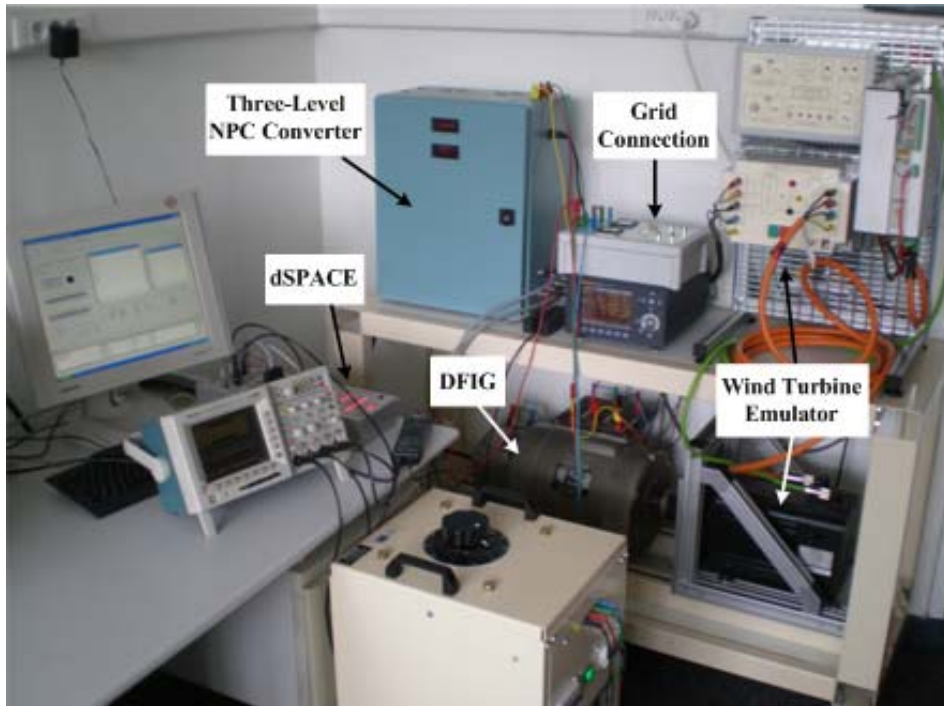


Figure V-15 : Experiment platform of the high power DFIG wind turbine system

The experimental results are presented in Figure IV-16 and prove excellent performance of the system as well as good consistency with the simulated results. With a control strategy reconfiguration, the stator voltage can be increased to about 85% of the rated value while it decreases to 70% without reconfiguration. Therefore, the fault ride-through capability of the studied DFIG system can be effectively enhanced by using the proposed scheme.

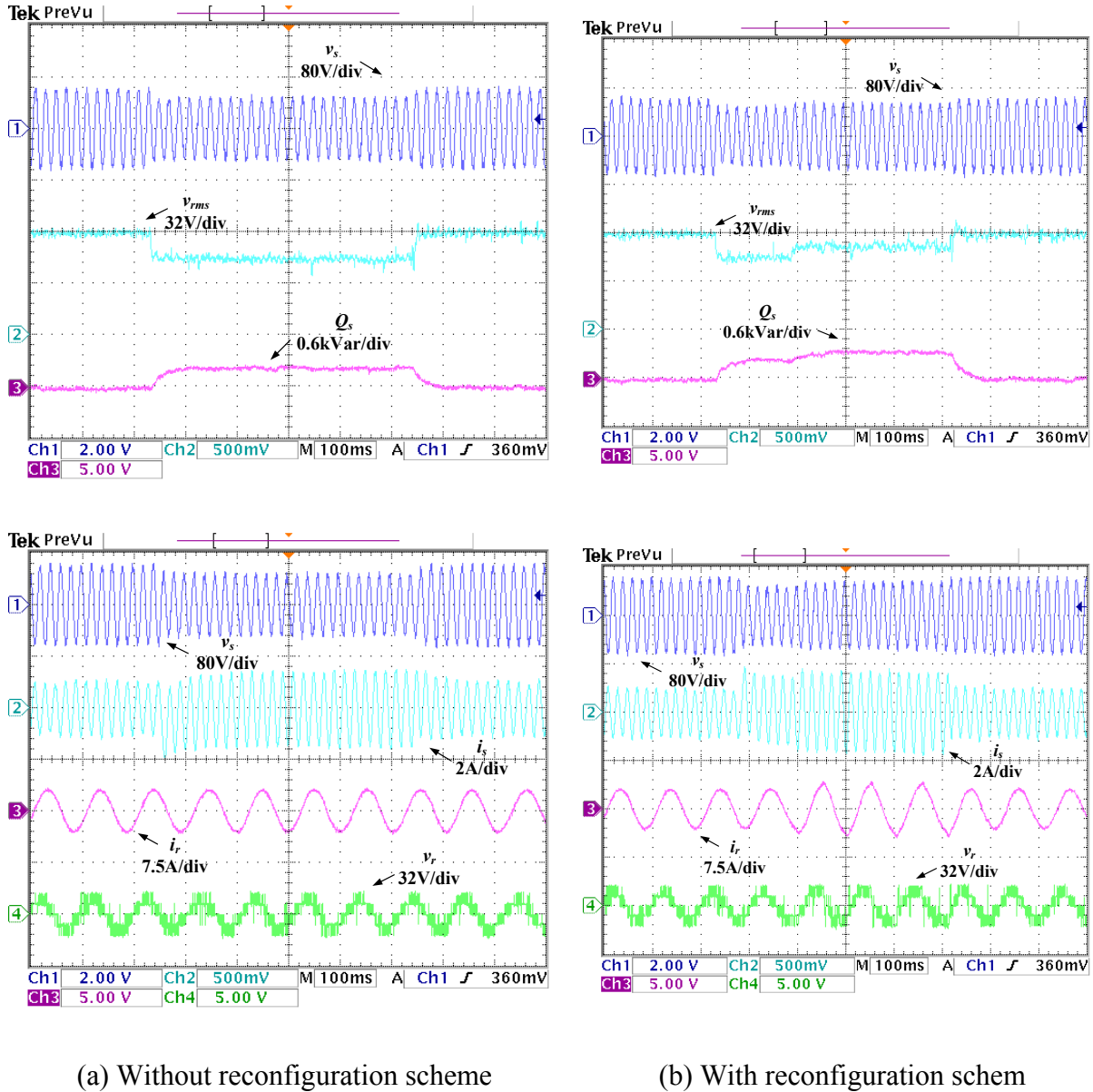


Figure V-16 : Experimental results during grid voltage dip

V.5. CONCLUSION.

A Space-Vector Hysteresis Current Controller is proposed to control the rotor-side NPC converter of a high power DFIG based wind turbine system. With the proposed strategy, the three-phase current errors can be gathered into a single space vector quantity. Hence the magnitude of the current error vector can be limited within a boundary area of a circle shape. In this way, the rotor current can be controlled in a safe range during grid voltage dips. Therefore, the LVRT capability of the DFIG system can be greatly enhanced. Moreover, a reconfiguration scheme of control strategies for the system is proposed to meet the latest grid code requirements. Both simulation and small-scale experimental tests show that with this

specific methodology, the system can stay connected to the grid in the case of grid faults. And the fault ride-through capability of the DFIG system can be greatly enhanced by providing ancillary reactive power under long duration voltage dips, which can increase the voltage at PCC during the fault. And the system can resume normal operation immediately after the clearance of the fault.

CHAPTER VI

CONCLUSION AND PERSPECTIVES

VI.1. CONCLUSION.

The presented work in this thesis is mainly about the control strategies and the protection scheme for the DFIG based wind turbine system in order to keep connected to the network during grid faults, which cause voltage dips at the generator terminal.

Firstly the studied wind turbine system has been modeled by using the graphical representation method Causal Ordering Graph (COG) and Energetic Macroscopic Representation (EMR). Then the Maximum Control Structure (MCS) has been deduced from EMR by using inversion rules. The conventional vector control strategies have been presented with COG to show the excellent performance of the system during normal grid condition. The decoupled control of the active and reactive power (thus the power factor) can be easily obtained to improve the power quality. And the DFIG can operate in VSCF mode in order to realize Maximum Power Point Tracking (MPPT).

A modified vector control strategy of the DFIG, which takes the dynamics of the stator flux into account, has been proposed to provide adequate control of the DFIG during small voltage dips. The over current in the rotor windings and over voltage in the DC bus can be well limited thanks to the proposed control strategy, which can improve the Low Voltage Ride-through (LVRT) capability of the DFIG based wind turbine system. However, its capability is limited by the relatively small rating of the power converters compared to the DFIG.

Therefore, an ancillary circuit of active crowbar has been implemented to protect the system when the voltage dip is too large. In order to reduce the activated time of the crowbar as much as possible, an improved hysteresis control strategy has been proposed. Moreover, a demagnetization method, based on a closed-loop control of the stator flux, has also been proposed to decrease the oscillations of the transient current both during the voltage dips and after the clearance of the faults. So that the DFIG can provide reactive power to the weak grid during voltage dips. In the meantime, the grid-side converter is also controlled to supply extra reactive power in order to enhance the grid voltage support capability of the total system.

Three-level converters are adopted to increase the power of wind turbines based on DFIG. A Space-Vector Hysteresis Current Controller has been proposed to control the rotor-side NPC converter. With the proposed strategy, the magnitude of the current error vector can be limited within a boundary area of a circle shape. In this way, the rotor current can be controlled in a safe range during grid voltage dips. Moreover, a reconfiguration scheme of control strategies for the system has been proposed to meet the latest grid code requirements. With this specific methodology, the system can stay connected to the grid in the case of grid faults. In addition, the fault ride-through capability of the DFIG system can be greatly enhanced by providing ancillary reactive power under long duration voltage dips, which can increase the voltage at PCC during the fault and thus provide support to the grid. And the system can resume normal operation immediately after the clearance of the fault. Thus the system can meet the requirements by the grid code.

VI.2. PERSPECTIVE.

The ride-through capability has been enhanced against symmetrical three-phase network fault. This kind of fault, however, is very seldom. Single and two-phase earth faults and two-phase faults are more common. Except of the dc component, the negative sequence component will be also produced in the stator flux because of the asymmetrical faults. Due to the large slip of the negative sequence, very large transients will appear, which makes it more difficult to control the DFIG during an asymmetrical voltage dip. Thus, research about unsymmetrical fault ride-through performance is required to improve the maintenance of production in more general situations.

REFERENCE

- [1] C. Millais, S. Teske. Wind force 12: a blueprint to achieve 12% of the world's electricity from wind power by 2020. Greenpeace European Wind Energy Association, 2004.
- [2] World Wind Energy Association. World wind energy report 2008. 2009.
- [3] Z. Chen, F. Blaabjerg. Wind energy - the world's fastest growing energy source. IEEE Power Electron. Soc. Newsl., 2006, 18, (3):15-19.
- [4] R. Thresher, M. Robinson, P. Veers. To Capture the Wind: The Status and Future of Wind Energy Technology. IEEE power & energy magazine, November/December 2007:34-46.
- [5] R. Datta, V. Ranganathan. Variable-Speed Wind Power Generation Using a Doubly Fed Wound Rotor Induction Machine: A Comparison with Alternative Schemes. IEEE Transaction on Energy Conversion, 2002, 17(3):414-421.
- [6] F. Blaabjerg, Z. Chen, S. Kjaer. Power electronics as efficient interface in dispersed power generation systems. IEEE Transaction on Power Electronics, 2004, 19(5):1184-1194.
- [7] J. Carrasco, L. Franquelo, J. Bialasiewicz, et al. Power-Electronic Systems for the Grid Integration of Renewable Energy Sources: A Survey. IEEE Transaction on Industrial Electronics, 2006, 53(4):1002-1016.
- [8] L. Hansan, L. Helle, F. Blaabjerg, et al. Conceptual survey of generators and power electronics for wind turbines. Riso National Laboratory Technical Report Riso-R-1205(EN) Roskilde, Denmark, December 2001.
- [9] H. Polinder, J. Morren. Developments in wind turbine generator systems. Electrimacs 2005, Hammamet, Tunisia.
- [10] A. Hansan, L. Hansan. Wind turbine concept market penetration over 10 years (1995–2004). Wind Energy, 2007, 10, (1):81-97.
- [11] S. Muller, M. Deicke, R. De Doncker. Doubly fed induction generator systems for wind turbines. IEEE Industry Applications Magazine, 2002, 8(3):26-33.
- [12] H. Li, Z. Chen. Overview of different wind generator systems and their comparisons. IET Renewable Power Generation, 2008, 2(2):123-138.
- [13] H. Polinder, F. van der Pijl, G. de Vilder, et al. Comparison of direct-drive and geared generator concepts for wind turbines. IEEE Transaction on Energy Conversion, 2006, 21(3): 725-733.
- [14] Y. Chen, P. Pillay, A. Khan. PM wind generator topologies. IEEE Transaction on Industrial Applications, 2005, 41, (6):1619-1626.
- [15] M. Dubois, H. Polinder, J. Ferreira. Comparison of generator topologies for direct-drive wind turbines. Proceeding of Nordic Countries Power and Industrial Electronics Conferece, Aalborg, Denmark, June 2000:22-26.
- [16] J. Baroudi, V. Dinavahi, A. Knight. A review of power converter topologies for wind generators. Renewable Energy 2007, 32:2369-2385.
- [17] F. Blaabjerg, R. Teodorescu, M. Liserre, et al. Overview of Control and Grid Synchronization for Distributed Power Generation Systems. IEEE Transaction on Industrial Electronics, 2006, 53(5):1398-1409.
- [18] R. Pena, J. Clare, G. Asher. Double fed induction generator using back-to-back PWM converter and its application to variable-speed wind-energy generation. Proc. IEE Electr. Power Appl., vol. 143, no. 3, pp. 231–241, May 1996.
- [19] O. Dorin, P. Neacsu. Analysis and Design of IGBT-based AC/AC Direct Converters Built of Conventional Current Source Inverter Modules.
- [20] Keyuan H, Yikang H. Investigation of a matrix converter-excited brushless doubly-fed machine

wind-power generation system. Proceedings IEEE PEDS'03, 2003, 1: 743–748.

- [21] A. Trzynadlowski, N. Patriciu, F. Blaabjerg, et al. A Hybrid, Current-Source/Voltage-Source Power Inverter Circuit.
- [22] Petersson A, Harnefors L, Thiringer T. Comparison between stator-flux and grid-flux-oriented rotor current control of doubly-fed induction generators. PESC 04, 2004, 1: 482-486.
- [23] H. Akagi, H. Sato. Control and performance of a doubly-fed induction machine intended for a flywheel energy storage system. IEEE Trans. Power Electron., vol. 17, no. 1, pp. 109–116, Jan. 2002.
- [24] M.Yamanmoto, O.Motoyoshi, Active and Reactive Power Control of Doubly-Fed Wound Rotor Induction Generator. IEEE Trans. on Power Electronics, 1991,6(4):624-629.
- [25] M. Depenbrock. Direct self-control (DSC) of inverter-fed induction machine. IEEE Trans. Power Electron., vol. 3, no. 4, pp. 420–429, Oct.1988.
- [26] Rajib Datta, V. T. Ranganathan. Direct Power Control of Grid-Connected Wound Rotor Induction Machine Without Rotor Position Sensors. IEEE Trans. on Power Electronics,2001,16(3):390-399.
- [27] L. Xu, P. Cartwright. Direct active and reactive power control of DFIG for wind energy generation. IEEE Trans. Energy Convers., vol. 21, no. 3, pp. 750–758, Sep. 2006.
- [28] O. Anaya-Lara, F.M. Hughes, N. Jenkins, G. Strbac, Rotor Flux Magnitude and Angle Control Strategy for Doubly Fed Induction Generators. Wind Energy, vol.9, pp. 479–495, 2006
- [29] R.G. de Almeida, J.A.P. Lopes, et al. Improving power system dynamic behavior through doubly fed induction machines controlled by static converter using fuzzy control. IEEE Transactions on Power Systems, vol. 19, no. 4, pp. 1942 – 1950, November 2004.
- [30] N.P. Quang, A. Dittrich, P.N. Lan. Doubly-fed induction machine as generator in wind power plant nonlinear control algorithms with direct decoupling. Proceedings of EPE 2003, Dresden, Germany, September 2005.
- [31] M.R. Rathi, N. Mohan. A novel robust low voltage and fault ride through for wind turbine application operating in weak grids. 31st Annual Conference of IEEE Industrial Electronics Society (IECON 2005), November 2005.
- [39] J. Morren, S.W.H. de Haan, Ridethrough of wind turbines with doubly-fed induction generator during a voltage dip, IEEE Transaction on Energy Conversion, vol. 20, no. 2, pp. 435 – 441, June 2005.
- [40] J. Lopez, P. Sanchis, X. Roboam, L. Marroyo, Dynamic Behavior of the Doubly Fed Induction Generator During Three-Phase Voltage Dips, IEEE Transaction on Energy Conversion, vol. 22, no. 3, pp. 709 – 717, Sept. 2007.
- [41] S.Seman, J. Niiranen, S. Kanerva, A. Arkkio, J. Saitz, Performance Study of a Doubly Fed Wind-Power Induction Generator Under Network Disturbances. IEEE Transaction on Energy Conversion, vol. 21, no. 4, pp. 883 – 890, December 2006.
- [42] J.B. Ekanayake, L. Holdsworth, XueGuang Wu; N. Jenkins, Dynamic modeling of doubly fed induction generator wind turbines, IEEE Transactions on Power Systems, vol. 18, no. 2, pp. 803 – 809, May 2003.
- [43] A. Petersson, S. Lundberg, T. Thiringer, A DFIG Wind Turbine Ride-through System. Influence on the Energy Production, Wind Energy, vol. 8, pp. 251–263, 2005.
- [44] I. Erlich, J. Kretschmann, J. Fortmann, S. Mueller-Engelhardt, H. Wrede, Modeling of Wind Turbines Based on Doubly-Fed Induction Generators for Power System Stability Studies, IEEE Transactions on Power Systems, vol. 22, no. 3, pp. 909 – 919, August 2007.
- [45] E. Muljadi, C.P. Butterfield, B. Parsons, A. Ellis, Effect of Variable Speed Wind Turbine Generator on Stability of a Weak Grid, IEEE Transaction on Energy Conversion, vol. 22, no. 1, pp. 29 – 36, March 2007.
- [46] P.S. Flannery, G. Venkataramanan, A Fault Tolerant Doubly Fed Induction Generator Wind Turbine Using a Parallel Grid Side Rectifier and Series Grid Side Converter, IEEE Transactions on Power Electronics, vol. 23, no. 3, pp. 1126 – 1135, May 2008.

- [47] A.D. Hansen, G. Michalke, Fault ride-through capability of DFIG wind turbines, *Renewable Energy*, vol 32, 2007, pp 1594-1610.
- [48] A.D. Hansen, G. Michalke, P. Sørensen, T. Lund, F. Iov, Coordinated voltage control of DFIG wind turbines in uninterrupted operation during grid faults, *Wind Energy*, No. 10, 2007, pp. 51-68.
- [49] Xiang Dawei, Li Ran. Control of a doubly fed induction generator in a wind turbine during grid fault ride-through[J]. *IEEE Transaction on Energy Conversion*, 2006, 21(3): 652-662.
- [50] He Yikang, Hu Jiabing, Zhao Rende, Modeling and Control of Wind-Turbine Used DFIG under Network Fault Conditions, *Proceedings of the Eighth International Conference on Electrical Machines and Systems*, Nanjing, China, September, 2005, vol. 2, pp. 986-991
- [51] J.B. Ekanayake, L. Holdsworth, N. Jenkins, Comparison of 5th order and 3rd order machine models for doubly fed induction generator (DFIG) wind turbines, *Electric Power Systems Research*, vol. 67, no. 3, pp. 207-215, December 2003.
- [52] Gomis-Bellmunt O, Junyent-Ferre A, Sumper A, et al. Ride-Through control of a doubly fed induction generator under unbalanced voltage sags. *IEEE Transaction on Energy Conversion*, 2008, 23(4):1036-1045.
- [53] Brekken T, Mohan N. Control of a doubly fed induction wind generator under unbalanced grid voltage conditions. *IEEE Transaction on Energy Conversion*, 2007, 22(1):129-135.
- [54] Zhou Y, Bauer P, Ferreira J, et al. Operation of grid-connected DFIG under unbalanced grid voltage condition. *IEEE Transaction on Energy Conversion*, 2009, 24(1):240-246.
- [55] Qiao W, Harley R. Improved control of DFIG wind turbines for operation with unbalanced network voltages. *IAS '08*, 2008.
- [56] Xu L. Enhanced control and operation of DFIG-based wind farms during network unbalance. *IEEE Transactions on Energy Conversion*, 2008, 23(4):1073-1081.
- [57] Santos-Martin D, Rodriguez-Amenedo J, Arnalte S. Direct power control applied to doubly fed induction generator under unbalanced grid voltage Conditions. *IEEE Transaction on Power Electronics*, 2008, 23(5):2328-2336.
- [58] Hu J, He Y, Xu L, et al. Improved control of DFIG systems during network unbalance using PI-R current regulators. *IEEE Transactions on Industrial Electronics*, 2009, 56(2):439-451.
- [59] J.K. Niiranen, Simulation of Doubly Fed Induction Generator wind turbine with an active crowbar, *EPE-PEMC 2004*, Riga, Latvia, September 2004.
- [60] J. Niiranen, Voltage dip ride through of a doubly-fed generator equipped with an active Crowbar, *Nordic Wind Power Conference*, Sweden, 2004.
- [61] Bing Xie, B. Fox, D. Flynn, Study of fault ride-through for DFIG based wind turbines, *Proceedings of the 2004 IEEE International Conference on Electric Utility Deregulation, Restructuring and Power Technologies*, vol. 1, April 2004:411 – 416.
- [62] T. Sun, Z. Chen, F. Blaabjerg, Voltage recovery of grid-connected wind turbines with DFIG after a short-circuit fault, *PESC 04*, vol. 3, June 2004:1991 – 1997.
- [63] M. Rodriguez, G. Abad, I. Sarasola, A. Gilabert, Crowbar control algorithms for doubly fed induction generator during voltage dips, *Proceedings of EPE 2005*, Dresden, Germany, September, 2005
- [64] C. Abbey, G. Joos, Supercapacitor Energy Storage for Wind Energy Applications, *IEEE Transactions on Industry Applications*, vol. 43, no. 3, pp. 769 – 776, May-June 2007.
- [65] P. La Seta, P. Schegner, Comparison of stabilizing methods for doubly-fed induction generators for wind turbines, *2005 International Conference on Future Power Systems*, November 2005.
- [66] A. Dittrich, A. Stoev, Comparison of fault ride-through strategies for wind turbines with DFIM generators, *Proceedings of EPE 2005*, Dresden, Germany, September, 2005.
- [67] Hautier JP, Barre P. The Causal Ordering Graph, A tool for system modelling and control law synthesis. *Studies in informatics and control*, 2003, 13(4): 265-283.

- [68] Guillaud X, Barre P, Hautier J. Modeling, control and causality: the Causal Ordering Graph. 16th IMACS world congress, 2000.
- [69] Guillaud X, Barre P, Hautier J. Synthesis of control law with the method of Causal Ordering Graph. ICEM, 2000, vol. 4: 1917-1921.
- [70] Barre P, Bouscayrol A, Delarue, P, et al. Inversion-based control of electromechanical systems using causal graphical descriptions. IECON 2006, 2006: 5276-5281.
- [71] Bouscayrol A, Davat B, de Fornel B, et al. Multimachine Multiconverter System: application for electromechanical drives. European Physics Journal – Applied Physics, 2000, 10(2): 131-147.
- [72] Bouscayrol A, Guillaud X, Delarue P, et al. Energetic Macroscopic Representation and inversion-based control illustrated on a Wind Energy Conversion System using Hardware-in-the-Loop simulation. IEEE Transactions on Industrial Electronics, 2009, 56(12): 4826-4835.
- [73] Delarue P, Bouscayrol A, Tounzi X, et al. Modeling, control and simulation of an overall wind energy conversion system. Renewable Energy, 2003, 28(8): 1169-1184.
- [74] Burton T, Sharpe D, Jenkins N, et al. Wind energy handbook. New York: John Wiley & Sons, 2001.
- [75] Abdin E, Xu W. Control design and dynamic performance analysis of a wind turbine induction generator unit. IEEE Transactions on Energy Conversion, 2000, 15(1): 91-96.
- [76] Ekanayake J, Holdsworth L, Jenkins N. Comparison of 5th order and 3rd order machine models for doubly fed induction generator (DFIG) wind turbines. Electric Power Systems Research, 2005, 67(3):207-215.
- [77] Jabr H, Kar C. Effects of main and leakage flux saturation on the transient performances of doubly-fed wind driven induction generator. Electric Power Systems Research, 2007, 77(8):1019-1027.
- [78] Francois B, Cambronne J, Hautier J. A new approach for synthesizing logic connection controllers in power converters. EPE'95, September 1995, Sevilla.
- [79] S. El Aimani. Modélisation de différentes technologies d'éoliennes intégrées dans un réseau de moyenne tension. Thèse soutenu en 2004 de l'Ecole Centrale de Lille.
- [80] Bearee R, Barre P, Hautier J. Control structure synthesis for electromechanical systems based on the concept of inverse model using Causal Ordering Graph. IECON 2006, 2006: 5289-5294.
- [81] Bouscayrol A, Delarue P, Guillaud X. Power strategies for Maximum Control Structure of a wind energy conversion system with a synchronous machine. Renewable Energy, 2005, 28: 2273-2288.
- [82] Bouscayrol A, Delarue P. Simplifications of the Maximum Control Structure of a wind conversion system with an induction generator. International Journal of Renewable Energy Engineering, 2002, 4(2): 479-485.
- [83] Pena R, Clare J, Asher G. Doubly fed induction generator using back-to-back PWM converters and its application to variable-speed wind-energy generation. IEE Proceedings Electric Power Applications, 1996, 13(3):231-241.
- [84] Muller S, Deicke M, Doncker R. Doubly fed induction generator systems for wind turbines. IEEE Industry Applications Magazine, 2002, 8(3):26-33.
- [85] Petersson A, Harnefors L, Thiringer T. Comparison between stator-flux and grid-flux-oriented rotor current control of doubly-fed induction generators. PESC 04, 2004, 1: 482-486.
- [86] Chondrogiannis S, Barnes M. Stability of doubly-fed induction generator under stator voltage orientated vector control. IET Renewable Power Generation, 2008, 2(3):170-180.
- [87] Yao J, Li H, Liao Y, et al. An improved control strategy of limiting the DC-link voltage fluctuation for a doubly fed induction wind generator. IEEE Transaction on Power Electronics, 2008, 23(3):1205-1213.
- [88] Iov F, Hansen A, Sorensen P, et al. Mapping of grid faults and grid codes. RISØ Report, 2007.
- [89] Holdsworth L, Wu X, Ekanayake J, et al. Comparison of fixed speed and doubly-fed induction wind turbines during power system disturbances. IEE Proceedings Generation, Transmission and Distribution,

2003, 150(3):342-352.

- [90] Vicatos M, Tegopoulos J. Transient state analysis of a doubly fed induction generator under three phase short circuit, *IEEE Transaction on Energy Conversion*, 1991, 6(1):62-68.
- [91] Seman S, Niiranen J, Kanerva S, et al. Performance study of a Doubly Fed Wind-Power Induction Generator under network disturbances. *IEEE Transaction on Energy Conversion*, 2006, 21(4):883-890.
- [92] Sun T, Chen Z, Blaabjerg F. Transient analysis of grid-connected wind turbines with DFIG after an external short-circuit fault. *Nordic Wind Power Conference*, 2004.
- [93] El-Sattar A, Saad N, Shams El-Dein M. Dynamic response of doubly fed induction generator variable speed wind turbine under fault. *Electric Power Systems Research*, 2008, 78:1240-1246.
- [94] Perdana A, Carlson O, Persson J. Dynamic response of grid-connected wind turbine with doubly fed induction generator during disturbances. *Nordic Workshop on Power and Industrial Electronics*, 2004.
- [95] Petersson A, Harnefors L, Thiringer T. Evaluation of current control methods for wind turbines using doubly-fed induction machines. *IEEE Transactions on Power Electronics*, 2005, 20(1):227-235.
- [96] Gomis-Bellmunt O, Junyent-Ferre A, Sumper A, et al. Ride-Through control of a doubly fed induction generator under unbalanced voltage sags. *IEEE Transaction on Energy Conversion*, 2008, 23(4):1036-1045.
- [97] Ekanayake J, Holdsworth L, Wu X, et al. Dynamic modeling of doubly fed induction generator wind turbines. *IEEE Transactions on Power Systems*, 2003, 18(2):803-809.
- [98] Xiang D, Ran L, Tavner P, et al. Control of a doubly fed induction generator in a wind turbine during grid fault ride-through. *IEEE Transactions on Energy Conversion*, 2006, 21(3):652-662.
- [99] He Y, Hu J, Zhao R. Modeling and control of wind-turbine used DFIG under network fault conditions. *International Conference on Electrical Machines and Systems*, 2005, 2:986-991.
- [100] Seman S, Niiranen J, Arkkio A. Ride-Through Analysis of Doubly Fed Induction Wind-Power Generator Under Unsymmetrical Network Disturbance. *IEEE Transaction on Power Systems*, 2006, 21(4):1782-1789.
- [101] Anaya-Lara O, Hughes F, Jenkins N, et al. Rotor flux magnitude and angle control strategy for doubly fed induction generators. *Wind Energy*, 2006, 9:479-495.
- [102] Almeida R, Lopes J, Barreiros J. Improving power system dynamic behavior through doubly fed induction machines controlled by static converter using fuzzy control. *IEEE Transactions on Power Systems*, 2004, 19(4):1942-1950.
- [103] Rathi M, Mohan N. A novel robust low voltage and fault ride through for wind turbine application operating in weak grids. *IECON 2005*, 2005.
- [104] Quang N, Dittrich A, Lan P. Doubly-fed induction machine as generator in wind power plant nonlinear control algorithms with direct decoupling. *EPE'05*, 2005.
- [105] IEEE recommended practices and requirements for harmonic control in electrical power system. *IEEE Standard*:519-1992.
- [106] Bollen M, Styvaktakis S. Characterization of three-phase unbalanced sags, as easy as one, two, three. *IEEE PES Summer Meeting*, 2000.
- [107] Bollen M. Characterization of voltage sags experienced by three phase adjustable-speed drives. *IEEE Transactions on Power Delivery*, 1997, 12: 1666- 1671.
- [108] Bollen M, Graaff R. Behavior of AC and DC drives during voltage sags with phase-angle jump and three-phase unbalance. *IEEE Power Engineering Society Winter Meeting*, 1999.
- [109] Bollen M, Olguin G, Martins M. Voltage dips at the terminals of wind power installations. *Wind Energy*, 2005, 8:307-318.
- [110] Lopez J, Sanchis P, Roboam X, et al. Dynamic behavior of the Doubly Fed Induction Generator during three-phase voltage dips. *IEEE Transaction on Energy Conversion*, 2007, 22(3):709-717.
- [111] Niiranen J. Simulation of doubly fed induction generator wind turbine with an active crowbar.

EPE-PEMC 2004, 2004.

- [112]Niiranen J. Voltage dip ride through of a doubly-fed generator equipped with an active Crowbar. Nordic Wind Power Conference, 2004.
- [113]Morren J, Haan S. Ridethrough of wind turbines with doubly-fed induction generator during a voltage dip. IEEE Transaction on Energy Conversion, 2005, 20(2):435-441.
- [114]Erlich I, Kretschmann J, Fortmann J, et al. Modeling of wind turbines based on doubly-fed induction generators for power system stability studies. IEEE Transactions on Power Systems, 2007, 22(3):909-919.
- [115]Abbey C, Joos G. Supercapacitor energy storage for wind energy applications. IEEE Transactions on Industry Applications, 2007, 43(3):769-776.
- [116]Pettersson A, Lundberg S, Thiringer T. A DFIG wind turbine ride-through system influence on the energy production. Wind Energy, 2005, 8:251-263.
- [117]Flannery P, Venkataramanan G. A fault tolerant doubly fed induction generator wind turbine using a parallel grid side rectifier and series grid side converter. IEEE Transactions on Power Electronics, 2008, 23(3):1126-1135.
- [118]Hansen A, Michalke G. Fault ride-through capability of DFIG wind turbines. Renewable Energy, 2007, 32:1594-1610.
- [119]Hansen A, Michalke G, Sorensen P, et al. Coordinated voltage control of DFIG wind turbines in uninterrupted operation during grid faults. Wind Energy, 2007, 10:51-68.
- [120]Seman S, Niiranen J, etc. Ride-Through Analysis of Doubly Fed Induction Wind-Power Generator Under Unsymmetrical Network Disturbance. IEEE Transactions on Power Systems, 2006, 21(4):1782-1789.
- [121]Tsourakis G, Vournas C. Simulation of low voltage ride through capability of wind turbines with Doubly fed induction generator. EWEC 2006, Athens, Greece.
- [122]Rodriquez M, Abad G, etc. Crowbar control algorithms for doubly fed induction generator during voltage dips. EPE 2005, Dresden, Germany.
- [123]Dittrich A, Stoev A. Comparison of fault ride-through strategies for wind turbines with DFIM generators. EPE 2005, Dresden, Germany.
- [124]Lohde R, Jensen S, Knop A, et al. Analysis of three phase grid failure on doubly fed induction generator ride-through using Crowbars. EPE 2007, Aalborg, Denmark.
- [125]Blaabjerg F, Chen Z, Kjaer S. Power electronics as efficient interface in dispersed power generation systems. IEEE Transactions on Power Electronics, 2004, 19(5):1184-1194.
- [126]Carrasco J, Franquelo L, Bialasiewicz J, et al. Power-electronic systems for the grid integration of renewable energy sources: a survey. IEEE Transaction on Industrial Electronics, 2006, 53(4):1002-1016.
- [127]Lai J, Peng F. Multilevel converters-a new breed of power converters. IEEE Transactions on Industry Application, 1996, 32(3):509-517.
- [128]Rodriguez J, Lai J, Peng F. Multilevel inverters: a survey of topologies, controls, and applications. IEEE Transactions on Industry Application, 2002, 49(4):724-736.
- [129]Portillo R, Prats M, Leon J, et al. Modeling strategy for back-to-back three-level converters applied to high-power wind turbines. IEEE Transactions on Industrial Electronics, 2006, 53(5):1483-1491.
- [130]Malinowski M, Stynski S, Kolomyjski W, et al. Control of three-level PWM converter applied to variable-speed-type turbines. IEEE Transactions on Industrial Electronics, 2009, 56(1): 69-77.
- [131]Francois B, Semail E. Modeling and control of a three-phase neutral point clamped inverter by means of a direct space vector control of line to line voltages. EPE-PEMC 2002, 2002.
- [132] Kazmierkowski M, Malesani L. Current control techniques for three-phase voltage-source PWM converters: a survey. IEEE Transactions on Industrial Electronics, 1998, 45(5):691-703.

- [133]Dalessandro L, Drofenik U, Round S, et al. A novel hysteresis current control for three-phase three-level PWM rectifiers. APEC 2005, 2005, 1:501-507.
- [134]Ho C, Cheung V, Chung H. Constant-frequency hysteresis current control of grid-connected VSI without bandwidth control. IEEE Transactions on Power Electronics, 2009, 24(11): 2484-2495.
- [135]Kwon B, Min B, Youm J. An improved space vector-based hysteresis current controller. IEEE Transactions on Industrial Electronics, 1998, 45(5):752-760.
- [136]Mohseni M, Islam S. A space vector-based current controller for doubly fed induction generators. IECON '09, 2009: 3868-3873.
- [137]Celanovic N, Boroyevich D. A comprehensive study of neutral-point voltage balancing problem in three-level neutral-point-clamped voltage source PWM inverters. IEEE Transactions on Power Electronics, 2000, 15(2): 242-249.
- [138]Dalessandro L, Round S, Kolar J. Center-Point Voltage Balancing of Hysteresis Current Controlled Three-Level PWM Rectifiers. IEEE Transactions on Power Electronics, 2008, 23(5): 2477-2488.
- [139]Ghennam T, Berkouk E, Francois B. DC-link voltage balancing algorithm using a space-vector hysteresis current control for three-level VSI applied for wind conversion system. EPE 2007, 2007.
- [140]Hautier JP, Caron J. Convertisseur statiques, methodologie causale de modelisation et de commande. Editions Tecnip, 1999.